CLAS-ANALYSIS

Measuring Σ and G of single charged pion production from polarized quasi-free neutron target

Authors : H. Y. Lu[1,2], W. J. Briscoe[12], A. D'Angelo[3,4], A. Deur[5], J. Fleming[6], A. Filippi[7], D. H. Ho[1], C. Hanretty[5,8], T. Kageya[5], F. J. Klein[9], E. Klempt[10], L. Lanza[3,4], M. M. Lowry[5], K. V. Nikonov[10,11], P. Peng[7], R. A. Schumacher[1], A. M. Sandorfi[5], A. V. Sarantsev[10,11], I. I. Strakovsky[12], N. K. Walford[9], X. Wei[5], R. L. Workman[12], and I. Zonta[3,4]

[1]Carnegie Mellon University, Pittsburgh, Pennsylvania 15213, USA
[2]University of Iowa, Iowa City, IA 52242
[3]Universitá di Roma Tor Vergata, 00133 Rome, Italy
[4]I.N.F.N., Sezione di Roma Tor Vergata, 00133 Rome, Italy
[5]Thomas Jefferson National Accelerator Facility, Newport News, Virginia 23606, USA
[6]Edinburgh University, Edinburgh EH9 3JZ, United Kingdom
[7]I.N.F.N., Sezione di Torino, 10125 Torino, Italy
[8]University of Virginia, Charlottesville, Virginia 22901, USA
[9]Catholic University of America, Washington, DC 20064, USA
[10]Helmholtz-Institute für Strahlen- und Kernphysik der Rheinischen Friedrich-Wilhelms Universität, Nussallee 14-16, 53115 Bonn, Germany
[11]National Research Center "Kurchatov Institute", Petersburg Nuclear Physics Institute, Gatchina 188300, Russia
[12]The George Washington University, Washington, DC 20052, USA

March 13, 2025

Abstract

The excited-state spectrum of the nucleon is a complicated overlap of many resonances that must be disentangled through multipole analyses of reaction amplitudes. Photoproduction of ions, which has been a fruitful probe of N* structure, requires data on many different polarization observables to constrain its four complex amplitudes. Although considerable data have been accumulated with proton targets, comparatively little information is available from neutron targets. Recently, the first beam-target helicity asymmetries with circular beam polarization have been reported in reaction $\gamma n(p) \to \pi^- p(p)$ [1]. This note presents a parallel analysis from the same experiment of the beam-target double-polarization observable "G" with a linearly polarized beam for the same reaction. Linearly polarized photons and longitudinally polarized deuterons in a solid hydrogen deuteride (HD) target were used with the CEBAF Large Acceptance Spectrometer (CLAS) at Jefferson Laboratory (JLab). Data from different polarization orientations of the beam and target are combined to extract the asymmetries of the beam (Σ) and beam-target (G). The preliminary results for the Σ observables are consistent with existing partial wave analysis (PWA) that incorporates other experiments. Preliminary results are reported for the energy and angular dependence of G.

Contents

1 Introduction

Quantum Chromodynamics (QCD) is widely accepted as a successful theory to describe the strong interaction. However, the spectrum of nucleon excitation resonances (N^*) poses many challenges. These span from the prediction of yet unobserved levels to the understanding of the properties of well-established states. In addition, spectral properties are altered by "dressing", such as meson loops and channel couplings [2], which are beyond the scope of perturbative QCD (pQCD). Although the scattering data for π N have been intensively analyzed to extract the information on N^*s, a complete decomposition of the reaction amplitude into multipoles of definite isospin, spin, and parity has not been achieved. Furthermore, comparatively little information from neutron target reactions is available, while separate $\gamma p N^*$ and $\gamma n N^*$ couplings and deducing the isospin $I = 1/2$ amplitudes are required. The production of a single pseudoscalar meson, such as the production of π, requires data on a minimum of 8 of a total of 16 different spin observables to avoid mathematical ambiguities [3]. This work aims to provide two of them in the N^* resonance region.

1.1 G14 experiment

The E06–101 experiment (the g14 run) at Jefferson Lab with the CEBAF Large Acceptance Spectrometer (CLAS) in Hall B [4] utilized a polarized beam on a polarized HD target [5, 6, 7]. During the experiment, circularly and linearly polarized photon beams were generated. Circularly polarized photons were produced by Bremsstrahlung of longitudinally polarized electrons on a 10^{-4} radiation length-thick Au foil. Linearly polarized photons were obtained by coherent Bremsstrahlung of the electron beam off a thin diamond radiator. The first beam-target helicity asymmetry data (E), obtained for the $\gamma n(p) \to \pi^- p(p)$ reaction using a circularly polarized photon beam on a longitudinally polarized deuterium target, were recently reported in Ref. [1]. In the present work, the same reaction has been studied using linearly-polarized photons on longitudinally polarized deuterons and the beam (Σ) and beam-target (G) helicity asymmetries have been extracted, in the 1800 MeV - 2200 MeV photon energy range.

1.2 Run conditions

The linearly polarized beam was generated using coherent Bremsstrahlung from a 30 μm diamond radiator. Two orientations were arranged, parallel (PARA) to the floor and perpendicular (PERP) to it. A 5551.77 MeV electron beam was used to generate polarized photons at three different coherent edges: 1800, 2000, and 2200 MeV. The majority of data was taken using the 2-prong trigger as well as the 1-prong trigger, pre-scaled by a factor of 8. This trigger condition is the same for all production runs. The runs are

Run range	Coherent edge	Date range	perp events	para events	Target polarization
69476 - 69543	1800 MeV	5/3 - 5/9	528.2 M	457.6 M	D($+24.0 \pm .5\%$)
69544 - 69578	1800 MeV	5/9 - 5/12	303.9 M	304.2 M	D($-16.2 \pm 1.1\%$)
69398 - 69419	2000 MeV	4/27 - 4/28	186.4 M	130.8 M	D($+25.8 \pm 0.8\%$)
69420 - 69474	2000 MeV	4/29 - 5/3	270.7 M	300.5 M	D($+24.0 \pm 1.5\%$)
69583 - 69616	2000 MeV	5/12 - 5/15	131.0 M	191.7 M	D($-16.2 \pm 1.1\%$)
69194 - 69225	2200 MeV	4/6 - 4/9	170.5 M	189.5 M	D($+26.0 \pm 0.8\%$)
69370 - 69372	2200 MeV	4/21 - 4/21	31.4 M	4.7 M	D($+15.8 \pm 0.2\%$)
69375 - 69397	2200 MeV	4/25 - 4/27	90.5 M	78.7 M	D($+25.8 \pm 0.8\%$)
69618 - 69636	2200 MeV	5/16 - 5/17	93.6 M	113.3 M	D($-16.2 \pm 1.1\%$)

Table 1: List of run conditions

summarized in Tab. 1. Runs with too many malfunctioning detector components or too low statistics have been discarded, as discussed in Sect. 2.5.

1.3 Separating asymmetries with double-polarization data

The general expression for the single pseudoscalar-meson production cross section involving a linearly polarized beam and longitudinally polarized target (summed over final recoil polarization states) is [3]:

$$\frac{d\sigma(P_\gamma, P_D)}{d\Omega} = \frac{d\sigma_0}{d\Omega}\left(1 - P_\gamma^L \Sigma(\theta; W) cos(2\phi_\gamma) + P_\gamma^L P_D^V G(\theta; W) sin(2\phi_\gamma)\right), \tag{1}$$

where Σ and G are beam and beam-target asymmetries, respectively, $d\sigma_0/d\Omega$ is the unpolarized differential cross section, which is independent from beam and target polarization, P_γ^L is the degree of linear beam polarization, P_D^V is the vector polarization of the deuteron along the beam axis Z, and ϕ_γ is the angle from the detected meson, π^- in this work, to the beam photon polarization vector. The reaction angles and formula are explained in details in Fig. 1. X_{CL}, Y_{CL}, and Z_{CL} define the detector (CLAS) coordinate system. P_γ aligns with either X_{CL} or Y_{CL} depending on whether the beam photon is parallel or perpendicularly polarized. X_{det}, Y_{det}, and Z_{det} define the reaction plane, where X_{det} is given by the direction of the detected π^-, Z_{det}=Z_{CL}, and Y_{det} is the normal of the reaction plane. Thus, ϕ_{det} is the azimuthal angle of π^- in the center-of-mass frame. Depending on the beam photon polarization direction, $\phi_\gamma + \phi_{det}$ equals either 2π or $\pi/2$. Therefore, the sign changes according to the table listed in Fig. 1.

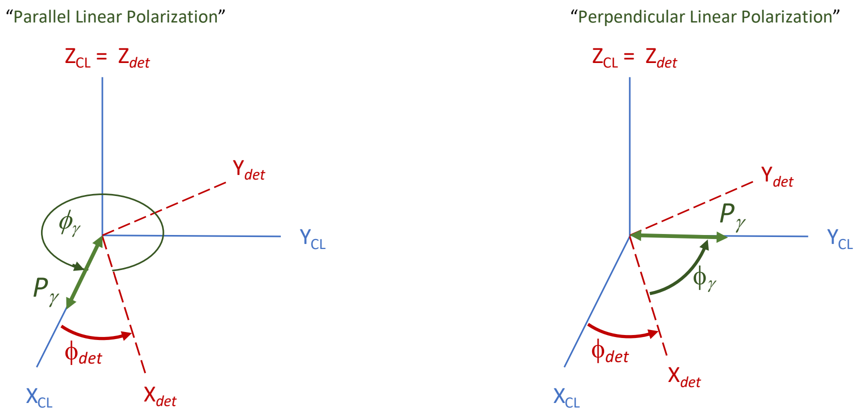

$$\phi_\gamma = (2\pi - \phi_{det}) \qquad \phi_\gamma = \left(\pi/2 - \phi_{det}\right)$$

P_γ state	P_γ alignment	$\cos(2\phi_\gamma)$	$\sin(2\phi_\gamma)$
|| (*parallel Pol*)	along X_{CLAS}	$+\cos(2\phi_{det})$	$-\sin(2\phi_{det})$
⊥ (*perpendicular Pol*)	along Y_{CLAS}	$-\cos(2\phi_{det})$	$+\sin(2\phi_{det})$

$$\frac{d\sigma(P_L^\gamma, P_z^T)}{d\Omega} = \frac{d\sigma_0}{d\Omega}\left(1 - P_L^\gamma \Sigma \cos(2\phi_\gamma) + P_L^\gamma P_z^T G \sin(2\phi_\gamma)\right)$$

P_γ *state*	$\lvert P_\gamma \rvert$	$\vec{P}^T$	$d\sigma/d\Omega(\phi_{det})$
|| , along X_{CLAS}	p_1	$+\lvert p_+ \rvert \hat{z}$	$d\sigma_0\left(1 - p_1 \Sigma \cos(2\phi_{det}) - p_1(p_+) G \sin(2\phi_{det})\right)$
|| , along X_{CLAS}	p_2	$-\lvert p_- \rvert \hat{z}$	$d\sigma_0\left(1 - p_2 \Sigma \cos(2\phi_{det}) + p_2(p_-) G \sin(2\phi_{det})\right)$
⊥ , along Y_{CLAS}	p_3	$+\lvert p_+ \rvert \hat{z}$	$d\sigma_0\left(1 + p_3 \Sigma \cos(2\phi_{det}) + p_3(p_+) G \sin(2\phi_{det})\right)$
⊥ , along Y_{CLAS}	p_4	$-\lvert p_- \rvert \hat{z}$	$d\sigma_0\left(1 + p_4 \Sigma \cos(2\phi_{det}) - p_4(p_-) G \sin(2\phi_{det})\right)$

Figure 1: Detailed sketch of reaction angles

All combinations of beam and target polarizations give four configurations:

1. beam polarization at zero rad and target polarization in +Z direction;
2. beam polarization at zero rad and target polarization in -Z direction;
3. beam polarization at $\pi/2$ rad and target polarization in +Z direction;
4. beam polarization at $\pi/2$ rad and target polarization in -Z direction

The differential cross sections for these four configurations are shown in the last table of Fig. 1. It can be easily derived that the yields of these four configurations at a given scattering angle are as follows.

$$\begin{aligned}
Y_1 &= L_1 A \Delta\Omega \frac{d\sigma_0}{d\Omega} \left(1 - p_1 \Sigma \cos(2\phi_{det}) - p_1 p_+ G \sin(2\phi_{det})\right)\\
Y_2 &= L_2 A \Delta\Omega \frac{d\sigma_0}{d\Omega} \left(1 - p_2 \Sigma \cos(2\phi_{det}) + p_2 p_- G \sin(2\phi_{det})\right)\\
Y_3 &= L_3 A \Delta\Omega \frac{d\sigma_0}{d\Omega} \left(1 + p_3 \Sigma \cos(2\phi_{det}) + p_3 p_+ G \sin(2\phi_{det})\right)\\
Y_4 &= L_4 A \Delta\Omega \frac{d\sigma_0}{d\Omega} \left(1 + p_4 \Sigma \cos(2\phi_{det}) - p_4 p_- G \sin(2\phi_{det})\right) ,
\end{aligned} \tag{2}$$

where ϕ_{det} is the azimuthal angle of π^- in the center-of-mass frame (ϕ will be used thereafter for short), L_i is the luminosity for each configuration, A is the acceptance which is approximately the same for all the configurations when $\Delta\Omega$, the solid angle of each bin, is large enough, p_i is the average beam polarization of each configuration, p_+ and p_- are averaged target polarization along the +Z and -Z directions. Using a simple algebra, the terms in Σ and in G can be independently evaluated as:

$$\Sigma \cos(2\phi) = \frac{s_1 Y_1 + s_2 Y_2 + s_3 Y_3 + s_4 Y_4}{a_1 Y_1 + a_2 Y_2 + a_3 Y_3 + a_4 Y_4} \tag{3}$$

$$G \sin(2\phi) = \frac{g_1 Y_1 + g_2 Y_2 + g_3 Y_3 + g_4 Y_4}{a_1 Y_1 + a_2 Y_2 + a_3 Y_3 + a_4 Y_4} - \Delta G, \tag{4}$$

where the coefficients for Σ are:

$$\begin{aligned}
s_1 &= \frac{-(p_-) p_2 C_{perp}}{N_1} & s_2 &= \frac{-(p_+) p_1 C_{perp}}{N_2}\\
s_3 &= \frac{(p_-) p_4 C_{para}}{N_3} & s_4 &= \frac{(p_+) p_3 C_{para}}{N_4}\\
a_1 &= \frac{(p_- + p_+) p_- D}{N_1 p_1} & a_2 &= \frac{(p_- + p_+) p_+ D}{N_2 p_2}\\
a_3 &= \frac{(p_- + p_+) p_- D}{N_3 p_3} & a_4 &= \frac{(p_- + p_+) p_+ D}{N_4 p_4} ,
\end{aligned} \tag{5}$$

where N_i is proportional to L_i and

$$\begin{aligned} C_{perp} &= p_4p_- + p_3p_+ \\ C_{para} &= p_2p_- + p_1p_+ \\ D &= p_1p_2p_3p_4. \end{aligned} \tag{6}$$

Normalization factors N_i are typically extracted from pre-scaled events to eliminate any dependence on different running conditions. The details are shown in Sect. 2.4. It is convenient to express the coefficients for G in terms of a new variable E, defined as:

$$E = \frac{(p_1 + p_3)p_2p_4p_- + (p_2 + p_4)p_1p_3p_+}{p_1p_2 + p_3p_4}. \tag{7}$$

Then the coefficients for G are:

$$\begin{aligned} g_1 &= -\frac{Ep_2}{N_1} \\ g_2 &= \frac{Ep_1}{N_2} \\ g_3 &= \frac{Ep_4}{N_3} \\ g_4 &= -\frac{Ep_3}{N_4} \\ \Delta G &= \frac{p_1 - p_2 - p_3 + p_4}{(p_1p_2 + p_3p_4)(p_- + p_+)} \end{aligned} \tag{8}$$

With these coefficients evaluated for four different sets of run conditions, Σ and G can be extracted independently from Eqs. (3) and (4) by fitting the $cos(2\phi)$ and $sin(2\phi)$ distributions.

2 Measurement

In Eqs. (3) and (4), the physics measurables are yields, beam linear polarization, target polarization, and flux normalization for each configuration, while acceptance is canceled in the formula. In this section, we present the procedures for extracting yield and flux normalization and for verifying that the acceptance variation is negligible.

2.1 Detector calibration

The calibration of the individual components of the spectrometer was performed sequentially since the calibration of one detector subsystem depended on the updated information from other detector subsystems. The order followed is Tagger, TOF, ST, DC, EC. The calibrations were performed by the collaborators in 12 iterations. Details on detector calibration are provided in the approved analysis note [8].

2.2 Energy and momentum correction

The raw data underwent a reconstruction process (colloquially known as cooking), using the standard program "*user_ana*". Charged particles emerging from the event vertex lose energy through interactions such as ionization when traveling through the target and detectors. Consequently, the reconstructed momentum from the drift chambers is smaller than that of a particle at the production vertex. The standard CLAS software package, "ELoss"[9], was used to account for these processes and correct for the volumes closer to the CLAS center than the Region-1 drift chambers. Corrections of tagger energy and particle momenta were applied; these corrections were based on kinematic fitting of $\gamma p \to \pi^+\pi^- p$ events, where all three final-state particles were detected. A detailed discussion of the above procedure can be found in the previous analysis note [8].

2.3 Yield extraction

To minimize statistical and systematic uncertainties, a series of data selection cuts have been applied and checked. They are described in this section.

2.3.1 Timing requirements

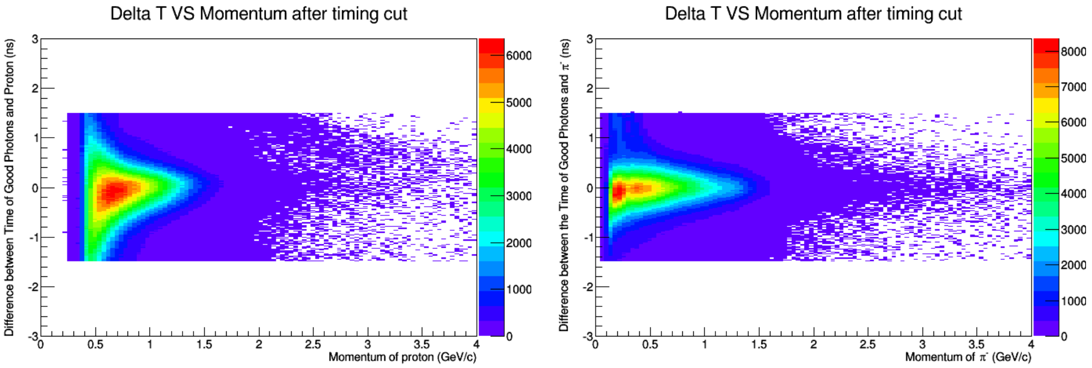

Figure 2: Time difference between proton (left) or π^- (right) and photon VS their momenta respectively.

In each event, timing and energy information of many photons are recorded. In order to find the interacting photon that generated the event and to discard the events where no correct photon information can be found, a timing cut is applied.

First, events with exactly two reconstructed charged particles are selected by reading the EVNT bank. The positively charged particle is assumed to be a proton and the negatively charged particle is assumed to be π^-. The times when these two particles started from the interaction point near the target center are calculated for each particle from its momentum, its track length between target center and hit time-of-flight counter, and the hit time at the time-of-flight counter.

$$t_{tc} = t_{SC} - \frac{l_{SC}}{\beta C} - (Z_{vt} - Z_{tc})/C \tag{9}$$

where t_{SC} is the time recorded at the time-of-flight detector (SC), l_{SC} is the reconstructed path length from the reaction point to SC, C is the speed of light, βC is the velocity by assuming the particle type, Z_{vt} is the reaction point, Z_{tc} is the target center where photon time is recorded. In this way, t_{tc} is the time of a particle of a certain type at the target center.

These are compared with the photon time at the target center:

$$\Delta t = t_\gamma - t_{tc}/C \tag{10}$$

where t_γ is the photon time recorded at the target center.

Figure 2 shows the time difference Δt between protons (left) or π^- (right) and photons as a function of the momentum of the particles. A cutoff point of ± 1.5 nanoseconds (ns) is applied to both time differences. Events with the selected photon are consistent with the assumption that a photon scatters off the quasi-free neutron, and a proton and a π^- are detected with consistent timing.

2.3.2 Exclusivity requirements

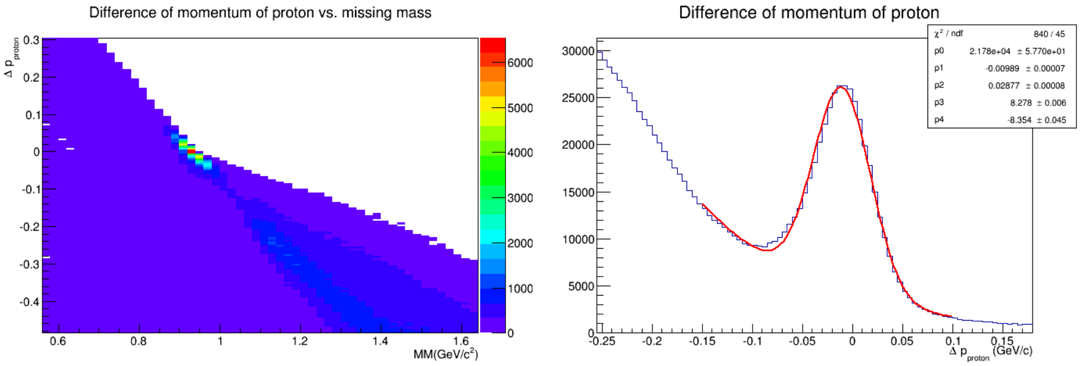

Figure 3: Left: Difference between measured and calculated momentum of proton versus the missing mass off the deuteron (MM($p\pi^- X$)). Right: Fit of the difference by a Gaussian over a polynomial background ($p_1 \equiv \mu = -0.010$ and $p_2 \equiv \sigma = 0.029$). (See Sect. 2.3.2.)

In Sec. 2.3.1, only the timing information is considered and therefore no exclusive reaction is chosen for each event. The deuterium in the HD composite was used to provide quasi-free neutrons. In order to single out the reaction off the neutron, the missing mass of

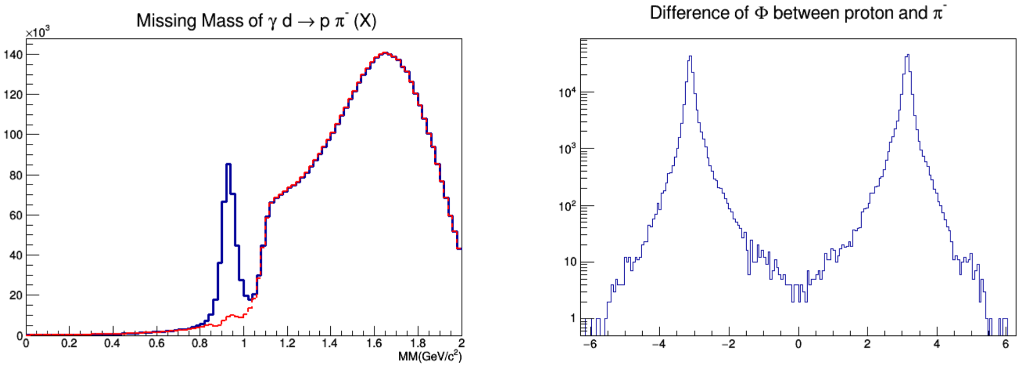

Figure 4: Left: Missing mass MM(pπ^-X) before selection (blue) and cut away (red). Right: ϕ angle between proton and π^- on logarithmic scale.

the incoming photon, target deuteron, and detected particles, proton and pion, was used to cut on the spectator proton. The missing mass after the above cut is shown in blue on the left side of Fig. 4. The peak at 0.9 GeV/c^2 is mainly from a spectator proton. The events other than the peak are from either inclusive production of $p\pi^-$ or misidentified 2-prong events. In order to select the events from the exclusive $p\pi^-$ production, an exclusive cut is performed using the following steps.

1. Calculate the boost needed to reach the center-of-mass frame of the photon and a neutron with non-zero momentum. The neutron momentum is calculated from the detected proton and π^- by assuming a two-body reaction and momentum conservation.

2. Calculate the momentum of the proton in the above center-of-mass frame, p_{cal}, by assuming the two-body reaction $\gamma n \to p\pi^-$.

3. Boost the detected proton momentum (p_{det}) into this center-of-mass frame and calculate the difference $\Delta p = p_{cal} - p_{det}$. This Δp is shown versus missing mass at the left in Fig. 3. The exclusive production events are concentrated in the area with $\Delta p \approx 0$ and $MM(p\pi^-X) < 1$ GeV/c^2.

4. The distribution of Δp is shown at the right in Fig. 3. A Gaussian-distribution peak plus a polynomial background is used to obtain the red curve. A 3-σ cut is applied to select the events.

The exclusivity cut is very efficient. Figure 4 shows the missing mass of cut-away events (those outside the above 3σ selection) in red on the left, and the azimuthal angle between proton and π^- on the right. The missing mass plot clearly shows that the cutaway distribution (red) is consistent with the background of all events (blue) before the cut. Leaves a set of exclusive production events for the next steps of the analysis. The azimuthal angle difference distribution confirms this by displaying two isolated peaks at ±π rad, which is consistent with the two-body reaction assumption.

2.3.3 Beam polarization selection

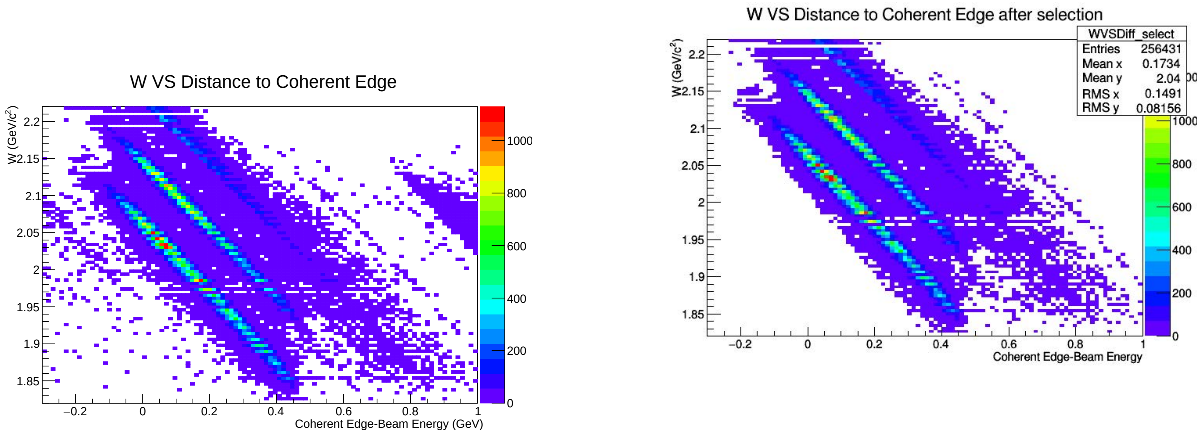

(a) W versus the difference between coherent edge and photon energy.

(b) W versus the difference between coherent edge and photon energy for the selected photon ranges

Figure 5: Dependence of W on the difference between coherent edge and photon energy.

The linearly polarized photon beam was produced by coherent bremsstrahlung. The diamond crystal radiator is carefully aligned with the electron beam. In this way, a large flux of linearly polarized photons is produced at a specific energy (the so-called "coherent edge"), which depends on the crystal orientation. The polarization and the polarized photon flux drop sharply at photon energies above the coherent edge and decrease less rapidly below the coherent edge. The degree of polarization was not measured directly. Instead, a theoretical model is fitted to the measured intensity distribution of the tagged photon energies and used to extract the coherent edge and photon polarization [10]. As shown in Fig. 5a, there are three bands corresponding to three set-ups of coherent edges: 1800, 2000, and 2200 MeV. There are scattered events from either unstable coherent edges and they are removed. The result is shown in Fig. 5b.

The uncertainty of the extracted photon polarization increases when the photon energy is further away from the coherent edge. The polarization itself also decreases when the photon energy is more distant from the coherent edge. The systematical uncertainties are smaller when the events with the beam energy closer to the coherent edge are selected, while the statistical uncertainties increases. The selection should be made in the way

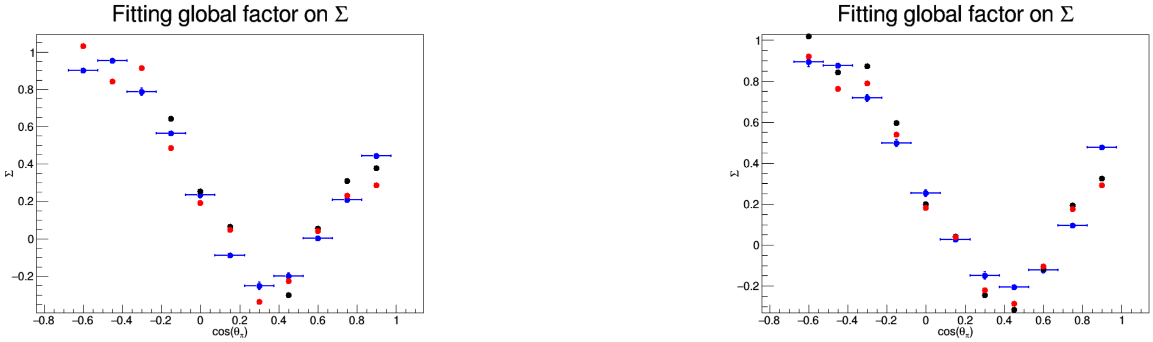

(a) fitting the scale factor with W from 1820 to 1900 MeV

(b) fitting the scale factor with W from 1900 to 1980 MeV

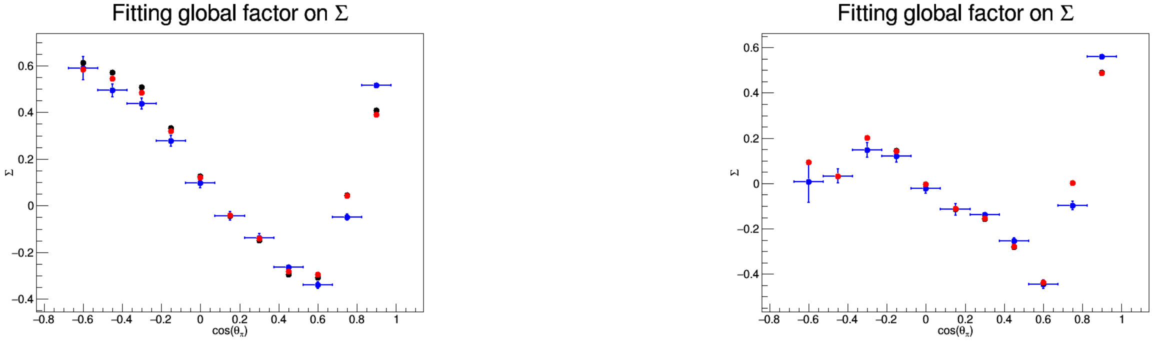

(c) fitting the scale factor with W from 1980 to 2060 MeV

(d) fitting the scale factor with W from 2060 to 2140 MeV

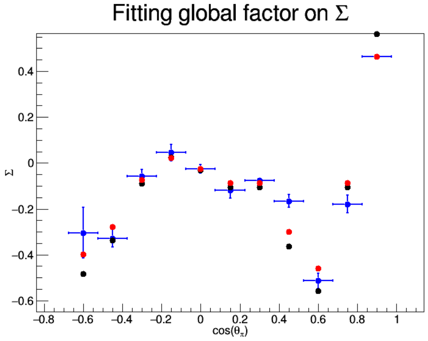

(e) fitting the scale factor with W from 2140 to 2220 MeV

Figure 6: Fitting the scale factors by minimizing Eq. 11. The blue dot with error bar is from G13, black is the original result, red is after applying the factor.

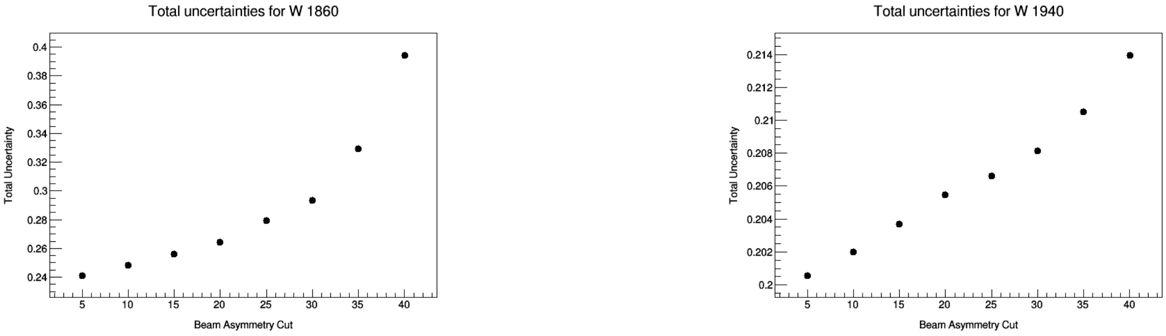

(a) Combined uncertainties with W from 1820 to 1900 MeV

(b) Combined uncertainties with W from 1900 to 1980 MeV

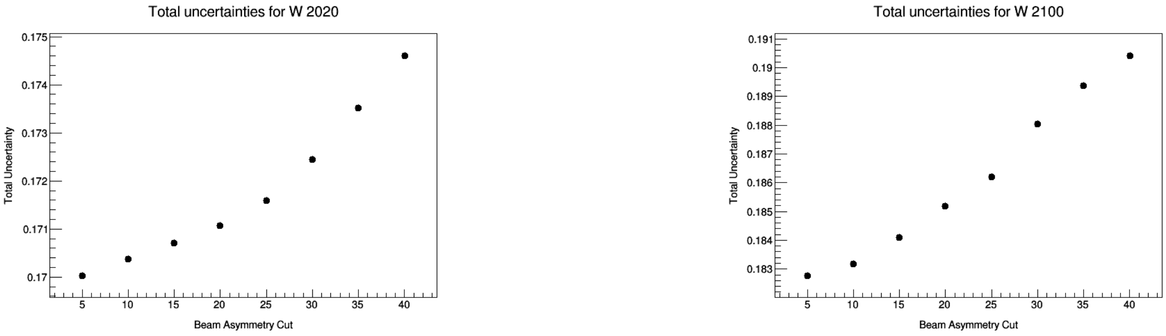

(c) Combined uncertainties with W from 1980 to 2060 MeV

(d) Combined uncertainties with W from 2060 to 2140 MeV

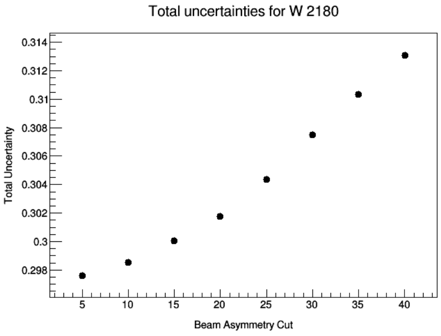

(e) Combined uncertainties with W from 2140 to 2220 MeV

Figure 7: Combined uncertainties of different beam polarization cut from 5% to 40% for each W bin.

that the combined uncertainties from systematics and statistics are minimized. Suppose there is a systematic bias on the beam polarization when the energy is faraway from the coherent edge. A global scaling factor for each W is obtained by minimizing

$$\gamma = \sum \Sigma_{g13} - c \sum \Sigma_{g14}. \tag{11}$$

The same scale factor c is multiplied on all the obtained Σ from this work. Then the difference between the results from G13 experiment and the scaled Σ is minimized by adjusting the scale factor c. The results for each W bin is shown at Fig. 6. The same scale factor is applied on the asymmetry G. Then the averaged change from the scaled G and the original value is considered as "systematical uncertainty",

$$\sigma_{sys} = \frac{\sum |1-c||g|}{N}, \tag{12}$$

while the statistical uncertainties are defined as

$$\sigma_{stat} = \frac{\sum \Delta g}{N}. \tag{13}$$

The Δg is the statistical uncertainties of each individual bins and the sum is over all the individual bins in the same W bin. The total uncertainty is defined as

$$\sigma = \sqrt{\sigma_{sys}^2 + \sigma_{stat}^2}. \tag{14}$$

The combined uncertainties for different beam polarization cut ranging from 5% to 40% in each W bin is compared at Fig. 7.

These figures show that the combined uncertainties are always increasing with a tighter cut on the beam polarization above 5%. It seems like the cut should be below 5%. However, the uncertainty on the beam polarization in general is greater than 5% [10]. Therefore, we select the events by requiring the beam polarization greater than 10%.

2.3.4 Missing momentum selection

Since a deuteron target was used to provide neutrons in this experiment, the momentum of the recoiling "spectator" proton needs to be chosen in a proper range. As the momentum of the undetected spectator proton increases, contributions from final state interactions (FSI) and Fermi motion increase, which are not associated with the effective $\gamma + n$ process of interest. While this favors a tight cut on the missing momentum, it comes at the cost of statistical uncertainty. Rather than invoking theoretical arguments, the optimal maximum momentum is extracted from the data themselves. The data used in Fig. 8 were selected by requiring the beam energy below 2 GeV and $0.4 < cos(\theta_\pi) < 0.6$. This kinematic region was chosen because Σ is comparatively large and different from zero,

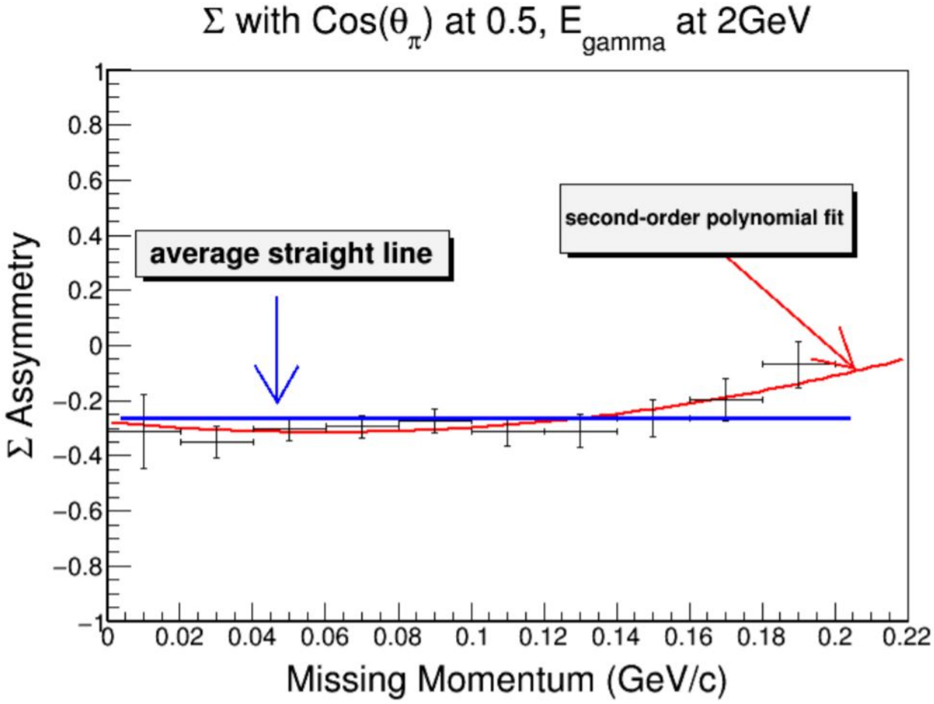

Figure 8: Σ with different missing momentum selections. The second-order polynomial fit (red curve) is superimposed, as well as the average (straight line in blue).

and the data sample is large. The missing momentum dependence of Σ is shown in Fig. 8. The Σ values are essentially independent of the missing momentum below 0.16 GeV/c, beyond which they begin to rise. The second-order-polynomial extrapolation to zero missing momentum yields a value, which is very close to the average. The selection of missing momentum below 0.16 GeV/c is adopted here and 0.18 GeV/c is used for studying systematic uncertainties.

2.3.5 Dilution factor and reaction vertex requirement

Figure 9 shows the vertex distribution from an empty target. Three dominant peaks originate from Kel-F (C_2ClF_3) windows. The first two Kel-F windows are walls of the target cell, which contains auxiliary aluminum cooling wires and target material (HD) when the cell is filled. The third major peak is isolated from the target area and provides the opportunity to flux-normalize runs of different polarization configurations, as well as production and empty-target runs. In order to minimize contributions from the target walls, the target-material area was chosen between −10 cm and −6 cm. Events inside this target-material area are chosen to extract asymmetries. In the early state of the

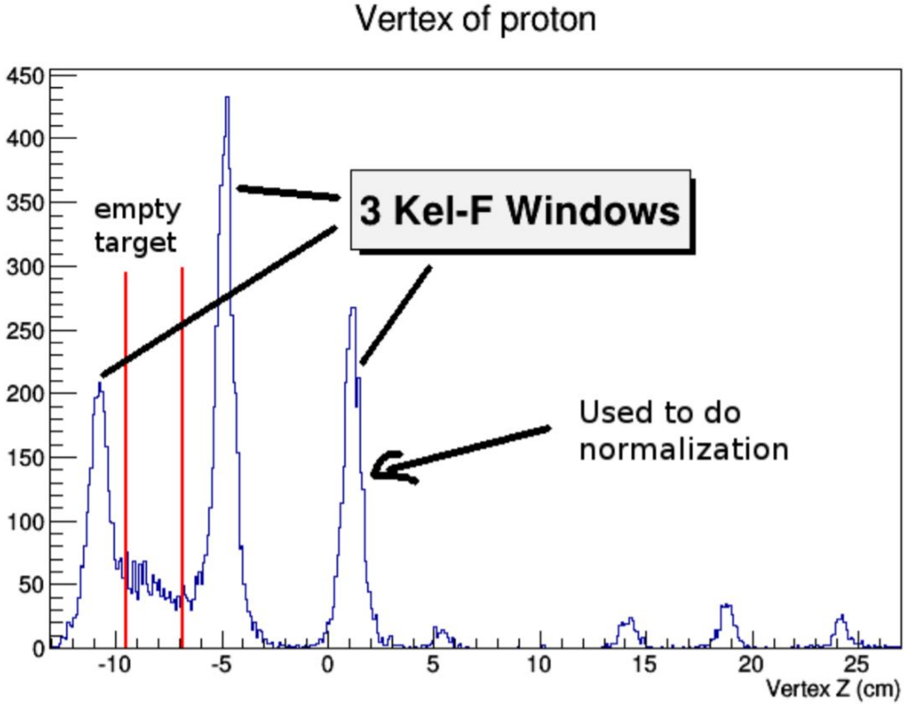

Figure 9: Vertex distribution of the empty HD-ice target insert.

analysis, a narrower area was chosen between −9.6 cm and −6.9 cm (between the red lines in Fig. 9). A dilution factor was obtained for the narrower area first, and then an additional correction factor was obtained by comparing the beam asymmetry for reaction vertices in these two areas.

The aluminum wires within the target material area of Fig. 9 are not polarized and dilute the asymmetry values, which need to be corrected. The dilution factor is defined as

$$f_{dilution} = \frac{N_p}{N_p - N_e} \tag{15}$$

where N_p and N_e are the flux-normalized yields in the target material area from production target and empty target runs, respectively. This dilution factor is a multiplicative correction to the extracted asymmetry values. The vertex distributions from production runs (red) is shown together with empty-target data (blue) on the left plot of Fig. 10. They are normalized by matching the number of events in the normalization area around the third Kel-F peak. The normalization area is determined by the width around the third peak, as indicated by two straight vertical lines. After varying this width, the dilution factor varies as shown on the right side of Fig. 10. When the width is greater than 4 cm, the value is stable. The final value is taken as the average of the stable values, namely

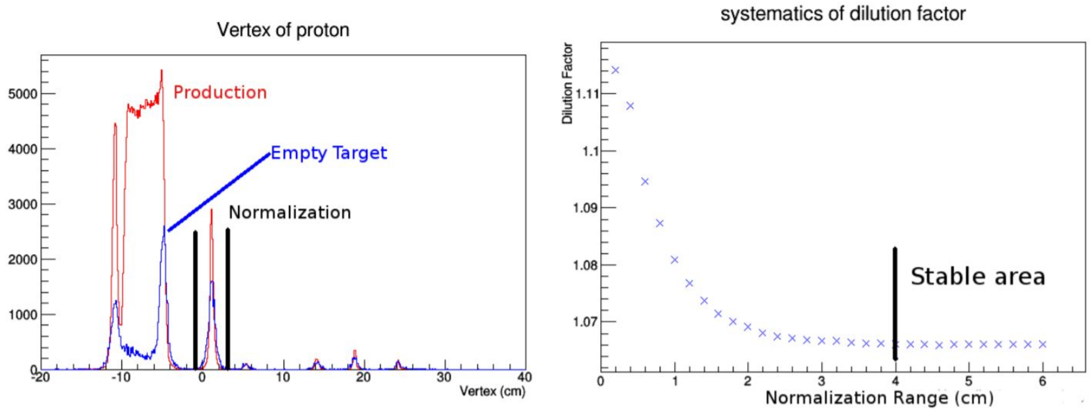

Figure 10: Left: Vertex distribution for a production run in red and for an empty-target run in blue. Right: Dilution factor dependence on the width of normalization area. The dilution factor converges when the normalization range is above 2.6 cm and stable above 4 cm.

1.066.

The target material range was extended to the range between -10.0 cm and -6.0 cm to accumulate more data. The Σ asymmetry was extracted for this vertex range and compared with the tighter vertex range. A linear relation was found and a slope of 0.991 ± 0.011 was fitted, as shown in Fig. 11. This implies that the asymmetry extracted using the wider range, -10 to -6 cm, is lower than that of the narrower range, -9.6 cm to -6.9 cm. This can be explained by the assumption that more supporting materials are in the wider range than in the narrower range. This suggests that a correction factor of 1 / 0.8991 needs to be applied on the results of the wider vertex selection. The general factor for this larger cut is $1.066/0.991 = 1.076$.

2.4 Flux normalization

Data for parallel- and perpendicular-photon polarization settings were taken in alternating sequences of about 100 million triggers. The run numbers for the g14 data take range from 69194 to 69636. The target polarization changed three times during the runtime for this analysis: it was reduced after a target quench from run 69364, there was a target change after run 69372, and the polarization changed after run 69543. During the g14 run we experienced deteriorated acceptance of some detector components, in particular some electronics components of the Time-of-Flight hodoscope and drift chambers showed worsened resolution or were off for short times. In order to reduce the systematic uncertainties run-dependent effects have been studied.

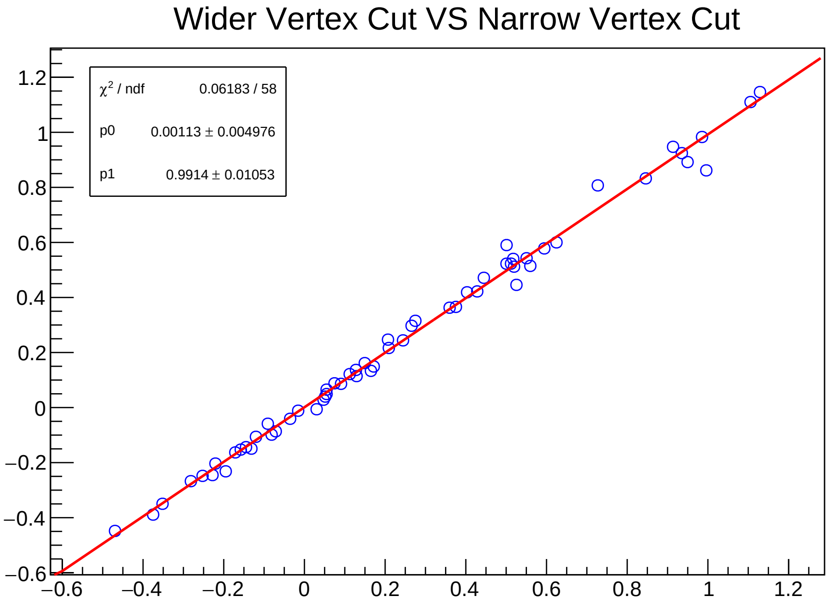

Figure 11: Σ from wider vertex cut (-10.0 cm $< z <$ -6.0 cm) vs narrow vertex cut (-9.6 cm $< z <$ -6.9 cm). A linear fit is performed and the fitted slope is 0.99 ± 0.01.

2.4.1 Problem and solution

The flux normalization is given by the total number of photons on the target material for each configuration. For this analysis absolute normalization yields are not needed because the asymmetries are extracted using the ratios of the normalization factors. Therefore, only the relative normalization is needed, which differs from the absolute normalization by an equal constant factor for all configurations. The experiment uses a polarized target cell with other unpolarized support material. The original idea was to use the same reaction channel off the support material, namely the forward Kel-F material, to find the normalization factors. However, there is an azimuthal angular dependence of the yield of the reaction scattering from the Kel-F material, probably because of the polarized beam. The extraction of the Σ and G asymmetries is based on the azimuthal distributions of these two observables. Thus, the azimuthal angular distribution of the normalization would bias the results.

An alternative is to find a different exclusive reaction that exhibited no azimuthal angular dependence. Unfortunately, no such channel is known to us, and it is likely that any exclusive reaction would show some azimuthal dependence.

The only apparent choice left is to use inclusive data, not restricted by the two-prong trigger of g14. Fortunately, such an inclusive channel is found, and it shows no azimuthal angular dependence.

2.4.2 Level-1 trigger

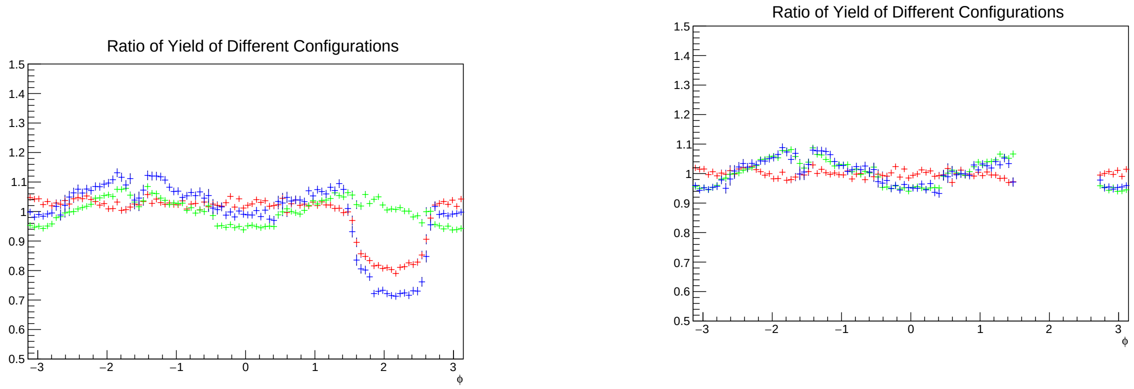

(a) Ratio of normalized ϕ distribution of all negative particles to (Para, +Z): (Perp, +Z) is in green, (Para,-Z) in red, and (Perp, -Z) in blue.

(b) Ratio of normalized ϕ distribution of all negative particles to (Para,+Z) after removing the inefficient range: (Para,-Z) is in red, (Perp, +Z) in green, and (Perp, -Z) in blue.

Figure 12: Ratio of normalized ϕ distributions for different configurations using negatively charged particles only.

As described in Sect. 2.4.1, the angular distribution is compared for different configurations. The configurations are identified by the beam polarization, parallel (para) or perpendicular (perp), and the target polarization, +Z or -Z. For this comparison, one configuration is chosen as the standard (Para, +Z), and the ratio of the others to the standard is plotted and examined.

During this part of the g14 run, two trigger bits in the TGBI bank are related to the level-1 trigger setting: bit 1 for tracks in at least two sectors (2-prong trigger) and bit 2 for tracks in at least one sector (1-prong trigger). In this flux normalization study, we require that trigger bit 2 is set. To be consistent with the ϕ definition in Eq. 1, only negatively-charged particles are chosen in the first trial. The result is shown in Fig. 12a. Data points show the ratios of (Para, -Z) to (Para, + Z) in red, (Perp, + Z) to (Para, + Z) in green, and (Perp, -Z) to (Para, + Z) in blue. The red and blue data points show a depletion at about $1.6 < \phi < 2.7$ rad, which can be attributed to a new dead zone in the Sector 3 drift chambers in later runs. After removing this inefficient angular range, the normalization factors have been updated. As shown in Fig. 12b, the blue and green data points line up much better; however, they are still different from the red ones.

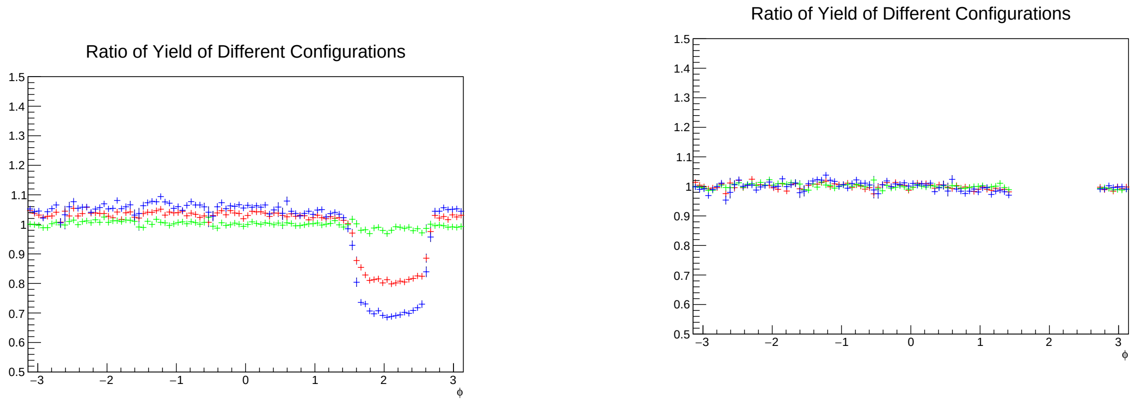

(a) Ratio of normalized ϕ distribution of all charged particles to (Para,+Z): (Para,-Z) is in red, (Perp, +Z) in green, and (Perp, -Z) in blue.

(b) Ratio of normalized ϕ distribution of all charged particles to (Para,+Z) after removing the inefficient range: (Para,-Z) is in red, (Perp, +Z) in green, and (Perp, -Z) in blue.

Figure 13: Ratio of normalized ϕ distributions for different configurations using all charged particles

Extending this study to all charged particles, the resulting ratios of extracted yields for the four configurations covering the full azimuth range are shown in Fig. 13a and the selected region is shown in Fig. 13b. The ratio of (Para,-Z) to (Para,+Z) is in red, the ratio of (Perp,+Z) to (Para,+Z) is in green, and the ratio of (Perp,-Z) to (Para,+Z) is in blue. The plots show that, except for the inefficient region, all ratios are consistent with unity.

An asymmetry measurement does not require knowledge of the absolute beam flux, but only the relative flux for the data taken under different polarization settings. So, the yield of inclusive channels can be chosen to represent the flux normalization, as long as the yields for different configurations show the same angular and energy dependence.

2.4.3 Separate into configurations and W bins

The above process must be repeated for the four configurations described in Eq. 2, as well as for each W bin used in this analysis work. The normalization factors obtained are listed on Tab. 2.

W bin center value (MeV)	(para,+z)	(para,-z)	(perp,+z)	(perp,-z)
1860	382597	772528	361279	774021
1940	343872	715271	320996	715984
2020	414740	862141	383119	868527
2100	380554	839283	351585	841563
2180	248996	575575	232948	597817
2260	169453	347130	167588	380547

Table 2: List of relative flux normalization factors for all six energy bins.

2.5 Acceptance checks

Equations (3) and (4) are derived from Eq.2 assuming that the acceptance does not change for different configurations so that it can be canceled by dividing the yields from different configurations. The acceptance for each run within the same configuration needs to be compared, to spot whether there are any acceptance variations within any of the twelve configurations, and in case any acceptance variation is found, how it could be corrected.

2.5.1 ϕ distribution

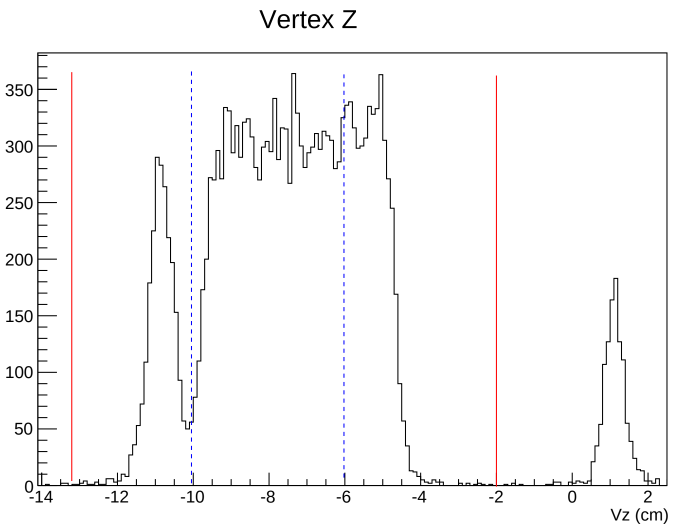

Figure 14: Vertex selection for extracting the asymmetries (dashed blue) and for studying the acceptance (solid red).

To check if there is any acceptance change, the data are processed with the same procedure as extracting the asymmetries. The same data selection criteria have been applied except the vertex cut. The vertex cut is applied to select the HD volume when extracting the asymmetries, while here we select the whole target volume, including the target windows, to enhance the statistics without losing the sensitivity to the acceptance. The two different vertex cuts for extracting the asymmetries and studying the acceptance are shown in Fig. 14 as blue and red solid lines, respectively. The other criteria are the same including timing cut, missing momentum cut, exclusivity cut, missing mass cut, and beam polarization cut. After the above steps, the ϕ distribution is obtained for each run.

2.5.2 Searching for odd-behaving runs

After obtaining the distributions of the azimuthal angle ϕ in the lab frame for all runs, the histograms for all runs belonging to the same configurations are summed to obtain twelve histograms of different configurations, as shown in Sect. C. To study the acceptance in the region of the detector where smooth behavior is expected, the bins corresponding to the sector gaps are removed. The ratio histograms are obtained for each run by dividing the distribution histogram ϕ for each run by the corresponding sum histogram and are fitted with a straight line as shown in Sect. D.

These ratio histograms are checked one by one and "problematic" runs are inspected. The histograms for these runs typically show at least one of the following issues:

a) dead area where no yield is observed while statistically relevant yield is expected,

b) dead area where no yield is observed but it is not certain whether this might be due to low statistics, or

c) inefficiency area where the ratio is significantly lower than in the other ϕ ranges.

These problematic runs, discussed below, were removed from the sum. The above process is repeated until no new problematic runs are found.

Runs 69372, 69375, 69412, 69429, 69618, 69621, and 69635 had very low statistics and were removed from the run list.

There are two runs with inefficient areas where a correction can be applied, and they are included in the final list of runs to be analyzed. These two runs are 69422 and 69540, and their distributions ϕ and ratio histograms are shown in Figs. 15 and 16. They show two inefficient sectors (sectors 2 and 5 for the 69422 run and sectors 3 and 6 for the 69540 run), which can easily be corrected by an additional factor, which is determined by scaling the ratios in the inefficient regions to the averaged ratio of the other regions, shown as straight lines in Fig. 17. The blue lines are the fitting ratios for the inefficient regions, while the red lines are the ratios for other regions. The correction factor is 1.9 for events in the inefficient region for run 69422 and 1.6 for 69540. After multiplying these factors by events in the inefficient sectors, the ratios of the inefficient regions are corrected as shown in Fig. 18

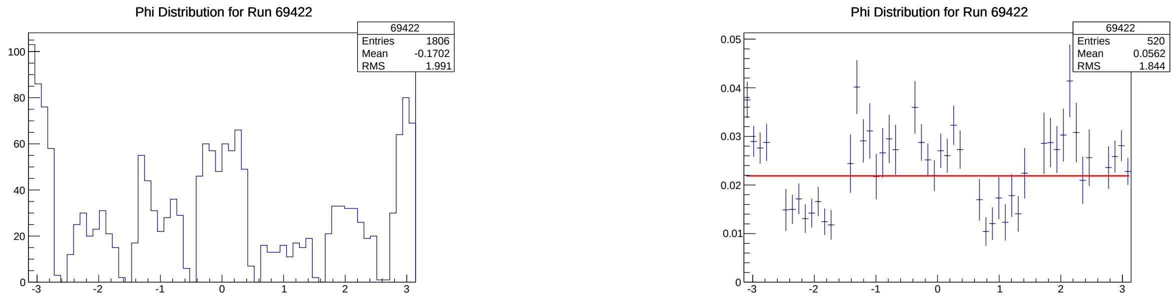

Figure 15: ϕ distribution (left) and ratio (right) of run 69422.

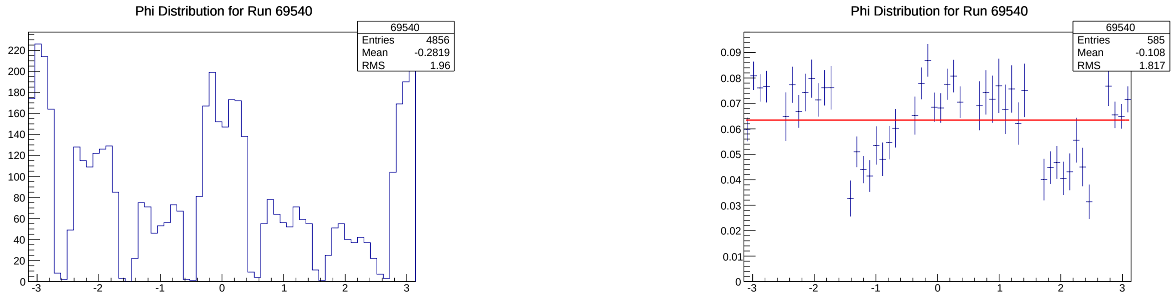

Figure 16: ϕ distribution (left) and ratio (right) of run 69540.

Five runs with dead regions were found that cannot be used for this analysis, as shown in Figs. 19 to 23, and are 69542, 69546, 69547, 69548, and 69549. During these runs an electronic box was off for Drift Chamber Region 1 in Sector 3. Fortunately, these runs belong to the configurations for the 1800 MeV coherent edge, which have a lot of statistics.

After applying the results of this acceptance study, the ϕ distributions and ratios for each run do not vary significantly from their averaged distributions for the corresponding configuration. The average distribution for each configuration is shown in the Appendix C.

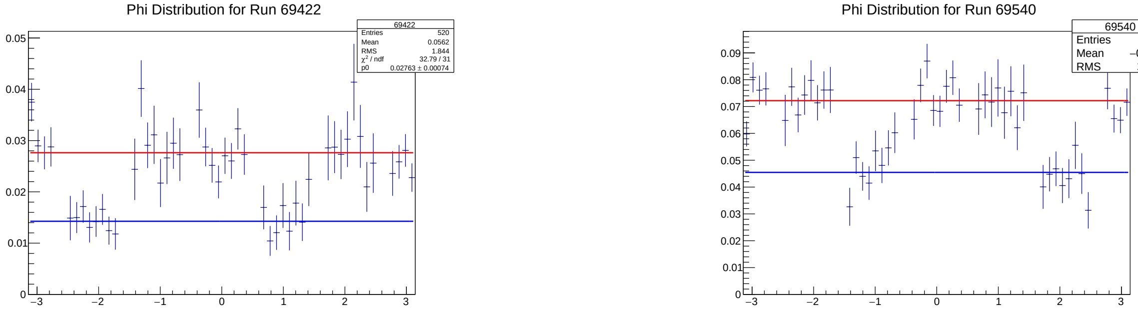

Figure 17: Fit of ratio excluding the inefficient regions in red and only inefficient regions in blue for run 69422 (left) and 69540 (right).

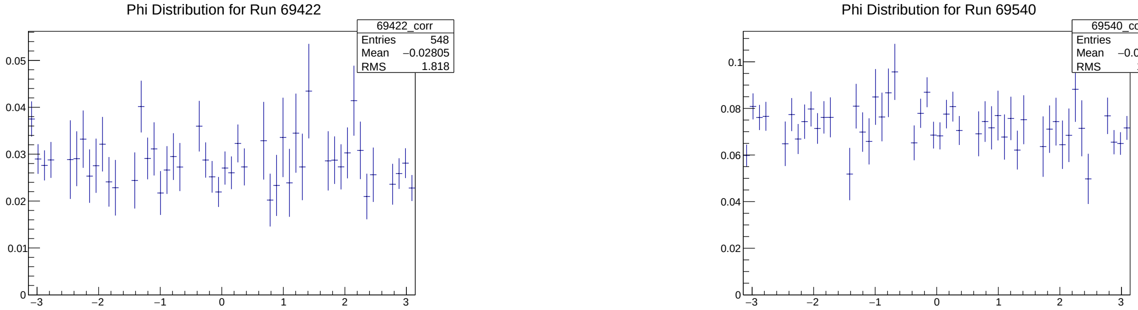

Figure 18: Yields in inefficient regions are multiplied by the correction factor 1.9 for run 69422 (left) and 1.6 for 69540 (right).

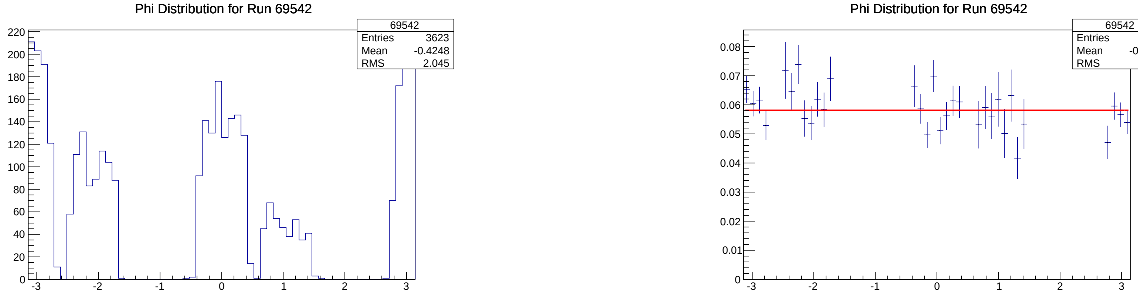

Figure 19: ϕ distribution (left) and ratio (right) of run 69542.

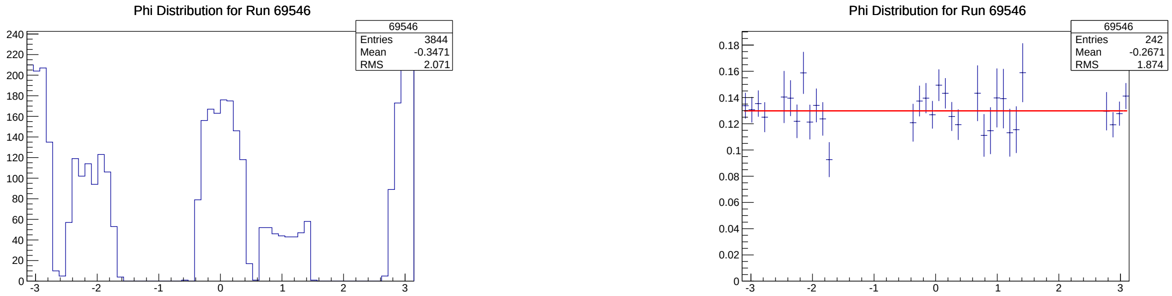

Figure 20: ϕ distribution (left) and ratio (right) of run 69546.

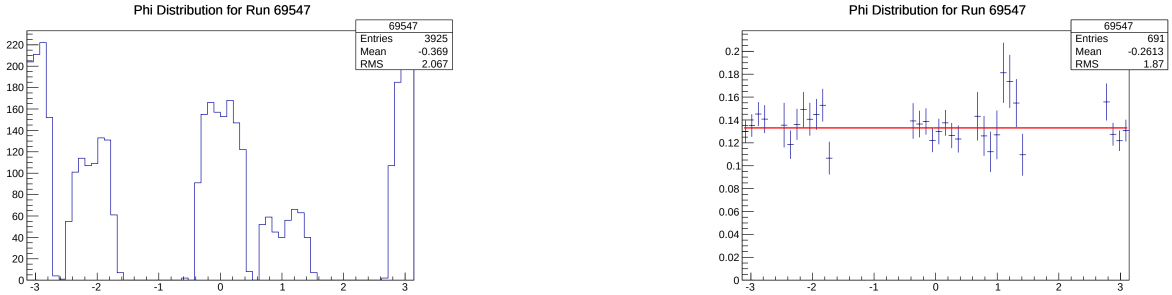

Figure 21: ϕ distribution (left) and ratio (right) of run 69547.

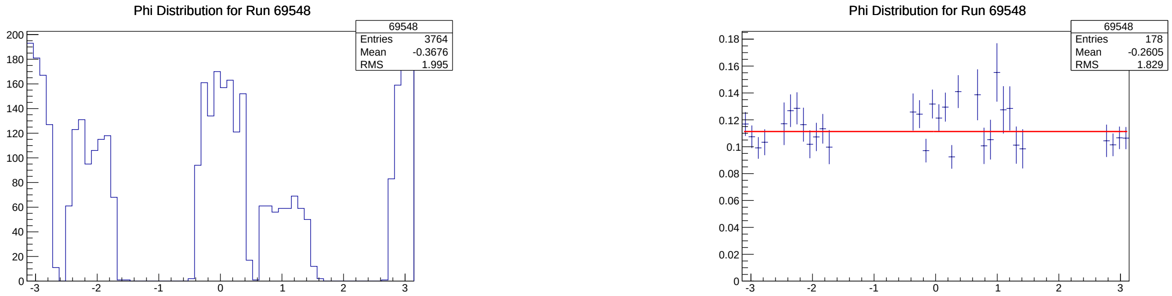

Figure 22: ϕ distribution (left) and ratio (right) of run 69548.

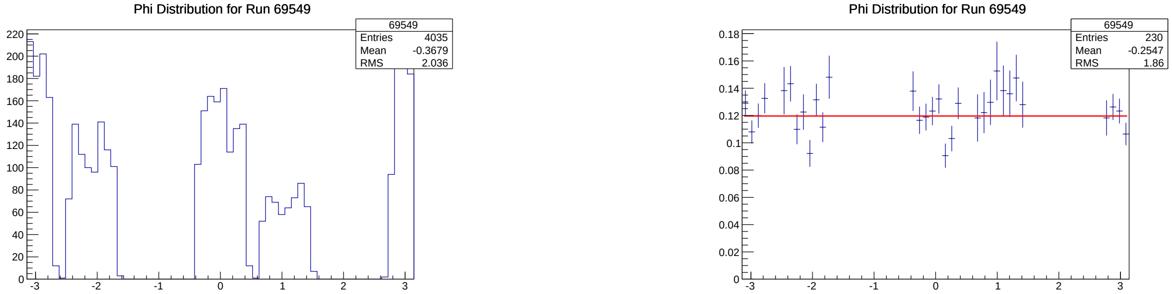

Figure 23: ϕ distribution (left) and ratio (right) of run 69549.

3 Systematic uncertainties

The asymmetries are obtained by fitting the ϕ distributions in each $\cos\theta_{cm}$ and W bin for the four combinations of beam and target polarization settings. The extracted asymmetries include only statistical uncertainties. However, systematic uncertainties from each cut need to be estimated, and are discussed in this section.

3.1 Systematics from timing cut

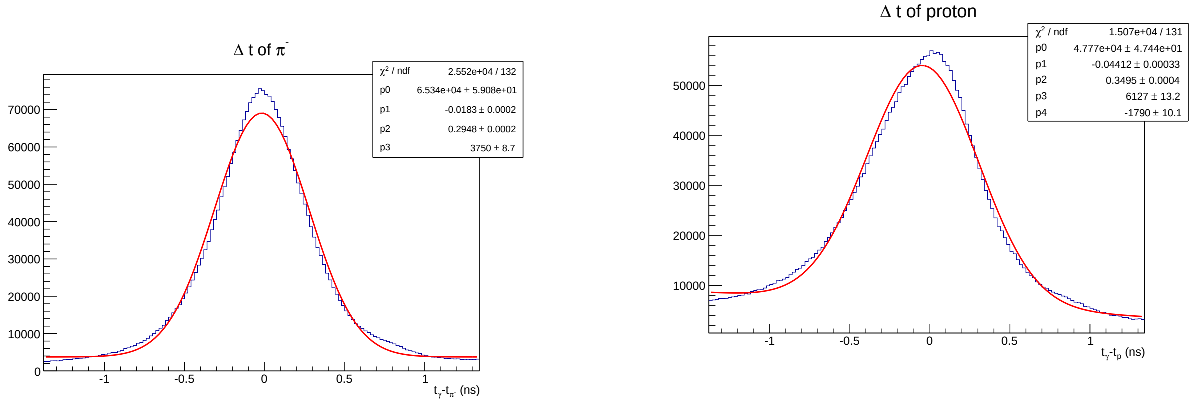

(a) Time difference between beam photon and π^-, fitted with a Gaussian (μ=p1, σ=p2) and a horizontal line (offset=p3).

(b) Time difference between beam photon and proton, fitted with a Gaussian (μ=p1, σ=p2) and straight line (offset=p3, slope=p4).

Figure 24: Time difference between photons and final state particles.

The timing cuts are applied on the π^- and proton and require both of them to be ±1.5 ns relative to the beam photon. The time difference between photon and π^-, as well as between photon and proton, is shown in Fig. 24. The fitted standard deviations are 0.29 and 0.35 ns for π^- and the proton, respectively. The timing cuts are changed from 1.5 to 1.5-0.29 ns for π^- and from 1.5-0.35 ns for the proton, and the same process of extracting Σ and G is performed using the modified timing cuts. The results of Σ are compared and their differences are fitted with a Gaussian function as shown in Fig. 25. The mean value is consistent with zero and the standard deviation is 0.011. Similarly, the comparison of G and the fit to the difference in the Gs distribution are shown in Fig. 26. The mean is again consistent with 0 and the standard deviation is 0.022.

In summary, the systematic uncertainty of the applied timing cut is 0.011 and 0.022 for Σ and G, respectively.

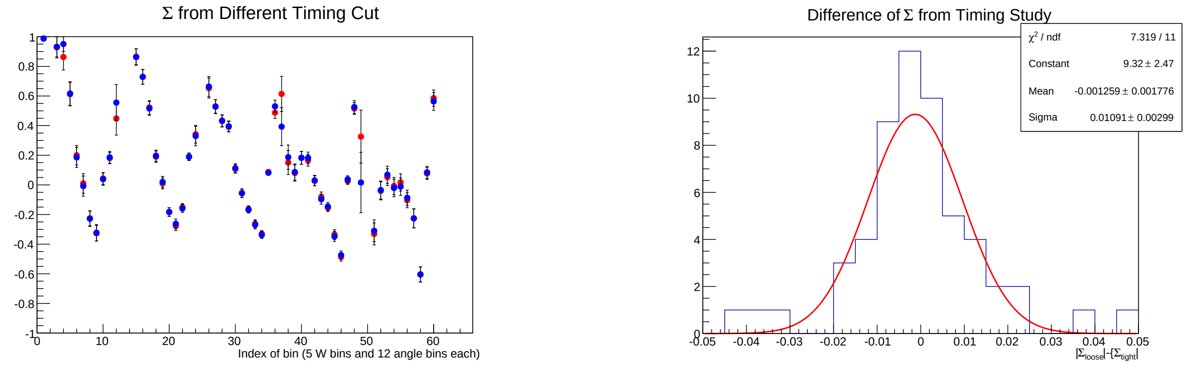

(a) Comparison of Σ for the two different timing cuts. Original results are in red, and points from varied cuts in blue.

(b) Distribution of the differences of Σs from the two timing cuts is fitted with a Gaussian function.

Figure 25: Systematic uncertainties of Σ from timing cut. The (a) distribution collects the spreads of Σ values obtained in all bins in W (5 ranges) and in angle (12 bins per W range), for a total of 60 entries, which is fed to histogram (b) for the Gaussian fit.

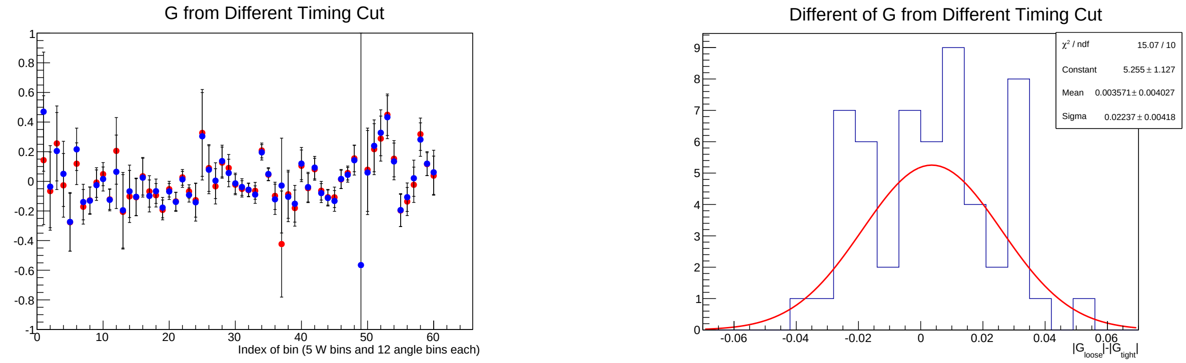

(a) Comparison of G for the two different timing cuts. Original results are in red, and points from varied cuts in blue.

(b) Distribution of the differences of Gs from the two timing cuts is fitted with a Gaussian function.

Figure 26: Systematic uncertainties of G from timing Cut.

3.2 Systematics from exclusivity cut

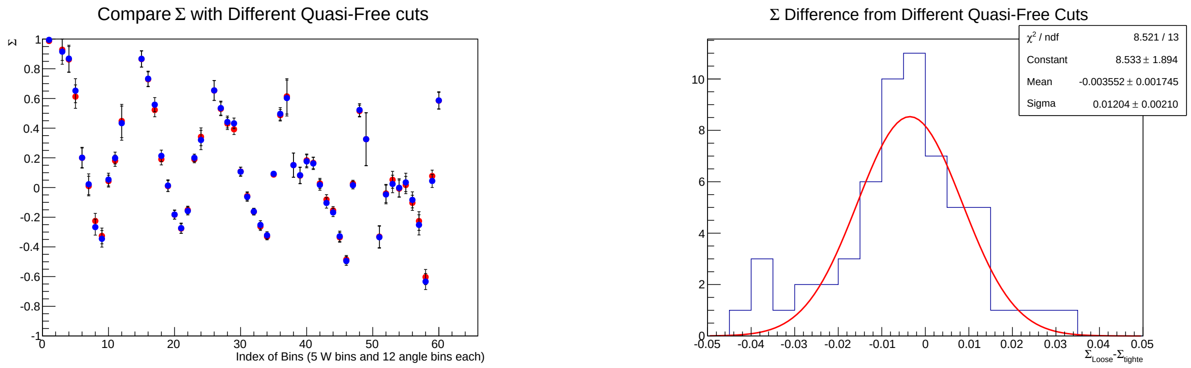

(a) Comparison of Σ for 2- and 3-σ exclusivity cuts. Original results are in red, and points from varied cuts in blue.

(b) Distribution of the differences of Σs from the two exclusivity cuts is fitted with a Gaussian function.

Figure 27: Systematic uncertainties of Σ from exclusivity Cut.

The exclusivity cut as described in Sect. 2.3.2 is 3-σ cut from Fig. 3. In order to obtain the systematic uncertainty of this cut, a 2-σ cut has been applied. The same process of extracting Σ and G has been performed again. The results of Σ are compared and then the differences are fitted with a Gaussian function as shown in Fig. 27. The mean value is consistent with zero and the standard deviation is 0.012. Similarly, the comparison of Gs and the fit to the difference of the Gs distribution are shown in Fig. 28. The mean is again consistent with 0 and the standard deviation is 0.017.

In summary, the systematic uncertainty of the exclusivity cut is 0.012 and 0.017 for Σ and G, respectively.

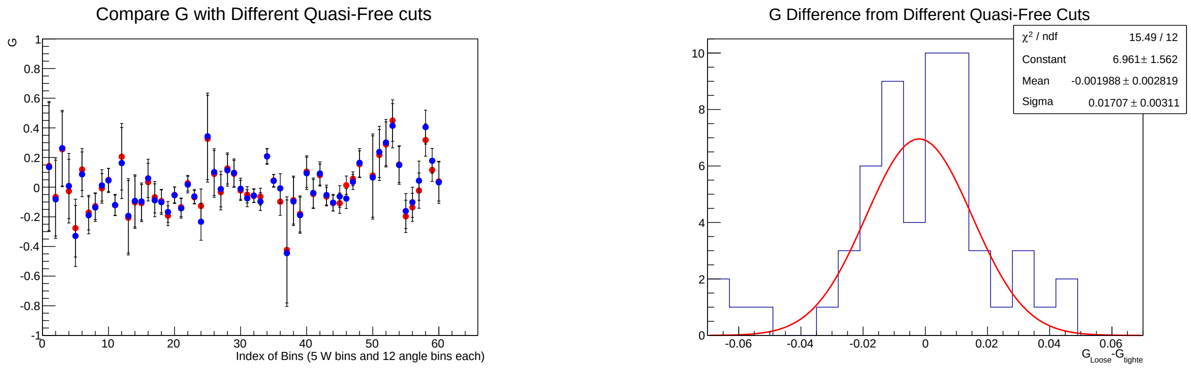

(a) Comparison of G for the two different exclusivity cuts. Original results are in red, and points from varied cuts in blue.

(b) Distribution of the differences of Gs from the two exclusivity cuts is fitted with a Gaussian function.

Figure 28: Systematic uncertainties of G from exclusivity Cut.

3.3 Systematic uncertainties from missing momentum cut

The missing momentum cut uses 0.18 GeV/c to select quasi-free events, while 0.20 GeV/c has been applied to extract the systematic uncertainty. The difference of Σ from these two cuts is calculated and then fitted with a Gaussian function as shown in Fig. 29. The standard deviation is 0.008. Similarly, the differences of G from different missing momentum cuts are calculated and fitted in Fig. 30. The standard deviation is 0.013. As seen in both figures, the mean is not centered at zero even considering the uncertainty of the fit.

In summary, the systematic uncertainty of missing momentum cut is 0.008 and 0.013 for Σ and G , respectively.

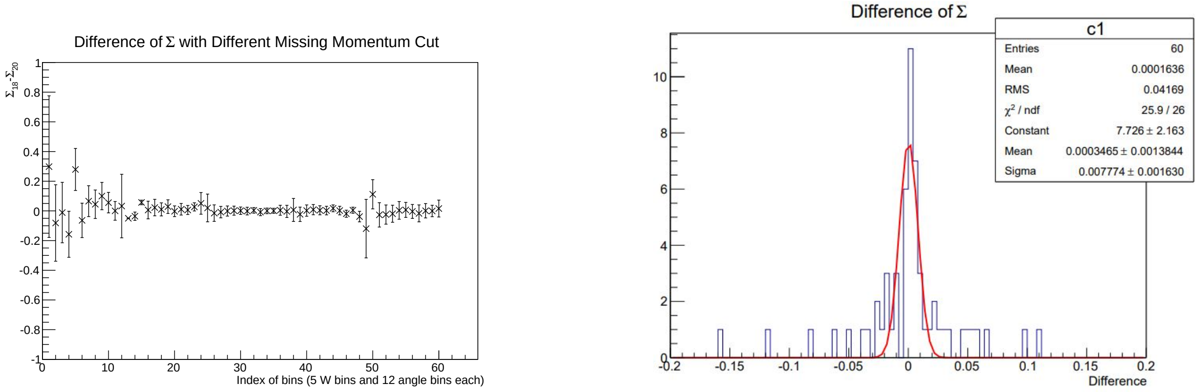

(a) Difference of Σ asymmetries for 0.18 GeV/c and 0.20 GeV/c missing momentum cuts.

(b) Distribution of the differences of Σs from the two missing momentum cuts is fitted with a Gaussian function.

Figure 29: Systematic uncertainties of Σ from missing momentum Cut.

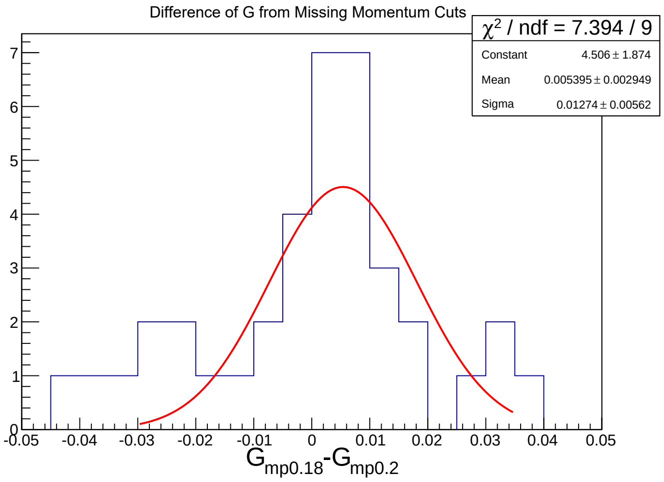

Figure 30: Distribution of the differences of Gs from the two missing momentum cuts is fitted with a Gaussian function.

3.4 Systematics from ϕ cut

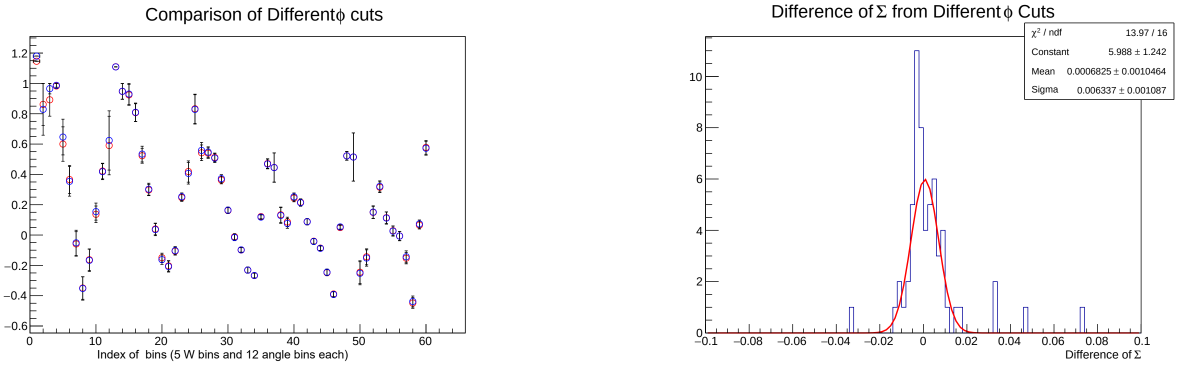

(a) Comparison of Σ for two different ϕ cuts. Original results are colored red, and points from varied cuts are colored blue.

(b) Distribution of the differences of Σs from the two ϕ cuts is fitted with a Gaussian function.

Figure 31: Systematic uncertainties of Σ from ϕ Cut.

During the fitting process of ϕ to extract observable asymmetry, the gaps in the detector sector are cut off. For this analysis, we divide the complete range ϕ from $-\pi$ to π into 30 bins of equally sized bins, labeled 1 to 30. Bins 3, 8, 13, 18, 23, and 28 are discarded because they cover the coil regions of the CLAS torus magnet; these bins cover the azimuthal ranges of $-\pi + \frac{4\pi}{30} * N$ to $-\pi + \frac{6\pi}{30} * N$ where N is the CLAS Sector number (ranging from 1 to 6). To study the effect of this cut, another cut in ϕ was applied to examine its influence on observables. For this systematic study, the width of each cut range is widened by $\pi/30$ on both sides in each sector, that is, the cut around the coil regions is doubled, covering $-\pi + \frac{3\pi}{30} * N$ to $-\pi + \frac{7\pi}{30} * N$.

The Σ results of these two ϕ cuts are compared and the differences are fitted with a normal distribution, as shown in Fig. 31. The standard deviation is 0.006. The differences of G from the same two sets of cuts ϕ are fitted and shown in Fig. 32. The standard deviation is 0.014.

In summary, the systematic uncertainty of the cut ϕ is 0.006 and 0.014 for Σ and G, respectively.

3.5 Systematic uncertainty of target polarization

The total systematic uncertainty of 6.0% is quoted for the polarization of H and D as in Ref. [8]. The details of all the uncertainties are listed in Tab. 3.

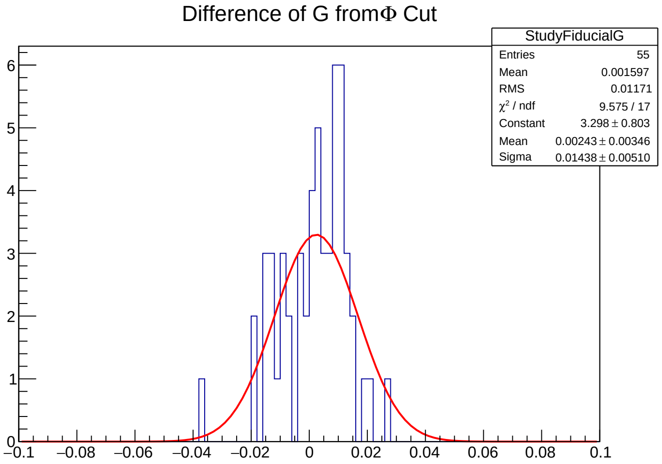

Figure 32: Distribution of the differences of Gs from the ϕ cuts is fitted with a Gaussian function.

3.6 Systematic uncertainty of beam polarization

The technique of generating linear polarized photon beams using the coherent bremsstrahlung effect of electron scattering off a thin diamond radiator has been used at MAMI (Mainz Microtron) and JLab. In these experiments, the linear photon polarization is obtained by fitting the relative intensity spectrum over the tagged photon-energy range, while accounting for specific beam parameters and radiator properties. The lattice-vector calculation in the ANB (Analytic Bremsstrahlung) fit, used at MAMI and JLab, shows an intrinsic uncertainty of 5% [10, 11, 12]. The diamond crystals mounted at CLAS showed short-term fluctuations of the coherent edge. Therefore the ANB fit was effectively performed on the envelope of E-counter enhancement spectra, taken at 2-second intervals. This adds another uncertainty of about 6% [13]. Therefore, the total systematic uncertainties of beam polarization is about 8%.

3.7 Summary of systematic uncertainties

The systematic uncertainties studied in this work include two categories. One comprises of the uncertainties resulting from the choice of various cuts, which are applied in this analysis, the other from uncertainties in beam and target polarization. The uncertainties in the second category relate to multiplicative factors, beam polarization P_γ and target polarization P_n, in the asymmetry formulas, they are reported as relative uncertainties. The other uncertainties result in changes of the yields, which are used to calculate the asymmetries and reported as absolute values. For comparison of these errors only, an

Uncertainties in reference to Thermal Equilibrium (TE) measurement:

PD noise	0.3%	white noise in PD NMR while in HDice Lab
Temperature	0.2%	drift, thermal gradients in HD from radiant heat load
H background	0.4%	H bkg with no target
Stoichiometry	0.1%	deviation of H:D of 1:1, due to H2 and D2 impurities
Bkg subtraction	0.6%	Err in signal from imperfect separation of bkg
Imcomplete relaxation	0.5%	T1 for TE measurement can be comparable to sweep time

Uncertainties in measurement of frozen-spin(FS) signal:

IBC noise	0.6%	residual effect of white noise in IBC NMR and PD
Hall-B noise jumps	0.5%	Variation in signal area after correction for signal jumps
Circuit non-linearity	4.0%	From the quadratic dependence of the circuit transducer gain
RF inhomogeneity	1.4%	Field inhomogeneity
RF depolarization	0.1%	Residual uncorrected decrement from repeated RF sweeps

Uncertainties in relating FS signal to TE measurement:

Circuit drift	1.8%	Variation from connecting FS signal to TE reference
Lock-in gain error	2.9%	SRS 844 manufacturers gain error
Differential ramp-rate	1.0%	Actual ramp rate differs from nominal
TC transfer losses	2.0%	Variation in polarization loss during a TC transfer

Total systematic error	6.0%	For both H and D polarization

Table 3: Systematic uncertainties from HD polarization measurement.

average of Σ and G asymmetries is used to translate the absolute uncertainty value into a relative value. The summary is shown in Tab. 4.

4 Conclusion

This work reports the first measurement of the asymmetry G for the reaction $\gamma D \rightarrow p\pi^-(p)$, as well as Σ in the W range from 1820 MeV to 2220 MeV with a bin size of 80 MeV. The results are binned in $\cos\theta^{cm}$ as a function of θ^{cm}. of the final state π^-.

The results Σ are compared with the results of G13 as shown in Fig. 33. The data points in the solid blue circle with error bars denoting the statistical uncertainties are from this work, while those in the open green triangles are from g13 [14]. The results of the g13 experiment have a finer binning in W. Shows that the results of g14 are clearly consistent with the results of g13. Although these two results are obtained independently, it strongly suggests that both the results of g13 and from this work are correct with a very high confidence. The model predictions from the SAID, MAID and Bonn-Gatchina predictions are also shown and compared to the data.

asymmetry	Σ	G
timing	0.011	0.022
exclusivity	0.012	0.017
missing momentum	0.008	0.013
ϕ cut	0.006	0.014
subtotal	0.019	0.034
beam polarization	8%	8%
target polarization	6%	6%
subtotal	10%	10%

Table 4: List of systematic uncertainties.

Since the measurement of G asymmetry presented here is the first experimental result on this variable with this reaction, no other experimental result is available for comparison; therefore, this is the main result of this work. The results are compared with various model predictions. The recent SAID SM22 description (blue dashed curves) [15], the results of MAID PIONMAID-2021 (magenta dash dotted curves) [16], and the Bonn-Gatchina BnGa-2022-02 predictions (black dotted curves) [17] are also shown in Fig. 34.

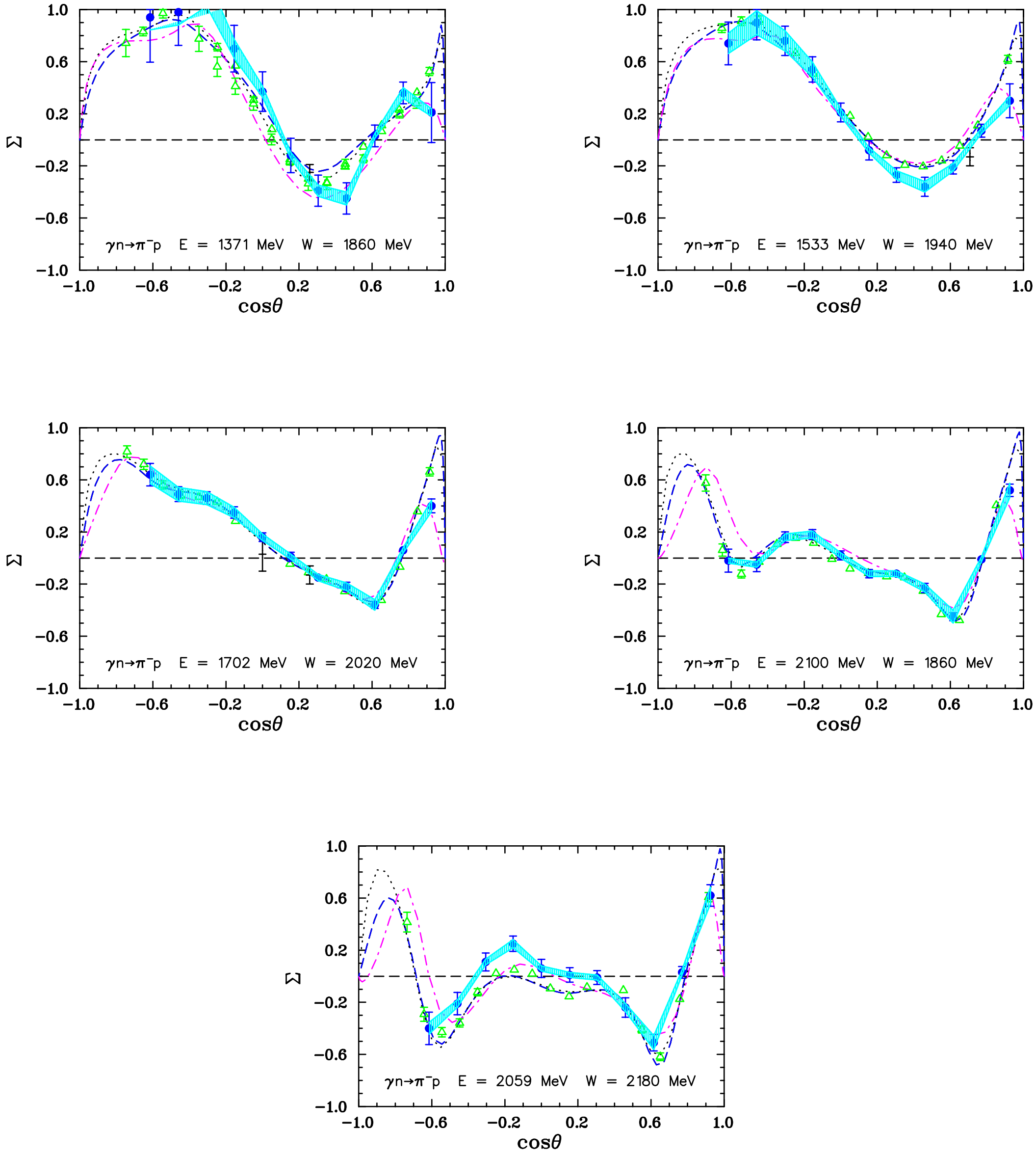

Figure 33: Σ beam asymmetry for the reaction $\vec{\gamma} n \to \pi^- p$ as a function of the pion production angle in the c.m. frame. The experimental data from this work are shown by the blue solid circle with error bars denoting the statistical uncertainties. The cyan bands show systematic uncertainties. Previous measurements: by CLAS (green open triangles) [14], Yerevan, and CEA (black dots) [18, 19]. The recent SAID SM22 description (blue dashed curves) [15], MAID PIONMAID-2021 results (magenta dash-dotted curves) [16], and the Bonn-Gatchina BnGa-2022-02 predictions (black dotted curves) [17] are also shown in the panels.

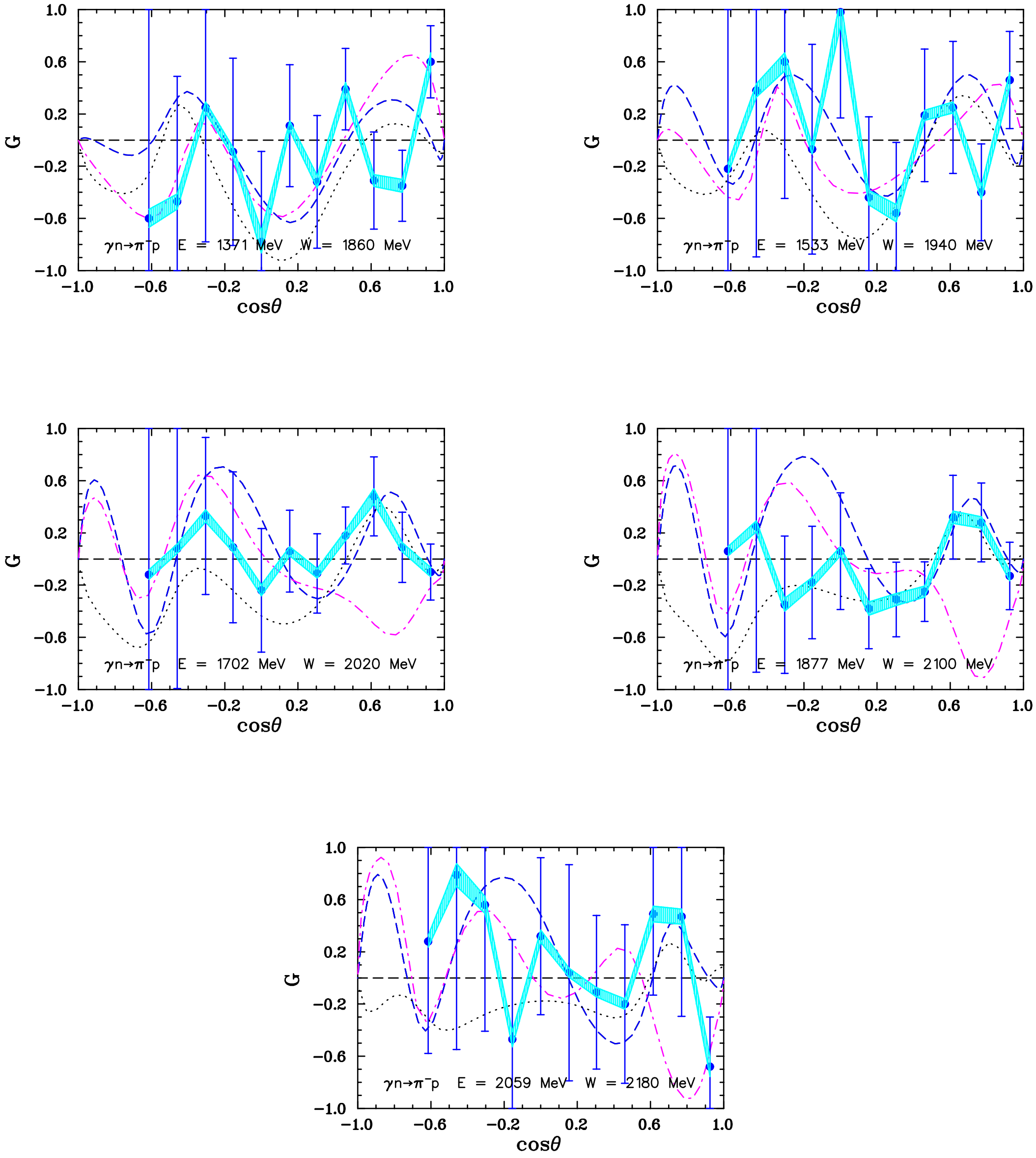

Figure 34: Double-polarization observable, G, for the reaction $\vec{\gamma}\vec{n} \to \pi^- p$ as a function of the pion production angle in the c.m. frame. The different panels denote bins in c.m. energy W $(1860 \pm 40, 1940 \pm 40, 2020 \pm 40, 2100 \pm 40, 2180 \pm 40$ MeV), with the mean values and widths indicated in each plot. The experimental data from this work are shown by the blue solid circle with error bars denoting the statistical uncertainties. The cyan bands show systematic uncertainties. The recent SAID SM22 description (blue dashed curves) [15], MAID PIONMAID-2021 results (magenta dash-dotted curves) [16], and the Bonn-Gatchina BnGa-2022-02 predictions (black dotted curves) [17] are also shown in the panels.

Appendix A Final Σ and G values

Final Σ and G values are listed in the following tables, as well as kinematic variables, statistical uncertainties, and systematic uncertainties.

W (MeV)	$\cos(\theta_\pi)$	Σ	stat	sys
1820 - 1900	-0.54 to -0.38	1.23	0.166	0.124
1820 - 1900	-0.38 to -0.23	1.37	0.182	0.139
1820 - 1900	-0.23 to -0.08	0.68	0.156	0.071
1820 - 1900	-0.08 to 0.08	0.27	0.128	0.033
1820 - 1900	0.08 to 0.23	0.00	0.109	0.019
1820 - 1900	0.23 to 0.38	-0.50	0.093	0.053
1820 - 1900	0.38 to 0.54	-0.34	0.099	0.039
1820 - 1900	0.54 to 0.69	0.06	0.075	0.020
1820 - 1900	0.69 to 0.85	0.33	0.069	0.038
1820 - 1900	0.85 to 1.00	0.40	0.269	0.044

Table 5: Σ at W = 1860 MeV ± 40 MeV.

W (MeV)	$\cos(\theta_\pi)$	Σ	stat	sys
1900 - 1980	-0.54 to -0.38	0.90	0.123	0.092
1900 - 1980	-0.38 to -0.23	0.91	0.087	0.093
1900 - 1980	-0.23 to -0.08	0.63	0.068	0.066
1900 - 1980	-0.08 to 0.08	0.22	0.067	0.029
1900 - 1980	0.08 to 0.23	0.05	0.065	0.020
1900 - 1980	0.23 to 0.38	-0.26	0.050	0.032
1900 - 1980	0.38 to 0.54	-0.34	0.048	0.039
1900 - 1980	0.54 to 0.69	-0.12	0.037	0.022
1900 - 1980	0.69 to 0.85	0.21	0.045	0.028
1900 - 1980	0.85 to 1.00	0.34	0.034	0.039

Table 6: Σ at W = 1940 MeV± 40 MeV.

W (MeV)	$\cos(\theta_\pi)$	Σ	stat	sys
1980 - 2060	-0.54 to -0.38	0.60	0.039	0.063
1980 - 2060	-0.38 to -0.23	0.53	0.037	0.056
1980 - 2060	-0.23 to -0.08	0.35	0.037	0.040
1980 - 2060	-0.08 to 0.08	0.13	0.026	0.023
1980 - 2060	0.08 to 0.23	-0.05	0.025	0.020
1980 - 2060	0.23 to 0.38	-0.16	0.019	0.025
1980 - 2060	0.38 to 0.54	-0.31	0.026	0.037
1980 - 2060	0.54 to 0.69	-0.33	0.020	0.038
1980 - 2060	0.69 to 0.85	0.05	0.019	0.020
1980 - 2060	0.85 to 1.00	0.43	0.039	0.047

Table 7: Σ at W = 2020 MeV ± 40 MeV.

W (MeV)	$\cos(\theta_\pi)$	Σ	stat	sys
2060 - 2140	-0.54 to -0.38	0.04	0.044	0.019
2060 - 2140	-0.38 to -0.23	0.21	0.037	0.029
2060 - 2140	-0.23 to -0.08	0.14	0.036	0.024
2060 - 2140	-0.08 to 0.08	0.00	0.029	0.019
2060 - 2140	0.08 to 0.23	-0.12	0.026	0.023
2060 - 2140	0.23 to 0.38	-0.17	0.021	0.025
2060 - 2140	0.38 to 0.54	-0.30	0.029	0.035
2060 - 2140	0.54 to 0.69	-0.47	0.024	0.050
2060 - 2140	0.69 to 0.85	0.00	0.021	0.019
2060 - 2140	0.85 to 1.00	0.52	0.038	0.055

Table 8: Σ at W = 2100 MeV ± 40 MeV.

W (MeV)	$\cos(\theta_\pi)$	Σ	stat	sys
2140 - 2220	-0.54 to -0.38	-0.35	0.072	0.040
2140 - 2220	-0.38 to -0.23	-0.10	0.059	0.021
2140 - 2220	-0.23 to -0.08	0.02	0.056	0.019
2140 - 2220	-0.08 to 0.08	-0.05	0.055	0.020
2140 - 2220	0.08 to 0.23	-0.11	0.045	0.022
2140 - 2220	0.23 to 0.38	-0.12	0.044	0.022
2140 - 2220	0.38 to 0.54	-0.38	0.052	0.043
2140 - 2220	0.54 to 0.69	-0.60	0.046	0.063
2140 - 2220	0.69 to 0.85	-0.12	0.037	0.023
2140 - 2220	0.85 to 1.00	0.59	0.060	0.062

Table 9: Σ at W = 2180 MeV ± 40 MeV.

W (MeV)	$\cos(\theta_\pi)$	G	stat	sys
1820 - 1900	-0.54 to -0.38	-0.19	0.432	0.039
1820 - 1900	-0.38 to -0.23	-0.22	0.310	0.041
1820 - 1900	-0.23 to -0.08	0.31	0.315	0.046
1820 - 1900	-0.08 to 0.08	0.39	0.277	0.052
1820 - 1900	0.08 to 0.23	0.06	0.220	0.035
1820 - 1900	0.23 to 0.38	0.25	0.181	0.042
1820 - 1900	0.38 to 0.54	0.05	0.149	0.034
1820 - 1900	0.54 to 0.69	0.20	0.166	0.039
1820 - 1900	0.69 to 0.85	0.08	0.133	0.035
1820 - 1900	0.85 to 1.00	-0.52	0.121	0.062

Table 10: G at W = 1860 MeV ± 40 MeV.

W (MeV)	$\cos(\theta_\pi)$	G	stat	sys
1900 - 1980	-0.54 to -0.38	0.37	0.386	0.050
1900 - 1980	-0.38 to -0.23	-0.02	0.288	0.034
1900 - 1980	-0.23 to -0.08	0.31	0.266	0.046
1900 - 1980	-0.08 to 0.08	-0.10	0.230	0.036
1900 - 1980	0.08 to 0.23	0.29	0.185	0.045
1900 - 1980	0.23 to 0.38	0.21	0.165	0.040
1900 - 1980	0.38 to 0.54	0.17	0.125	0.038
1900 - 1980	0.54 to 0.69	-0.29	0.153	0.045
1900 - 1980	0.69 to 0.85	0.00	0.126	0.034
1900 - 1980	0.85 to 1.00	0.05	0.115	0.034

Table 11: G at W = 1940 MeV ± 40 MeV.

W (MeV)	$\cos(\theta_\pi)$	G	stat	sys
1980 - 2060	-0.54 to -0.38	0.09	0.338	0.035
1980 - 2060	-0.38 to -0.23	-0.02	0.247	0.034
1980 - 2060	-0.23 to -0.08	-0.11	0.210	0.036
1980 - 2060	-0.08 to 0.08	0.28	0.200	0.044
1980 - 2060	0.08 to 0.23	-0.03	0.151	0.034
1980 - 2060	0.23 to 0.38	0.16	0.137	0.038
1980 - 2060	0.38 to 0.54	0.03	0.104	0.034
1980 - 2060	0.54 to 0.69	-0.44	0.140	0.056
1980 - 2060	0.69 to 0.85	-0.20	0.117	0.039
1980 - 2060	0.85 to 1.00	0.36	0.104	0.050

Table 12: G at W = 2020 MeV ± 40 MeV.

W (MeV)	$\cos(\theta_\pi)$	G	stat	sys
2060 - 2140	-0.54 to -0.38	0.03	0.369	0.034
2060 - 2140	-0.38 to -0.23	-0.34	0.260	0.048
2060 - 2140	-0.23 to -0.08	0.32	0.213	0.047
2060 - 2140	-0.08 to 0.08	0.15	0.210	0.037
2060 - 2140	0.08 to 0.23	0.11	0.166	0.036
2060 - 2140	0.23 to 0.38	0.20	0.142	0.040
2060 - 2140	0.38 to 0.54	0.16	0.118	0.037
2060 - 2140	0.54 to 0.69	-0.27	0.157	0.043
2060 - 2140	0.69 to 0.85	-0.23	0.139	0.041
2060 - 2140	0.85 to 1.00	0.29	0.117	0.045

Table 13: G at W = 2100 MeV ± 40 MeV.

W (MeV)	$\cos(\theta_\pi)$	G	stat	sys
2140 - 2220	-0.54 to -0.38	-0.33	0.561	0.048
2140 - 2220	-0.38 to -0.23	0.00	0.418	0.034
2140 - 2220	-0.23 to -0.08	0.13	0.311	0.037
2140 - 2220	-0.08 to 0.08	0.12	0.297	0.036
2140 - 2220	0.08 to 0.23	0.43	0.288	0.055
2140 - 2220	0.23 to 0.38	0.40	0.236	0.053
2140 - 2220	0.38 to 0.54	-0.50	0.224	0.061
2140 - 2220	0.54 to 0.69	-0.23	0.269	0.041
2140 - 2220	0.69 to 0.85	-0.26	0.262	0.043
2140 - 2220	0.85 to 1.00	0.13	0.196	0.036

Table 14: G at W = 2180 MeV ± 40 MeV.

Appendix B Fitting $\Sigma cos(2\phi)$ and $Gsin(2\phi)$

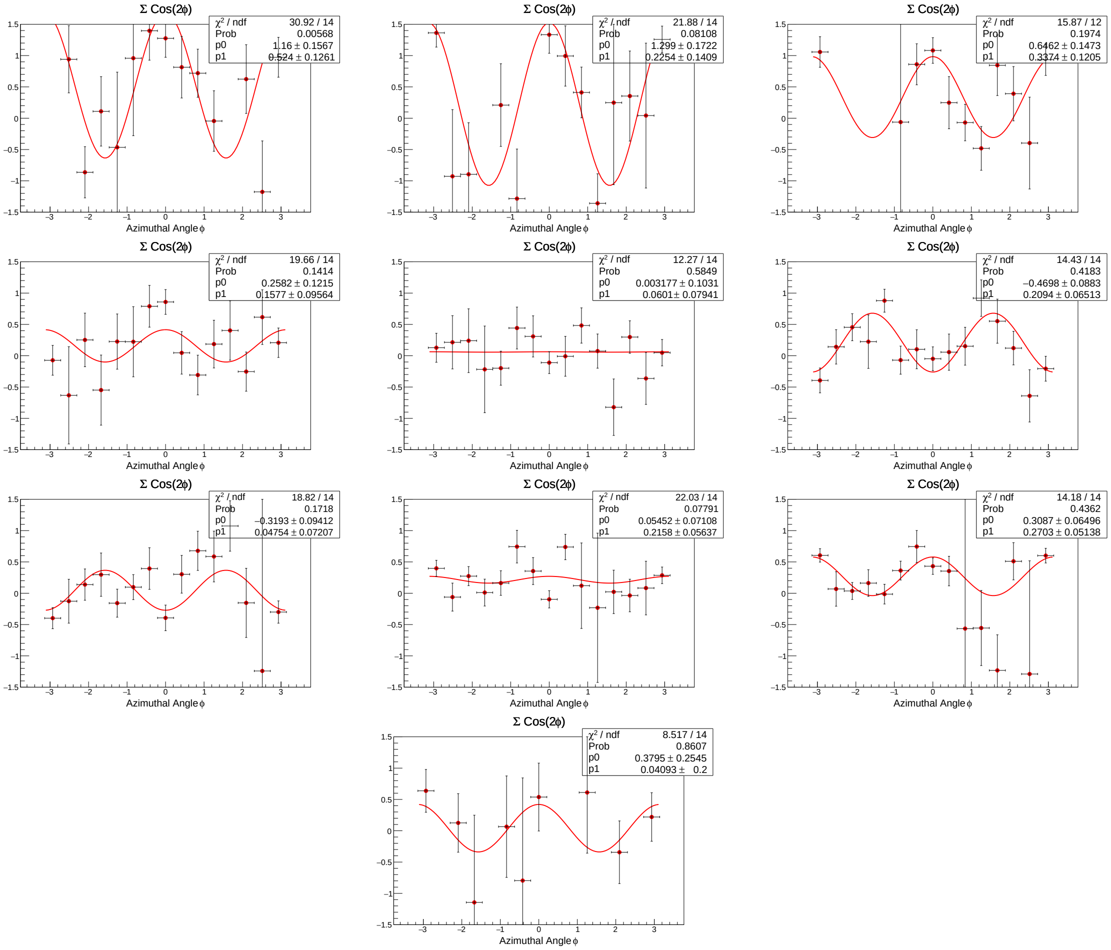

Figure 35: Fitting Σ with W from 1820 - 1900 MeV at different angle of pion in the center-of-mass frame. The different panels denote bins in $cos(\theta_\pi)$: -0.54 to -0.38, -0.38 to -0.23, -0.23 to -0.08, -0.08 to 0.08, 0.08 to 0.23, 0.23 to 0.38, 0.38 to 0.54, 0.54 to 0.69, 0.69 to 0.85, and 0.85 to 1.00.

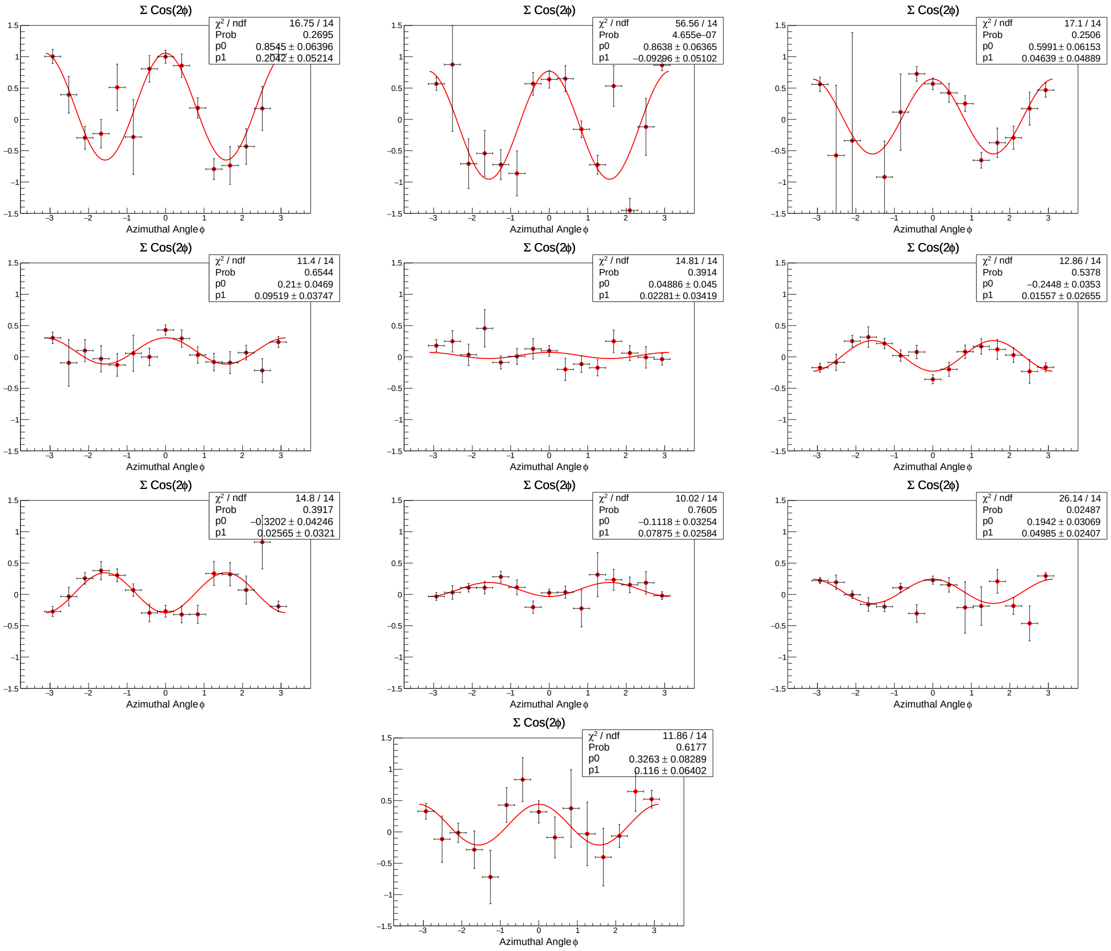

Figure 36: Fitting Σ with W from 1900 - 1980 MeV at different angle of pion in the center-of-mass frame. The different panels denote bins in $cos(\theta_\pi)$: -0.54 to -0.38, -0.38 to -0.23, -0.23 to -0.08, -0.08 to 0.08, 0.08 to 0.23, 0.23 to 0.38, 0.38 to 0.54, 0.54 to 0.69, 0.69 to 0.85, and 0.85 to 1.00.

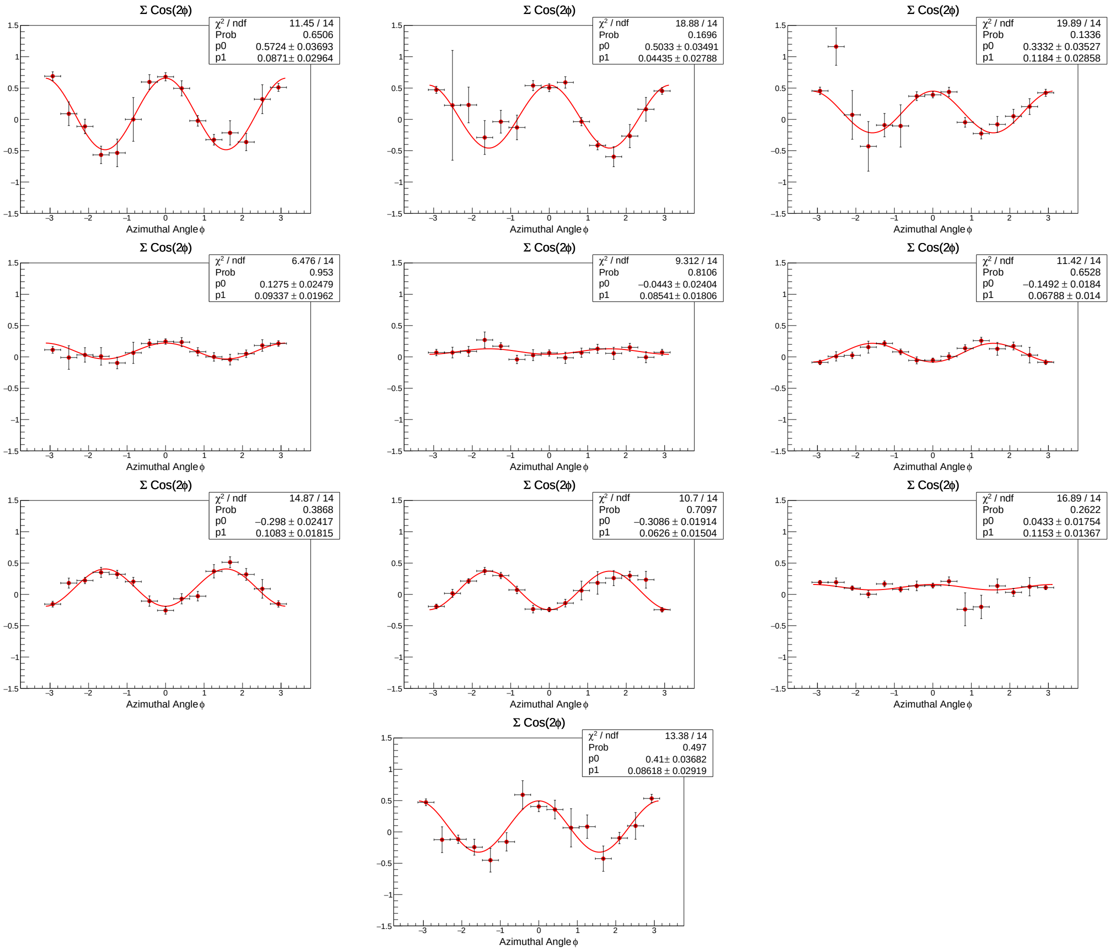

Figure 37: Fitting Σ with W from 1980 - 2060 MeV at different angle of pion in the center-of-mass frame. The different panels denote bins in $cos(\theta_\pi)$: -0.54 to -0.38, -0.38 to -0.23, -0.23 to -0.08, -0.08 to 0.08, 0.08 to 0.23, 0.23 to 0.38, 0.38 to 0.54, 0.54 to 0.69, 0.69 to 0.85, and 0.85 to 1.00.

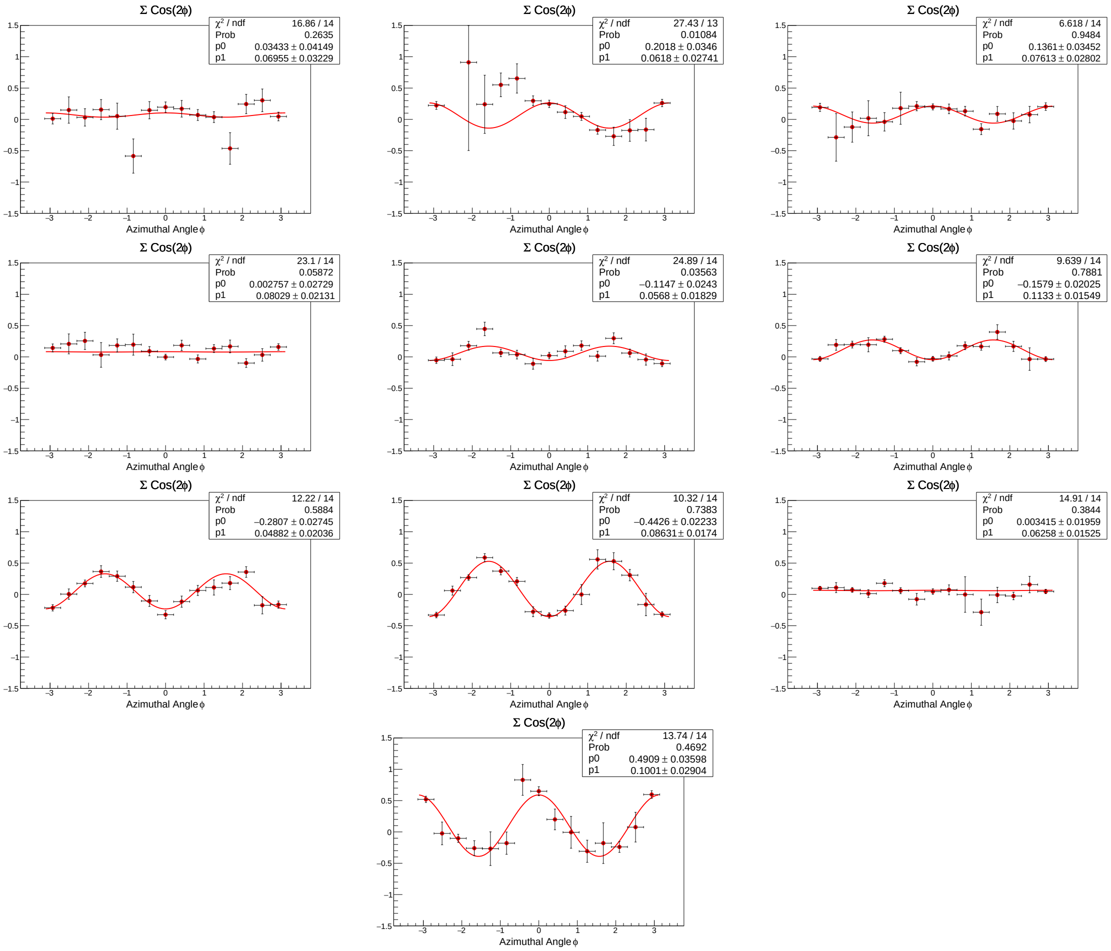

Figure 38: Fitting Σ with W from 2060 - 2140 MeV at different angle of pion in the center-of-mass frame. The different panels denote bins in $cos(\theta_\pi)$: -0.54 to -0.38, -0.38 to -0.23, -0.23 to -0.08, -0.08 to 0.08, 0.08 to 0.23, 0.23 to 0.38, 0.38 to 0.54, 0.54 to 0.69, 0.69 to 0.85, and 0.85 to 1.00.

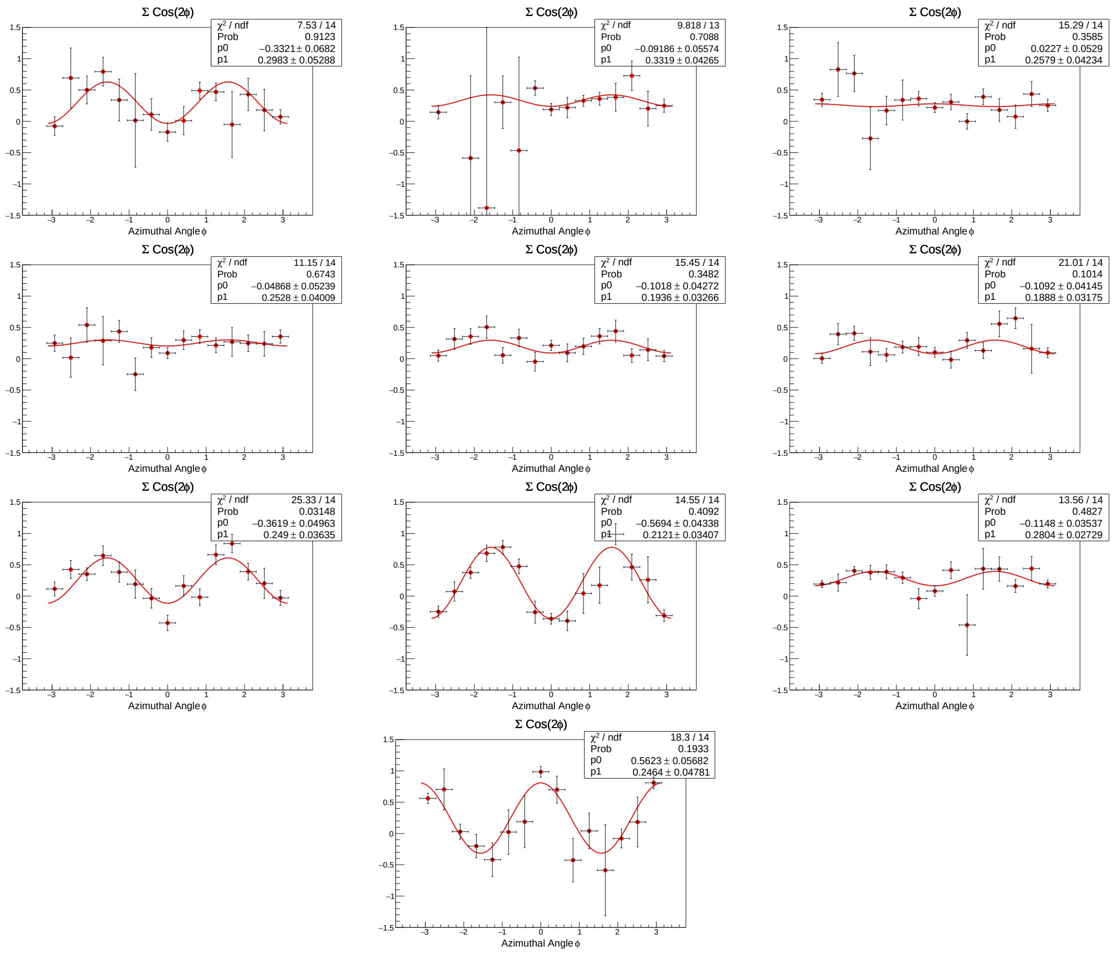

Figure 39: Fitting Σ with W from 2140 - 2220 MeV at different angle of pion in the center-of-mass frame. The different panels denote bins in $cos(\theta_\pi)$: -0.54 to -0.38, -0.38 to -0.23, -0.23 to -0.08, -0.08 to 0.08, 0.08 to 0.23, 0.23 to 0.38, 0.38 to 0.54, 0.54 to 0.69, 0.69 to 0.85, and 0.85 to 1.00.

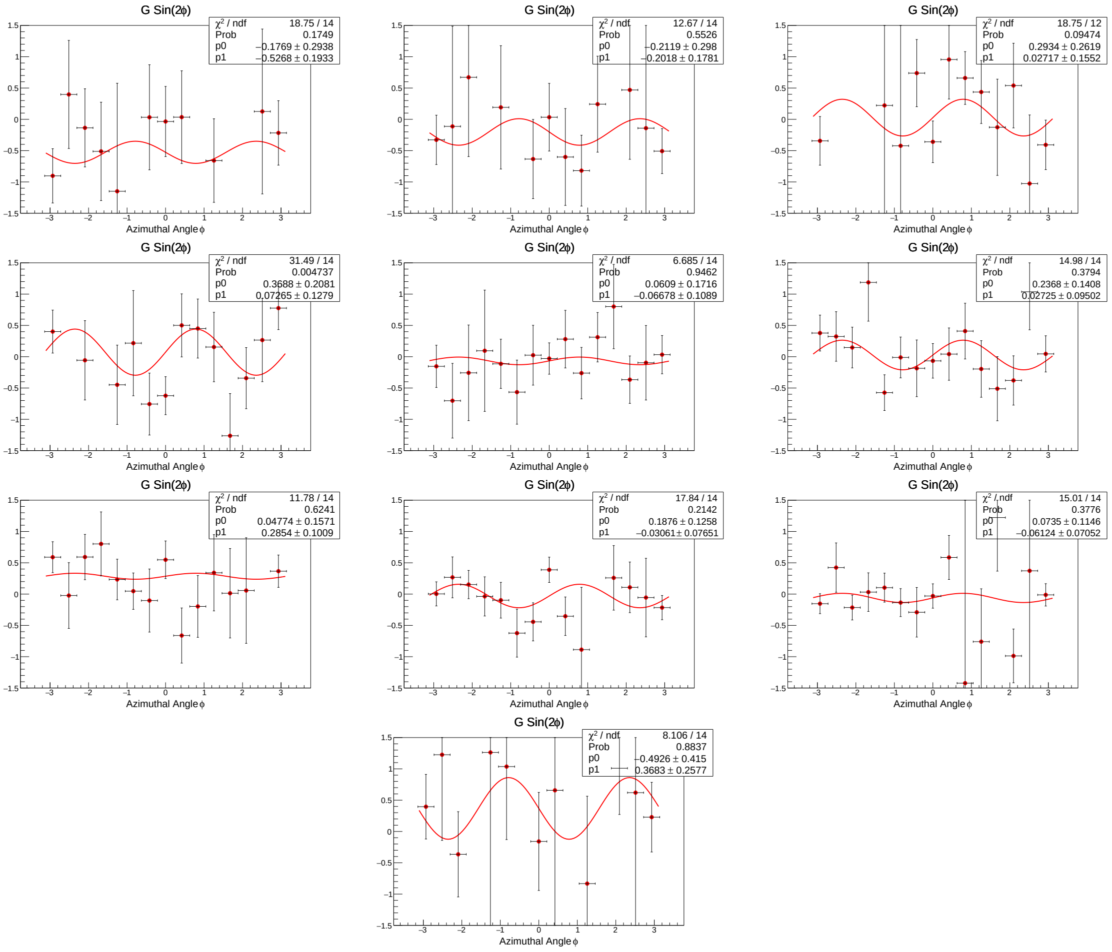

Figure 40: Fitting G with W from 1820 - 1900 MeV at different angle of pion in the center-of-mass frame. The different panels denote bins in $cos(\theta_\pi)$: -0.54 to -0.38, -0.38 to -0.23, -0.23 to -0.08, -0.08 to 0.08, 0.08 to 0.23, 0.23 to 0.38, 0.38 to 0.54, 0.54 to 0.69, 0.69 to 0.85, and 0.85 to 1.00.

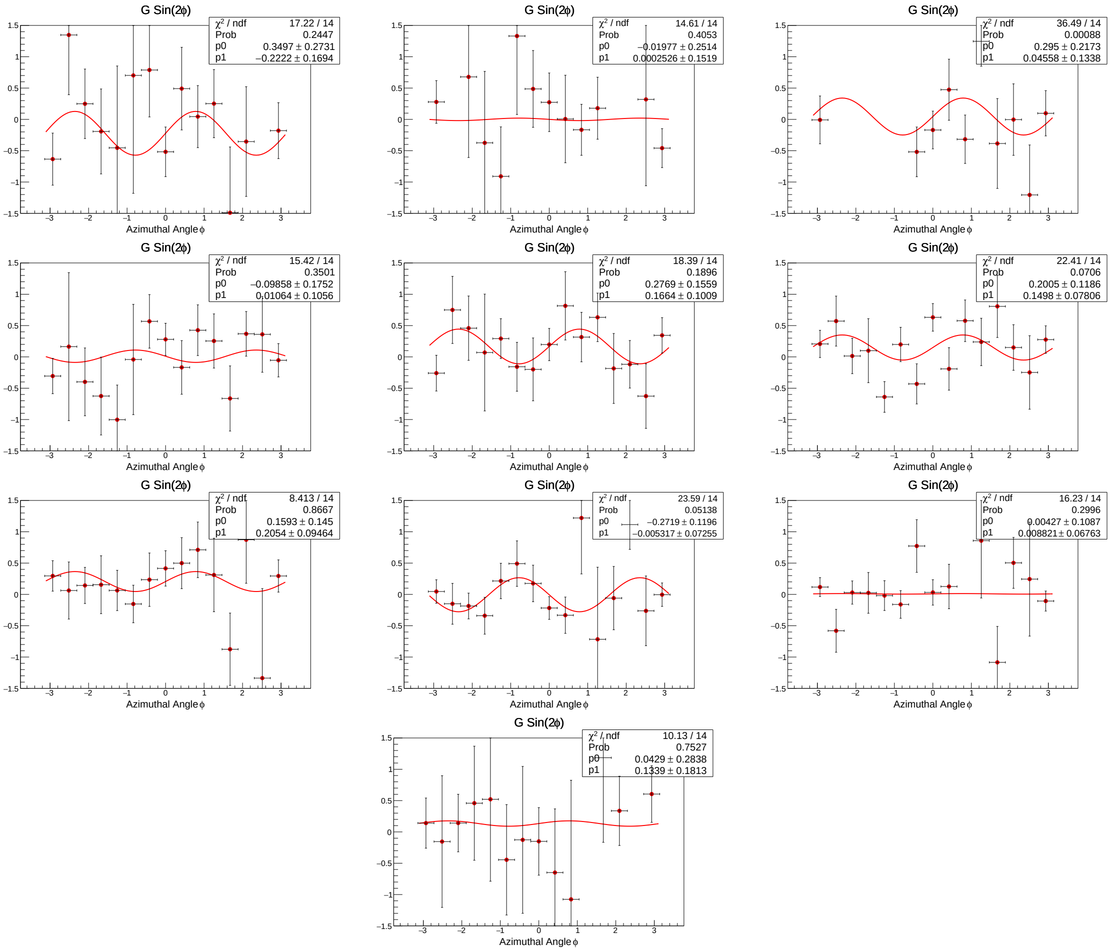

Figure 41: Fitting G with W from 1900 - 1980 MeV at different angle of pion in the center-of-mass frame. The different panels denote bins in $cos(\theta_\pi)$: -0.54 to -0.38, -0.38 to -0.23, -0.23 to -0.08, -0.08 to 0.08, 0.08 to 0.23, 0.23 to 0.38, 0.38 to 0.54, 0.54 to 0.69, 0.69 to 0.85, and 0.85 to 1.00.

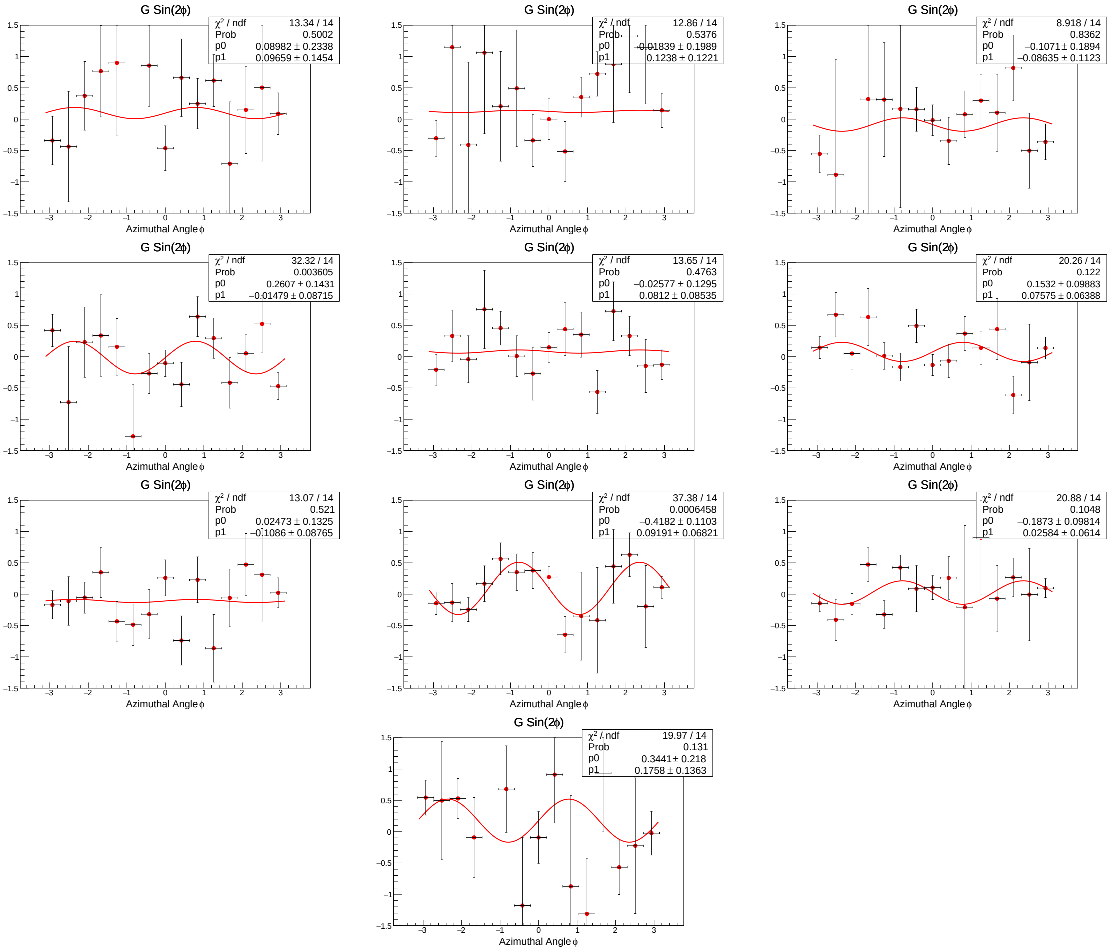

Figure 42: Fitting G with W from 1980 - 2060 MeV at different angle of pion in the center-of-mass frame. The different panels denote bins in $cos(\theta_\pi)$: -0.54 to -0.38, -0.38 to -0.23, -0.23 to -0.08, -0.08 to 0.08, 0.08 to 0.23, 0.23 to 0.38, 0.38 to 0.54, 0.54 to 0.69, 0.69 to 0.85, and 0.85 to 1.00.

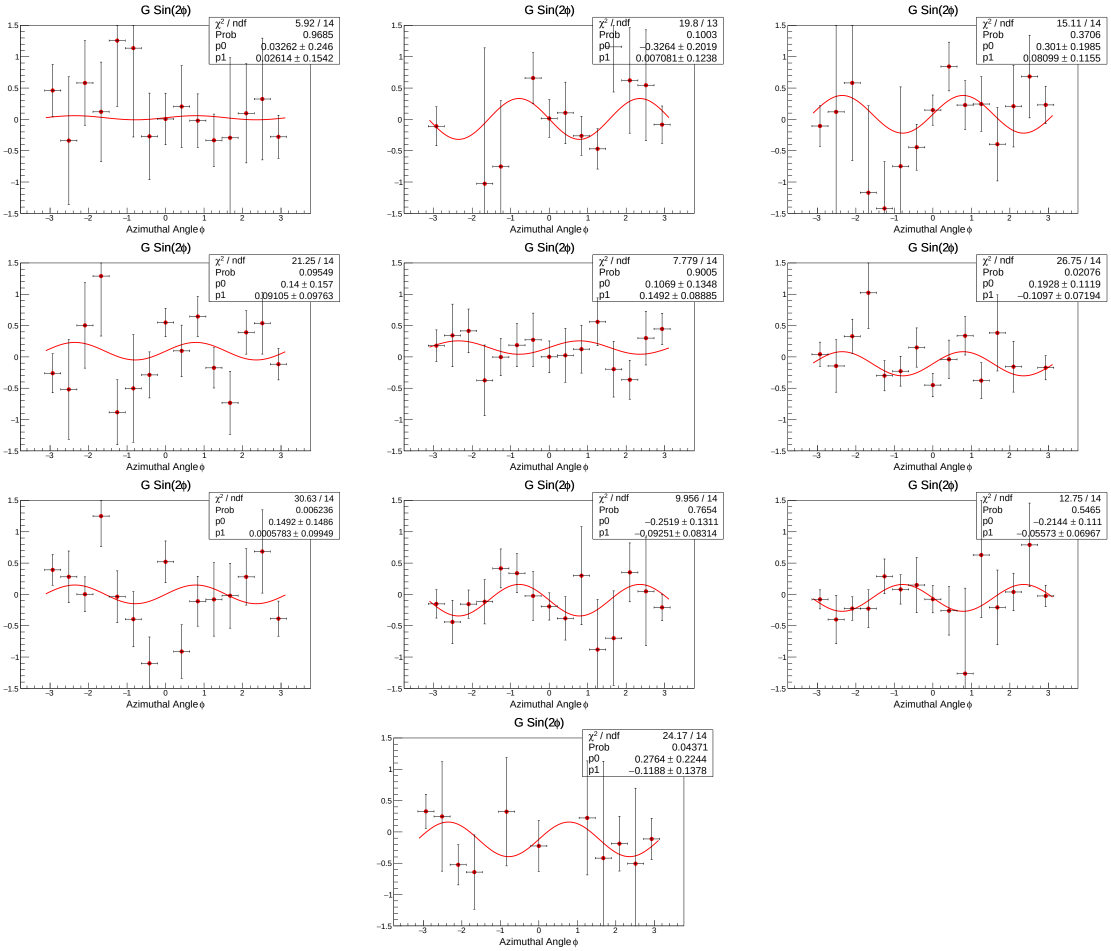

Figure 43: Fitting G with W from 2060 - 2140 MeV at different angle of pion in the center-of-mass frame. The different panels denote bins in $cos(\theta_\pi)$: -0.54 to -0.38, -0.38 to -0.23, -0.23 to -0.08, -0.08 to 0.08, 0.08 to 0.23, 0.23 to 0.38, 0.38 to 0.54, 0.54 to 0.69, 0.69 to 0.85, and 0.85 to 1.00.

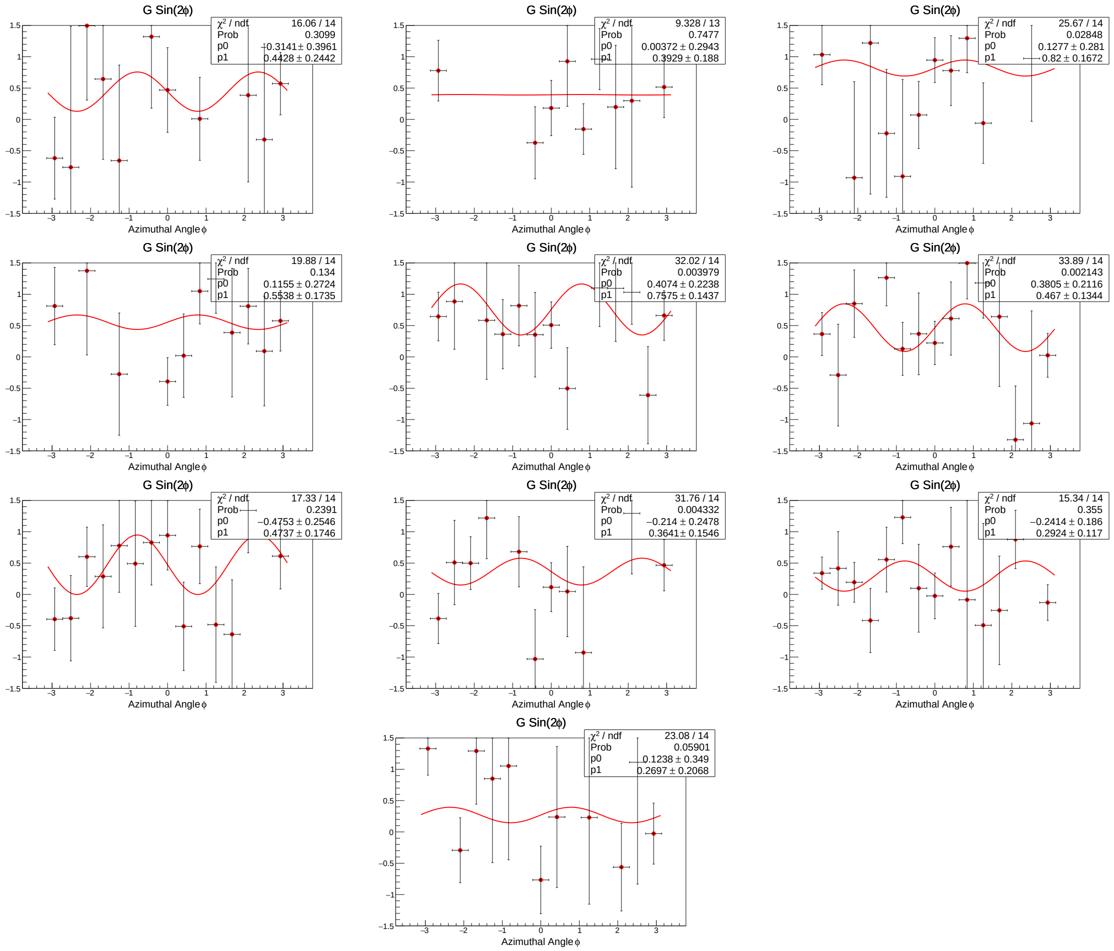

Figure 44: Fitting G with W from 2140 - 2220 MeV at different angle of pion in the center-of-mass frame. The different panels denote bins in $cos(\theta_\pi)$: -0.54 to -0.38, -0.38 to -0.23, -0.23 to -0.08, -0.08 to 0.08, 0.08 to 0.23, 0.23 to 0.38, 0.38 to 0.54, 0.54 to 0.69, 0.69 to 0.85, and 0.85 to 1.00.

Appendix C ϕ distribution of different configurations

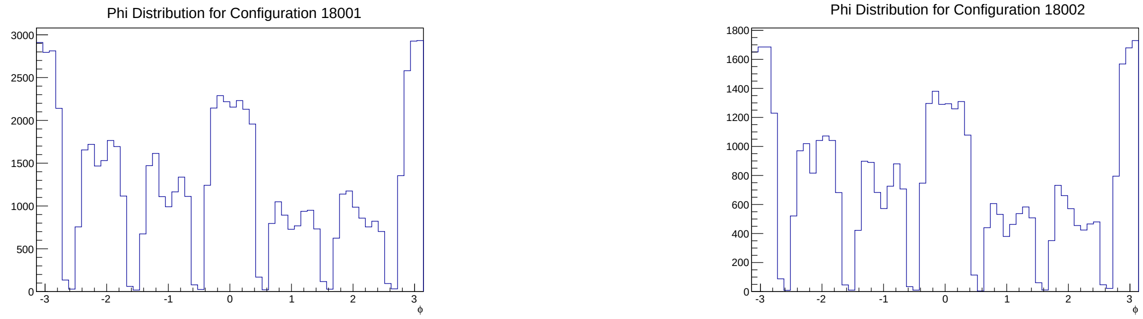

(a) ϕ distribution with beam coherent edge 1800 MeV, parallel beam polarization, and target +Z/-Z (left/right).

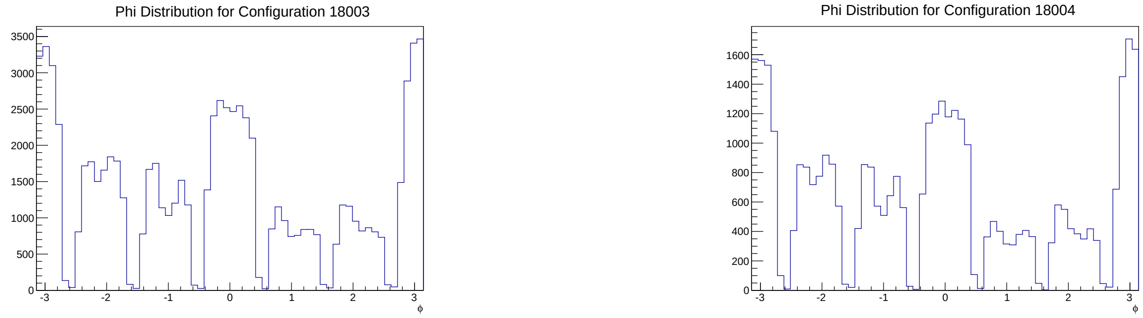

(b) ϕ distribution with beam coherent edge 1800 MeV, perpendicular beam polarization, and target +Z/-Z (left/right).

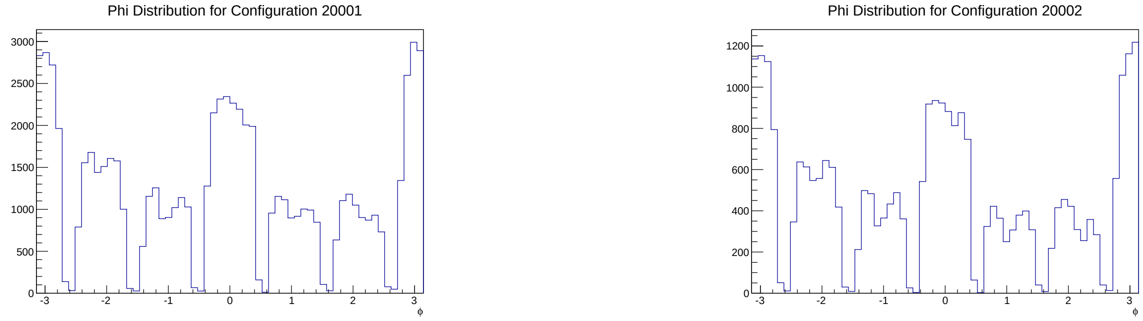

(c) ϕ distribution with beam coherent edge 2000 MeV, parallel beam polarization, and target +Z/-Z (left/right).

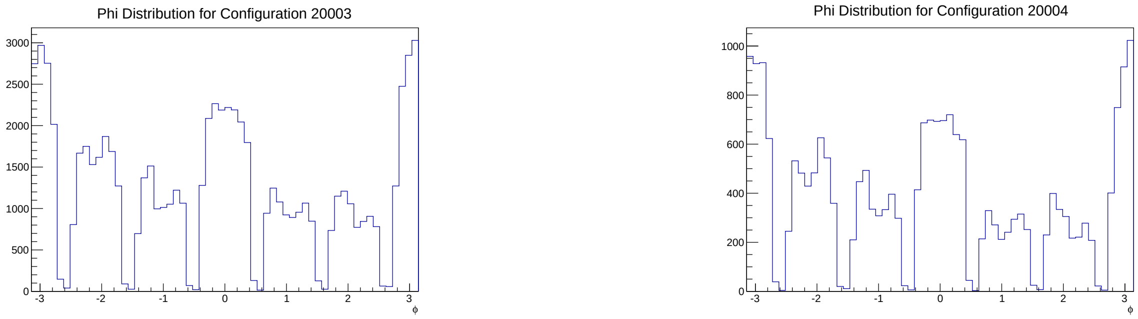

(d) ϕ distribution with beam coherent edge 2000 MeV, perpendicular beam polarization, and target +Z/-Z (left/right).

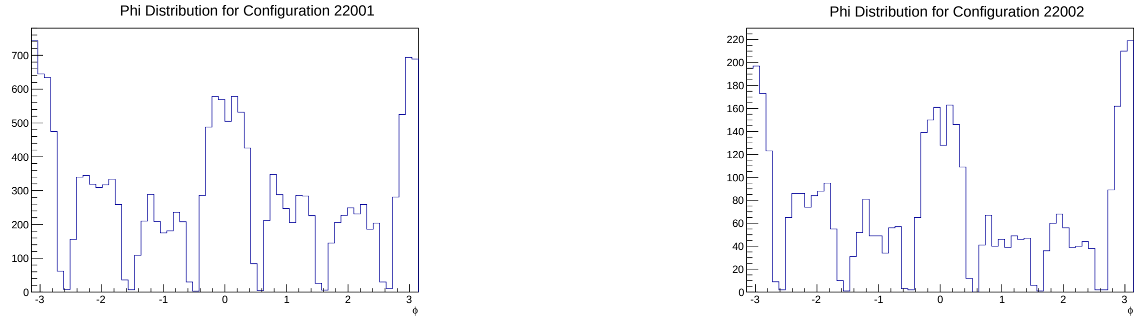

(e) ϕ distribution with beam coherent edge 2200 MeV, parallel beam polarization, and target +Z/-Z (left/right).

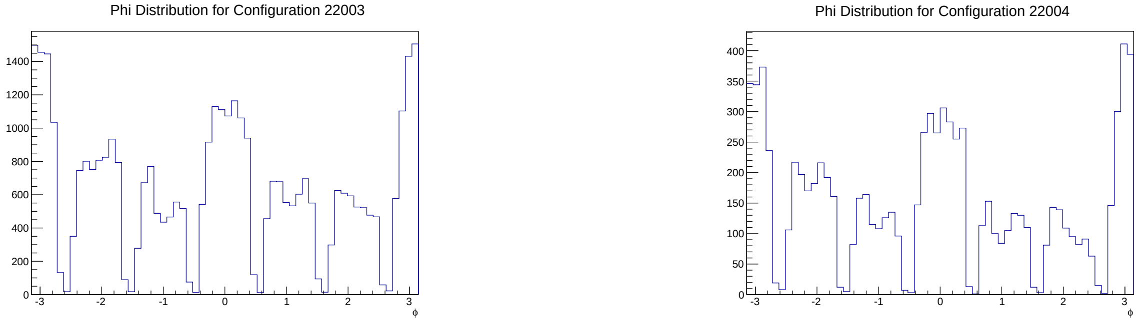

(f) ϕ distribution with beam coherent edge 2200 MeV, perpendicular beam polarization, and target +Z/-Z (left/right).

Appendix D Ratio of acceptance

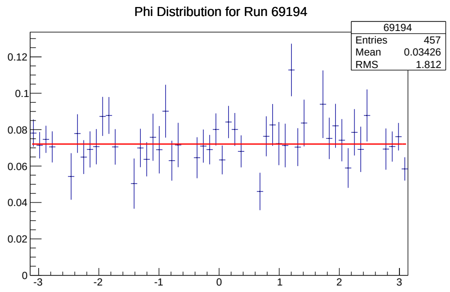

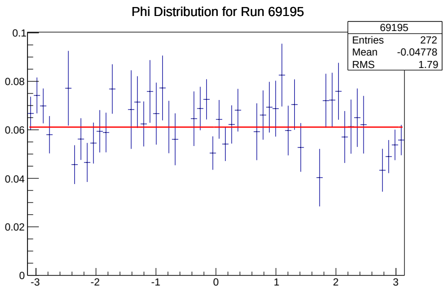

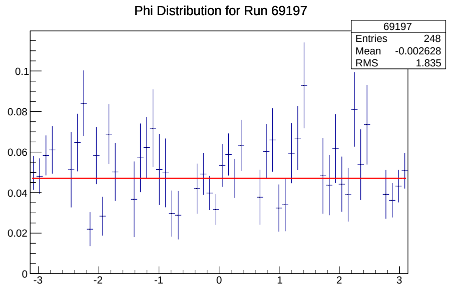

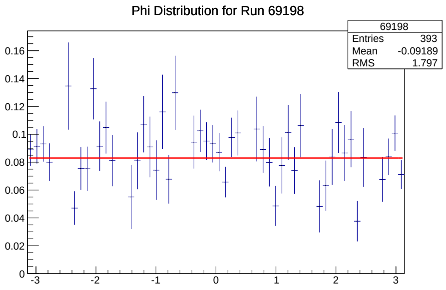

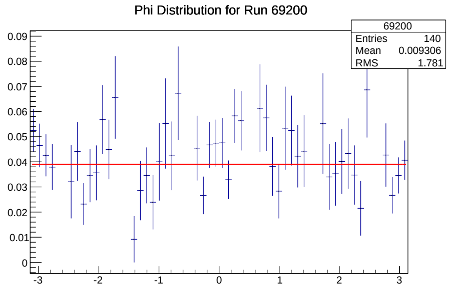

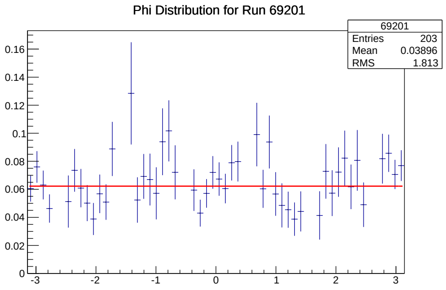

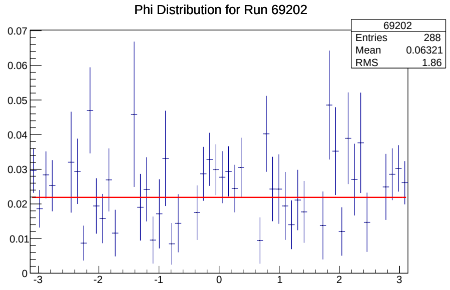

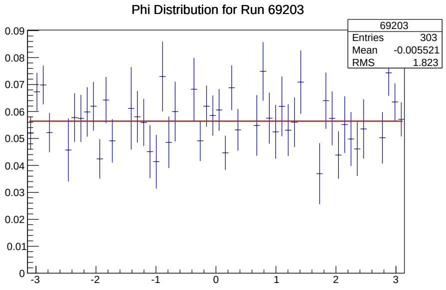

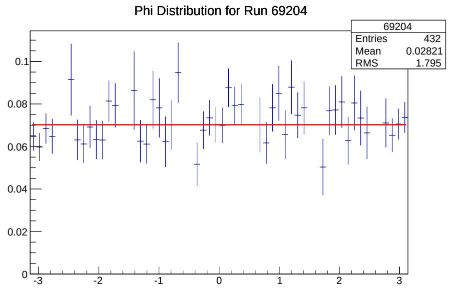

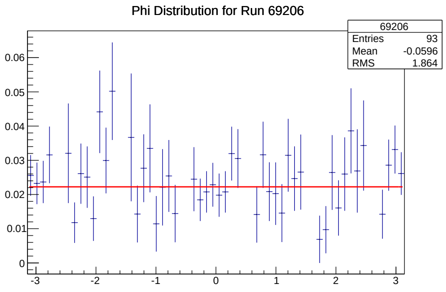

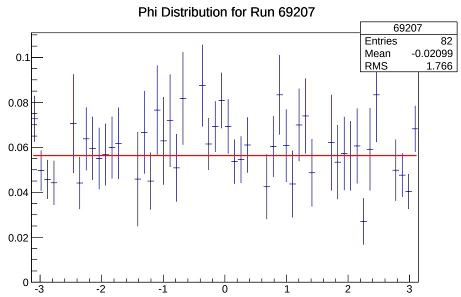
Phi Distribution for Run 69207

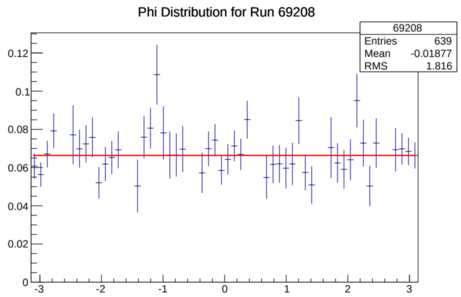
Phi Distribution for Run 69208

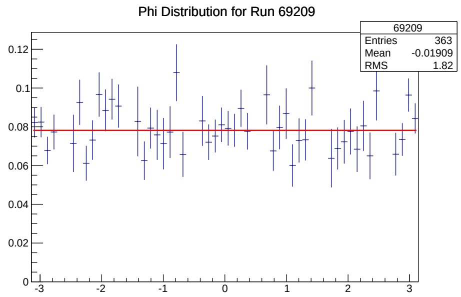
Phi Distribution for Run 69209

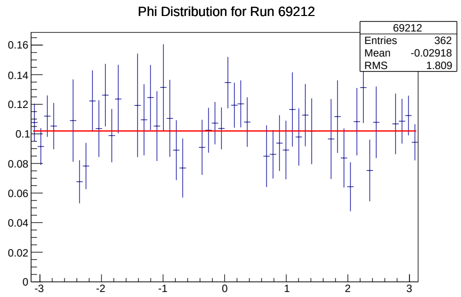
Phi Distribution for Run 69212

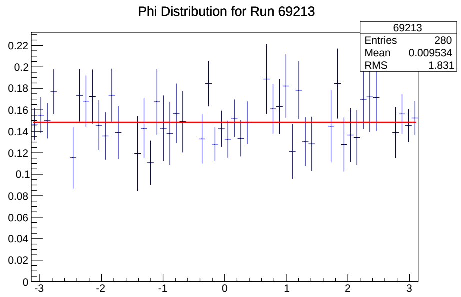
Phi Distribution for Run 69213

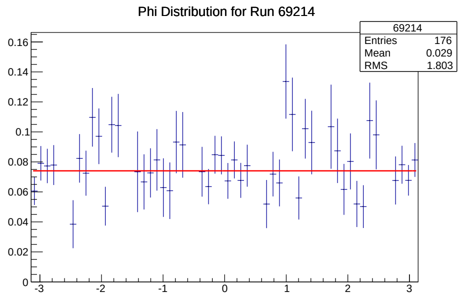
Phi Distribution for Run 69214

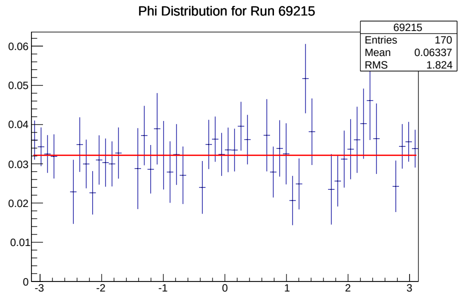
Phi Distribution for Run 69215

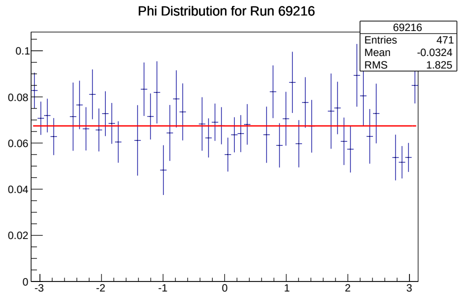
Phi Distribution for Run 69216

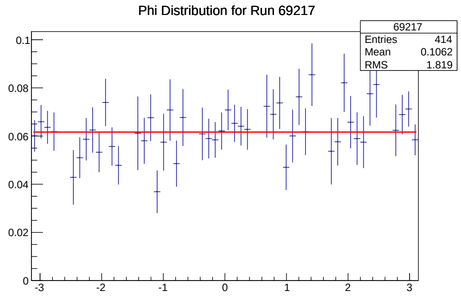
Phi Distribution for Run 69217

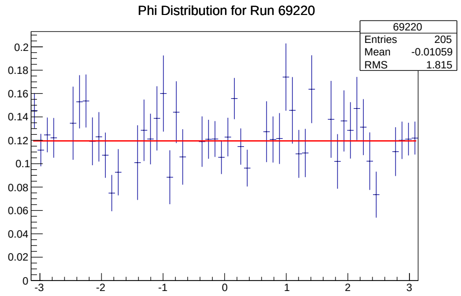
Phi Distribution for Run 69220

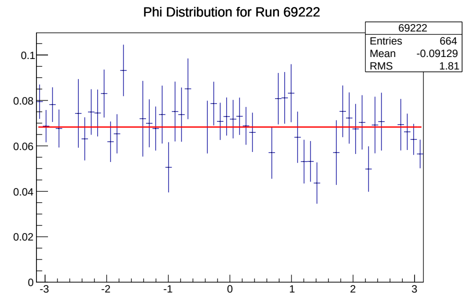
Phi Distribution for Run 69222

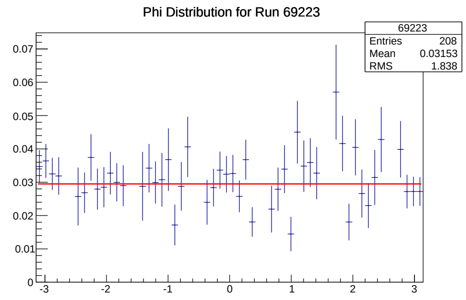
Phi Distribution for Run 69223

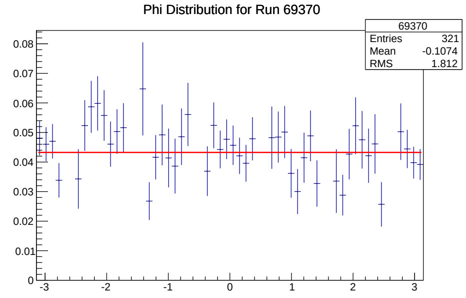
Phi Distribution for Run 69370

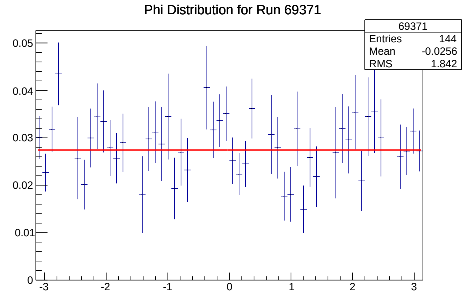
Phi Distribution for Run 69371

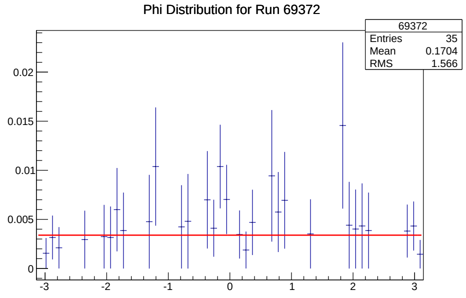
Phi Distribution for Run 69372

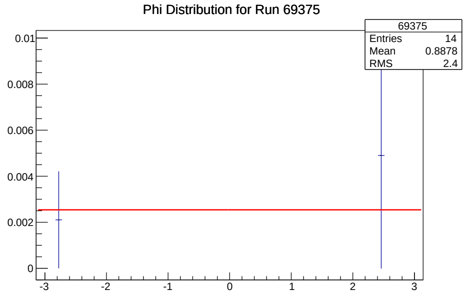
Phi Distribution for Run 69375

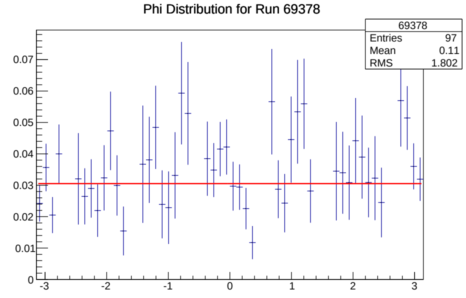
Phi Distribution for Run 69378

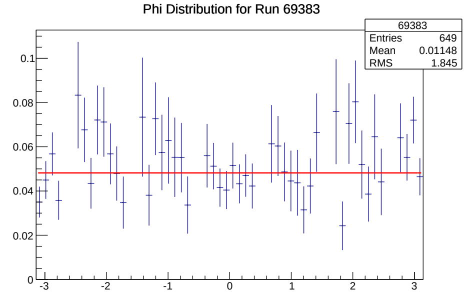
Phi Distribution for Run 69383

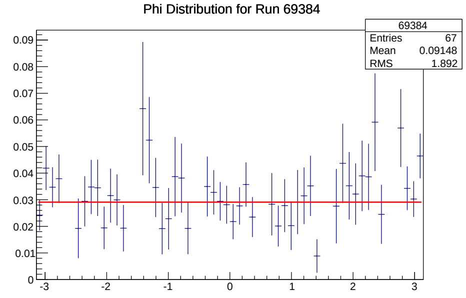
Phi Distribution for Run 69384

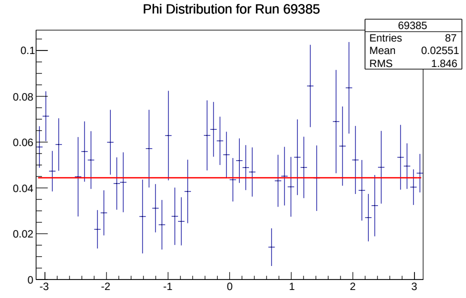
Phi Distribution for Run 69385

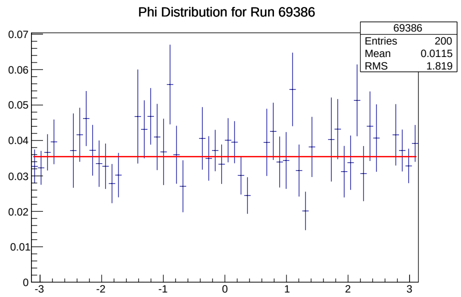
Phi Distribution for Run 69386
69386
Entries 200
Mean 0.0115
RMS 1.819
0
0.01
0.02
0.03
0.04
0.05
0.06
0.07
-3
-2
-1
0
1
2
3

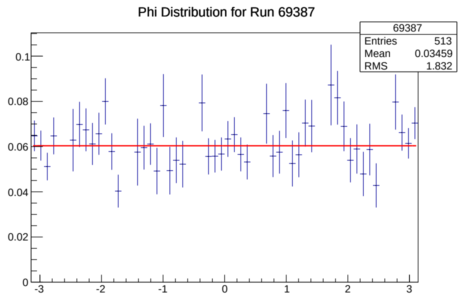
Phi Distribution for Run 69387
69387
Entries 513
Mean 0.03459
RMS 1.832
0
0.02
0.04
0.06
0.08
0.1
-3
-2
-1
0
1
2
3

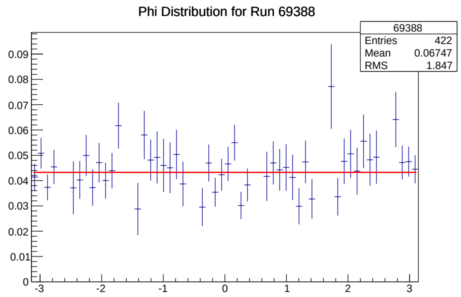
Phi Distribution for Run 69388
69388
Entries 422
Mean 0.06747
RMS 1.847
0
0.01
0.02
0.03
0.04
0.05
0.06
0.07
0.08
0.09
-3
-2
-1
0
1
2
3

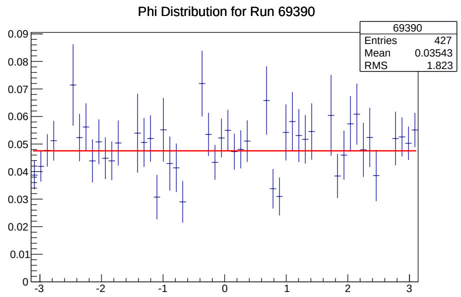
Phi Distribution for Run 69390
69390
Entries 427
Mean 0.03543
RMS 1.823
0
0.01
0.02
0.03
0.04
0.05
0.06
0.07
0.08
0.09
-3
-2
-1
0
1
2
3

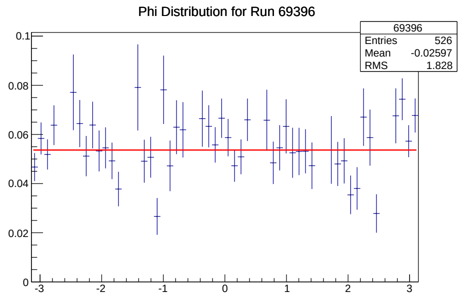
Phi Distribution for Run 69396
69396
Entries 526
Mean -0.02597
RMS 1.828
0
0.02
0.04
0.06
0.08
0.1
-3
-2
-1
0
1
2
3

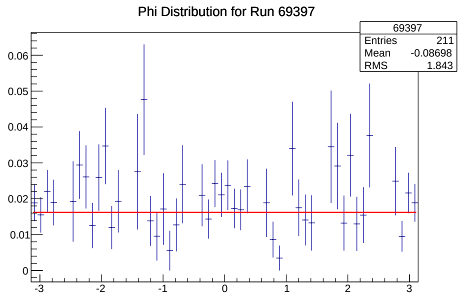
Phi Distribution for Run 69397
69397
Entries 211
Mean -0.08698
RMS 1.843
0
0.01
0.02
0.03
0.04
0.05
0.06
-3
-2
-1
0
1
2
3

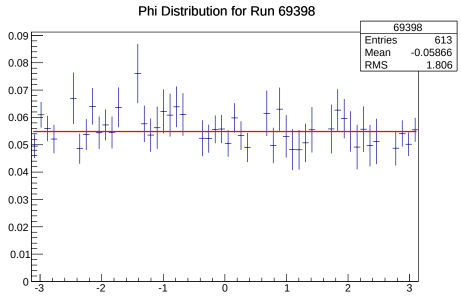
Phi Distribution for Run 69398
69398
Entries 613
Mean -0.05866
RMS 1.806
0
0.01
0.02
0.03
0.04
0.05
0.06
0.07
0.08
0.09
-3
-2
-1
0
1
2
3

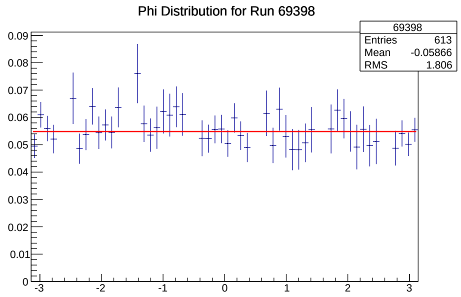
Phi Distribution for Run 69398
69398
Entries 613
Mean -0.05866
RMS 1.806
0
0.01
0.02
0.03
0.04
0.05
0.06
0.07
0.08
0.09
-3
-2
-1
0
1
2
3

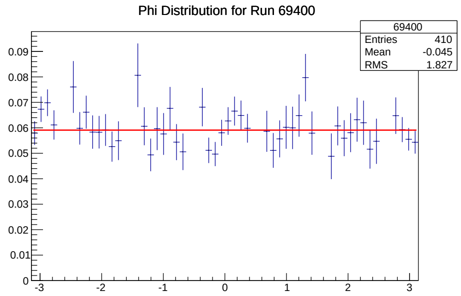
Phi Distribution for Run 69400
69400
Entries 410
Mean -0.045
RMS 1.827
0
0.01
0.02
0.03
0.04
0.05
0.06
0.07
0.08
0.09
-3
-2
-1
0
1
2
3

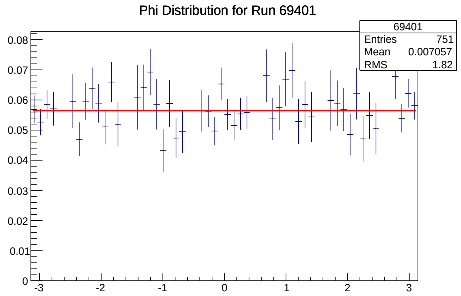
Phi Distribution for Run 69401
69401
Entries 751
Mean 0.007057
RMS 1.82
0
0.01
0.02
0.03
0.04
0.05
0.06
0.07
0.08
-3
-2
-1
0
1
2
3

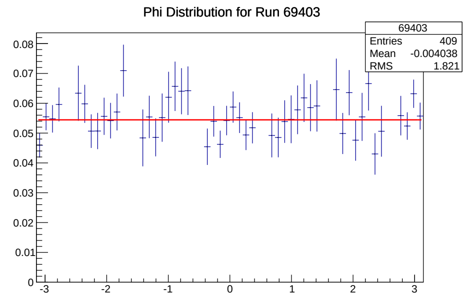
Phi Distribution for Run 69403

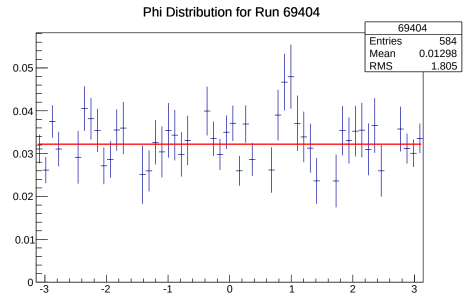
Phi Distribution for Run 69404

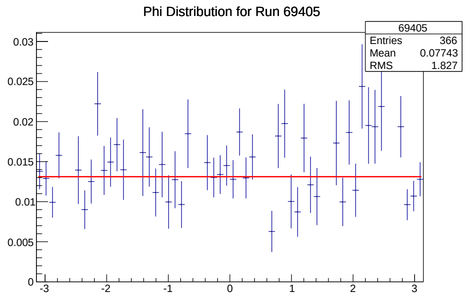
Phi Distribution for Run 69405

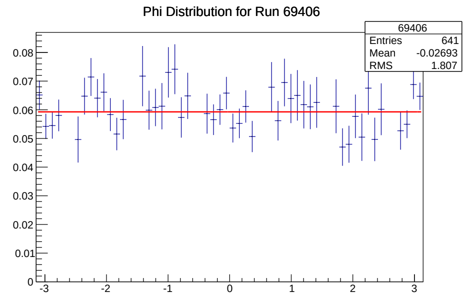
Phi Distribution for Run 69406

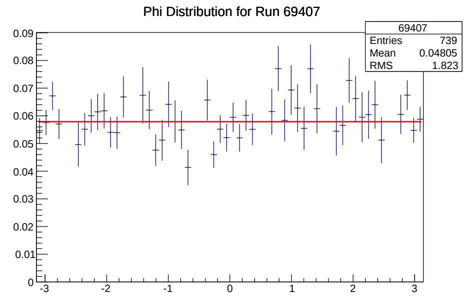
Phi Distribution for Run 69407

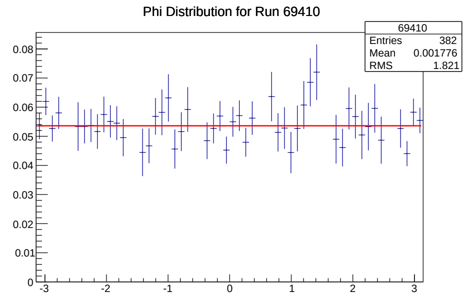
Phi Distribution for Run 69410

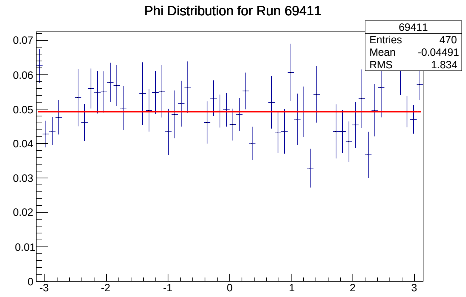
Phi Distribution for Run 69411

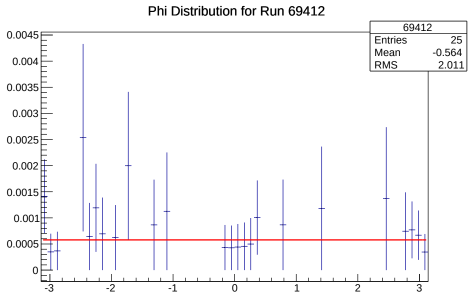
Phi Distribution for Run 69412

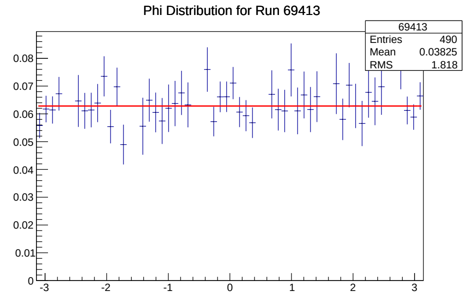
Phi Distribution for Run 69413

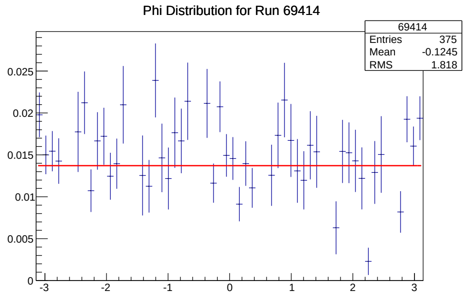
Phi Distribution for Run 69414

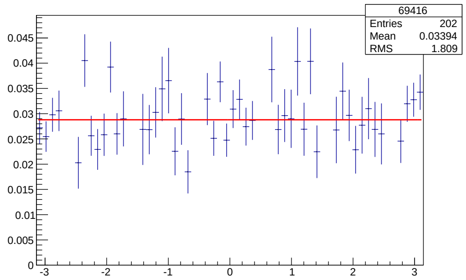
Phi Distribution for Run 69416

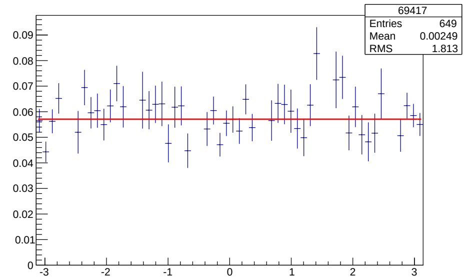
Phi Distribution for Run 69417

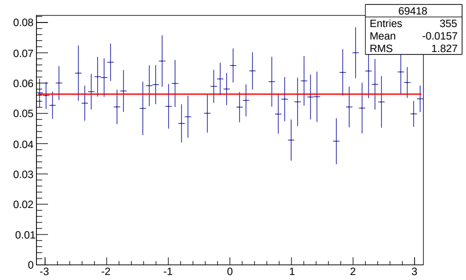
Phi Distribution for Run 69418

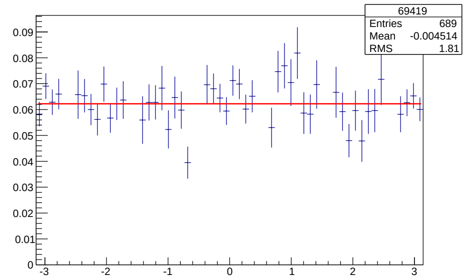
Phi Distribution for Run 69419

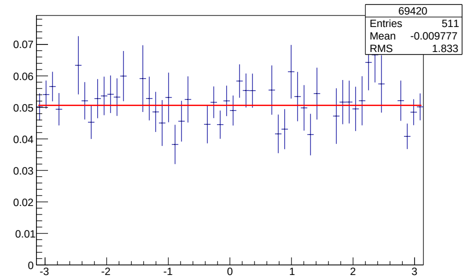
Phi Distribution for Run 69420

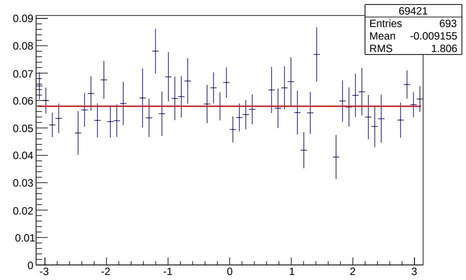
Phi Distribution for Run 69421

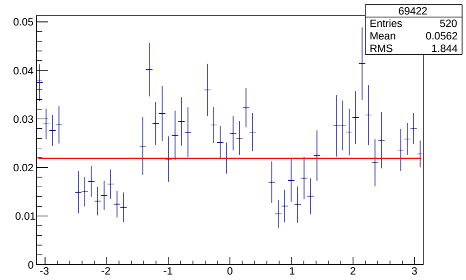
Phi Distribution for Run 69422

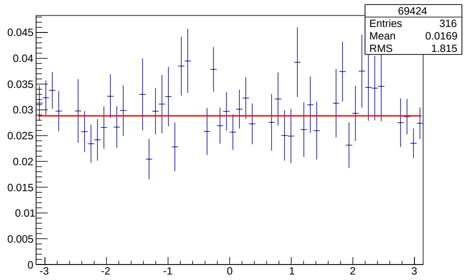
Phi Distribution for Run 69424

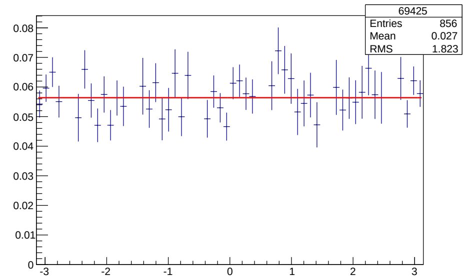
Phi Distribution for Run 69425

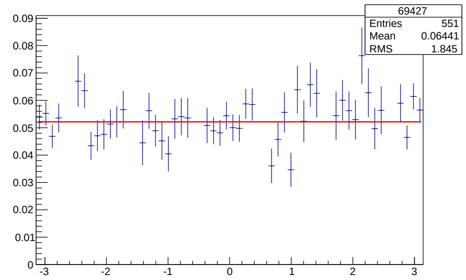
Phi Distribution for Run 69427

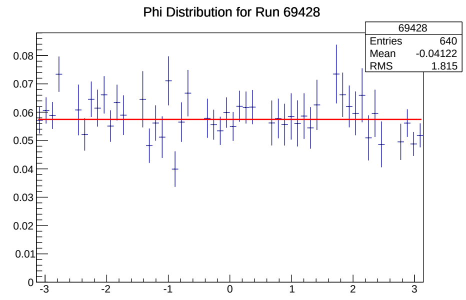
Phi Distribution for Run 69428
69428
Entries 640
Mean -0.04122
RMS 1.815
0.08
0.07
0.06
0.05
0.04
0.03
0.02
0.01
0
-3
-2
-1
0
1
2
3

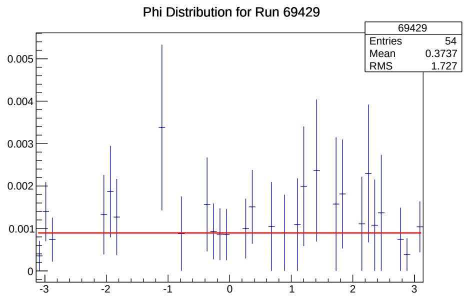
Phi Distribution for Run 69429
69429
Entries 54
Mean 0.3737
RMS 1.727
0.005
0.004
0.003
0.002
0.001
0
-3
-2
-1
0
1
2
3

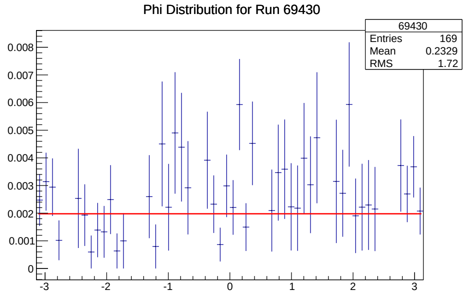
Phi Distribution for Run 69430
69430
Entries 169
Mean 0.2329
RMS 1.72
0.008
0.007
0.006
0.005
0.004
0.003
0.002
0.001
0
-3
-2
-1
0
1
2
3

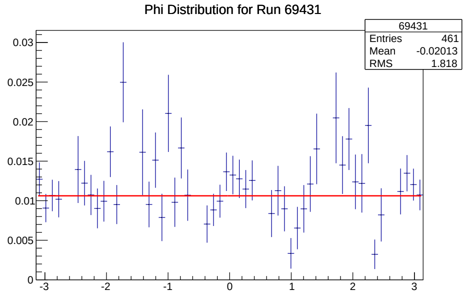
Phi Distribution for Run 69431
69431
Entries 461
Mean -0.02013
RMS 1.818
0.03
0.025
0.02
0.015
0.01
0.005
0
-3
-2
-1
0
1
2
3

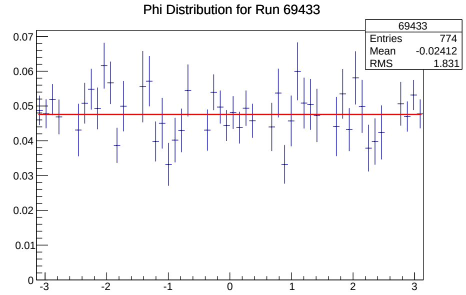
Phi Distribution for Run 69433
69433
Entries 774
Mean -0.02412
RMS 1.831
0.07
0.06
0.05
0.04
0.03
0.02
0.01
0
-3
-2
-1
0
1
2
3

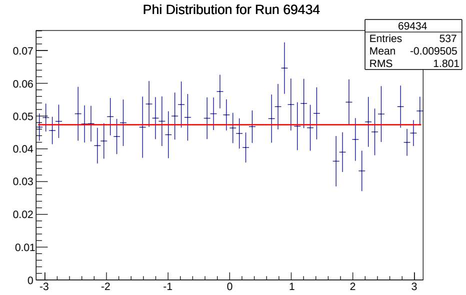
Phi Distribution for Run 69434
69434
Entries 537
Mean -0.009505
RMS 1.801
0.07
0.06
0.05
0.04
0.03
0.02
0.01
0
-3
-2
-1
0
1
2
3

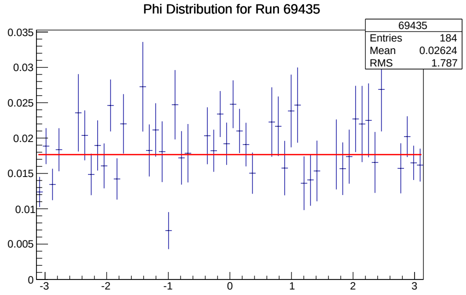
Phi Distribution for Run 69435
69435
Entries 184
Mean 0.02624
RMS 1.787
0.035
0.03
0.025
0.02
0.015
0.01
0.005
0
-3
-2
-1
0
1
2
3

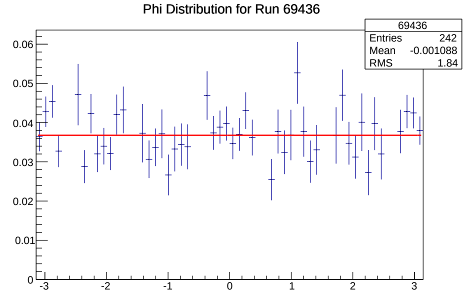
Phi Distribution for Run 69436
69436
Entries 242
Mean -0.001088
RMS 1.84
0.06
0.05
0.04
0.03
0.02
0.01
0
-3
-2
-1
0
1
2
3

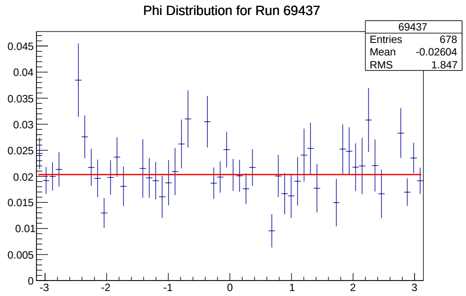
Phi Distribution for Run 69437
69437
Entries 678
Mean -0.02604
RMS 1.847
0.045
0.04
0.035
0.03
0.025
0.02
0.015
0.01
0.005
0
-3
-2
-1
0
1
2
3

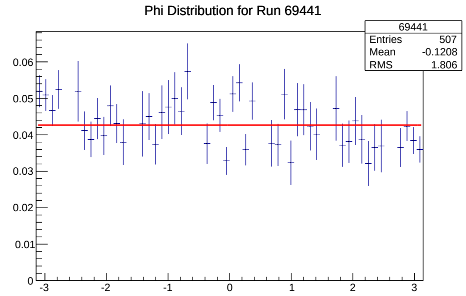
Phi Distribution for Run 69441
69441
Entries 507
Mean -0.1208
RMS 1.806
0.06
0.05
0.04
0.03
0.02
0.01
0
-3
-2
-1
0
1
2
3

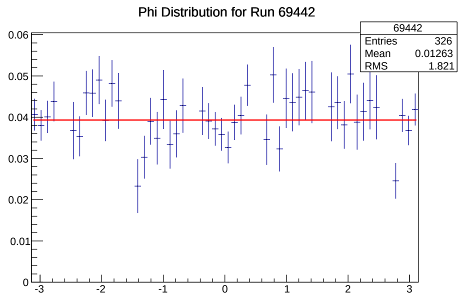
Phi Distribution for Run 69442

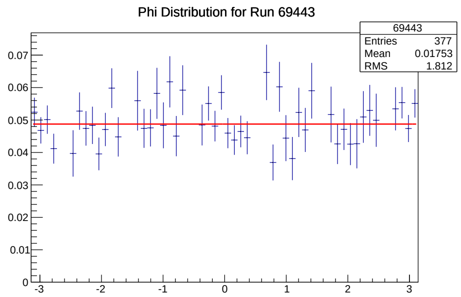
Phi Distribution for Run 69443

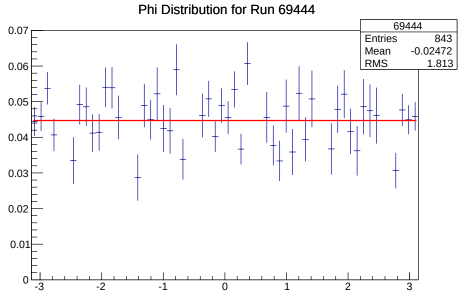
Phi Distribution for Run 69444

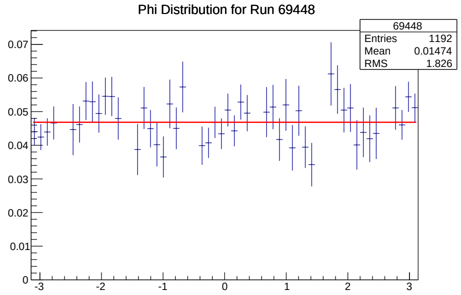
Phi Distribution for Run 69448

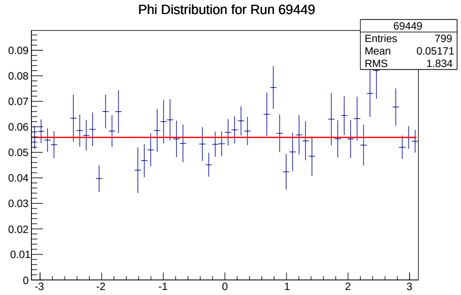
Phi Distribution for Run 69449

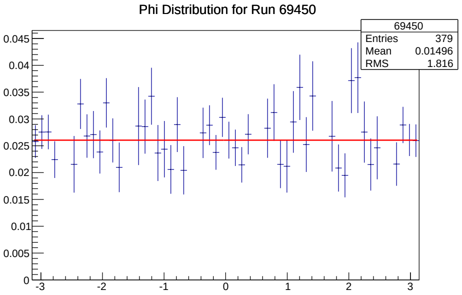
Phi Distribution for Run 69450

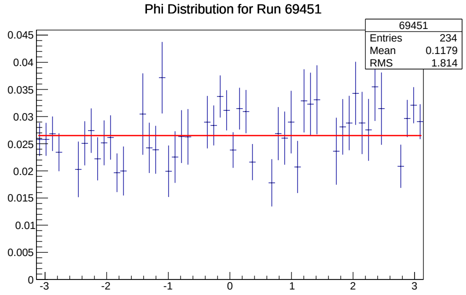
Phi Distribution for Run 69451

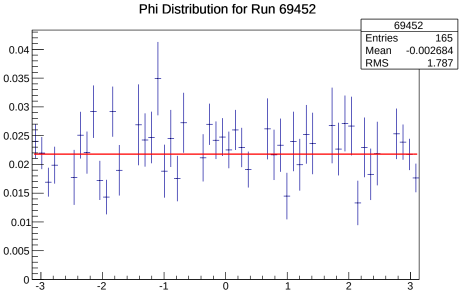
Phi Distribution for Run 69452

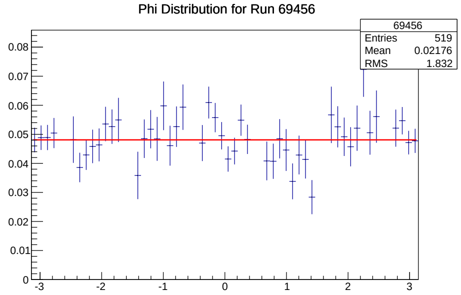
Phi Distribution for Run 69456

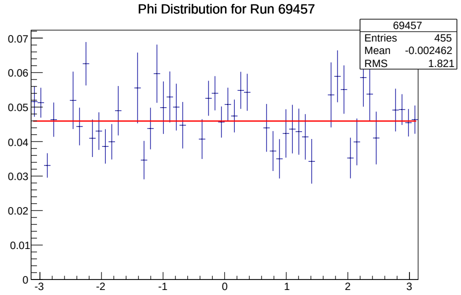
Phi Distribution for Run 69457

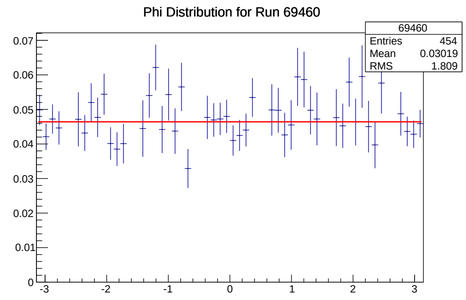
Phi Distribution for Run 69460
69460
Entries 454
Mean 0.03019
RMS 1.809
0.07
0.06
0.05
0.04
0.03
0.02
0.01
0
-3
-2
-1
0
1
2
3

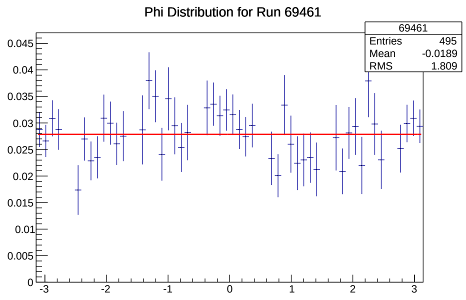
Phi Distribution for Run 69461
69461
Entries 495
Mean -0.0189
RMS 1.809
0.045
0.04
0.035
0.03
0.025
0.02
0.015
0.01
0.005
0
-3
-2
-1
0
1
2
3

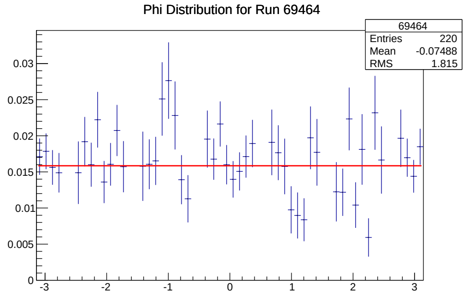
Phi Distribution for Run 69464
69464
Entries 220
Mean -0.07488
RMS 1.815
0.03
0.025
0.02
0.015
0.01
0.005
0
-3
-2
-1
0
1
2
3

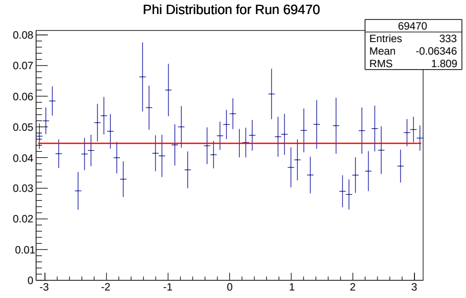
Phi Distribution for Run 69470
69470
Entries 333
Mean -0.06346
RMS 1.809
0.08
0.07
0.06
0.05
0.04
0.03
0.02
0.01
0
-3
-2
-1
0
1
2
3

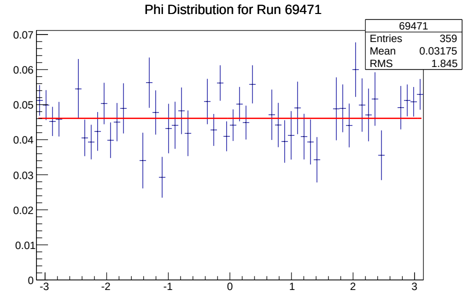
Phi Distribution for Run 69471
69471
Entries 359
Mean 0.03175
RMS 1.845
0.07
0.06
0.05
0.04
0.03
0.02
0.01
0
-3
-2
-1
0
1
2
3

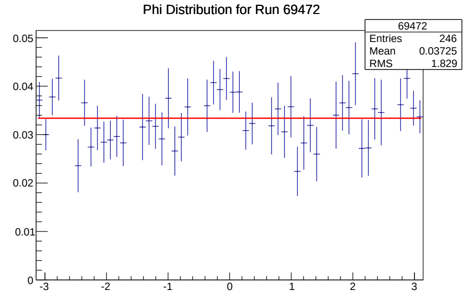
Phi Distribution for Run 69472
69472
Entries 246
Mean 0.03725
RMS 1.829
0.05
0.04
0.03
0.02
0.01
0
-3
-2
-1
0
1
2
3

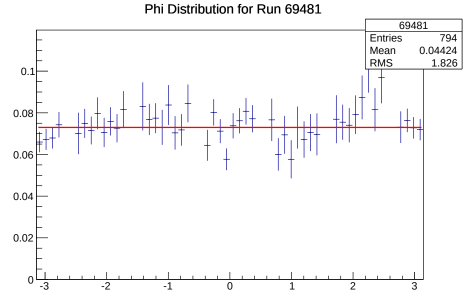
Phi Distribution for Run 69481
69481
Entries 794
Mean 0.04424
RMS 1.826
0.1
0.08
0.06
0.04
0.02
0
-3
-2
-1
0
1
2
3

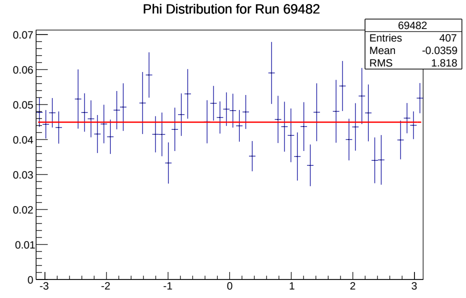
Phi Distribution for Run 69482
69482
Entries 407
Mean -0.0359
RMS 1.818
0.07
0.06
0.05
0.04
0.03
0.02
0.01
0
-3
-2
-1
0
1
2
3

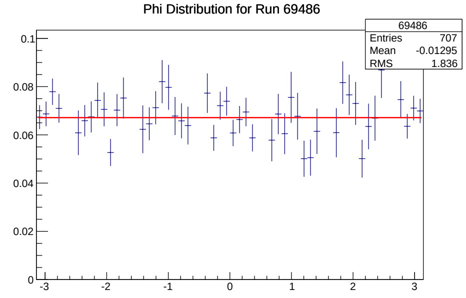
Phi Distribution for Run 69486
69486
Entries 707
Mean -0.01295
RMS 1.836
0.1
0.08
0.06
0.04
0.02
0
-3
-2
-1
0
1
2
3

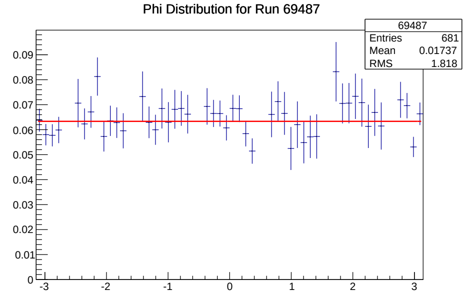
Phi Distribution for Run 69487
69487
Entries 681
Mean 0.01737
RMS 1.818
0.09
0.08
0.07
0.06
0.05
0.04
0.03
0.02
0.01
0
-3
-2
-1
0
1
2
3

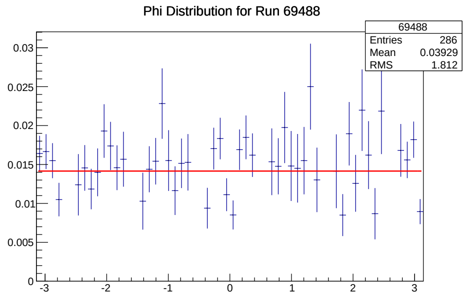
Phi Distribution for Run 69488

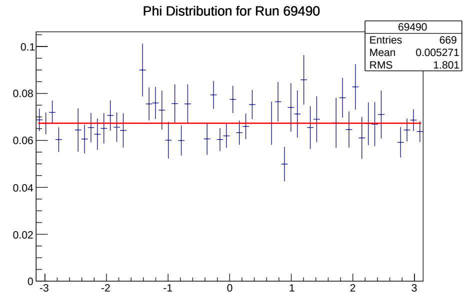
Phi Distribution for Run 69490

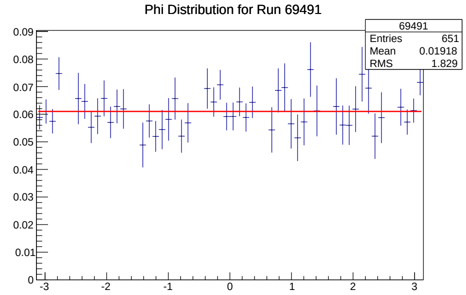
Phi Distribution for Run 69491

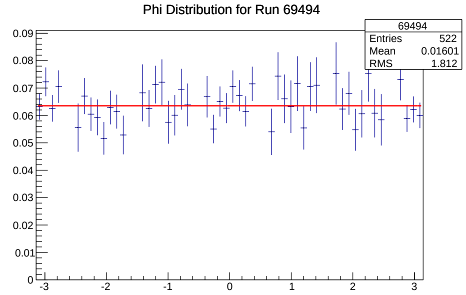
Phi Distribution for Run 69494

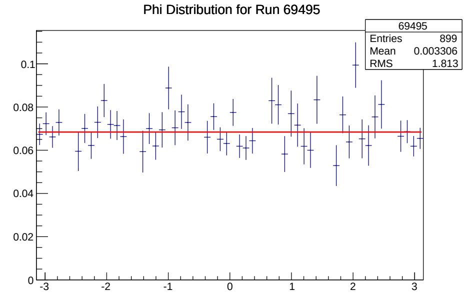
Phi Distribution for Run 69495

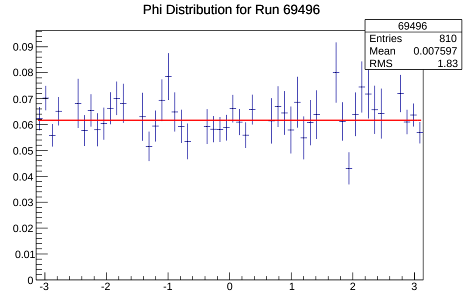
Phi Distribution for Run 69496

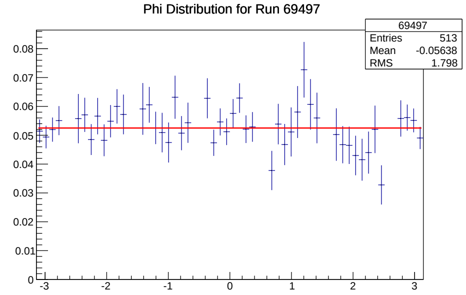
Phi Distribution for Run 69497

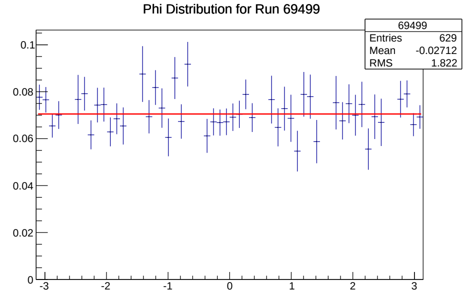
Phi Distribution for Run 69499

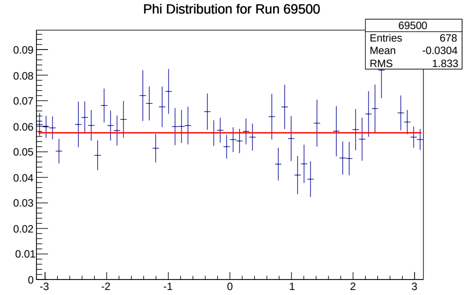
Phi Distribution for Run 69500

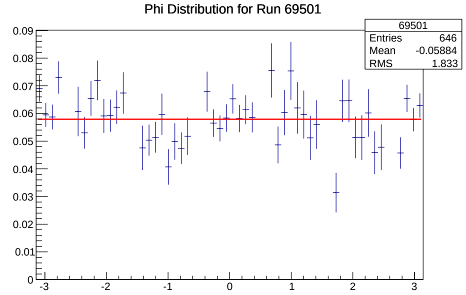
Phi Distribution for Run 69501

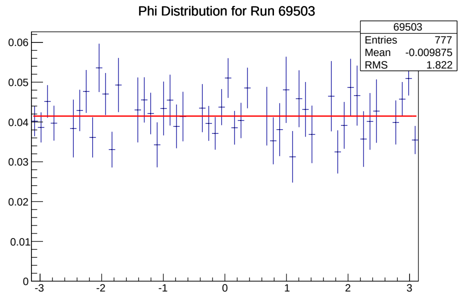
Phi Distribution for Run 69503
69503
Entries 777
Mean -0.009875
RMS 1.822
0.06
0.05
0.04
0.03
0.02
0.01
0
-3
-2
-1
0
1
2
3

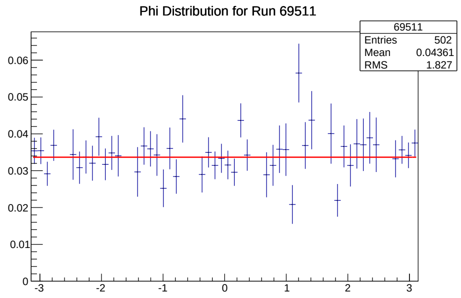
Phi Distribution for Run 69511
69511
Entries 502
Mean 0.04361
RMS 1.827
0.06
0.05
0.04
0.03
0.02
0.01
0
-3
-2
-1
0
1
2
3

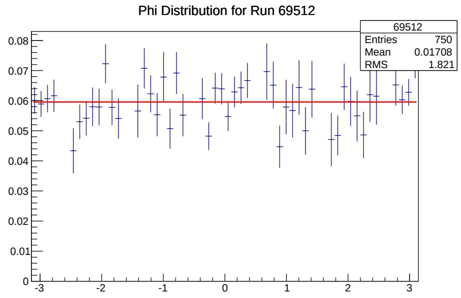
Phi Distribution for Run 69512
69512
Entries 750
Mean 0.01708
RMS 1.821
0.08
0.07
0.06
0.05
0.04
0.03
0.02
0.01
0
-3
-2
-1
0
1
2
3

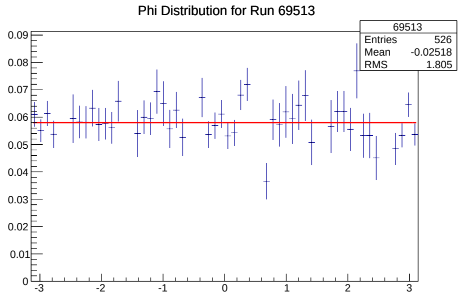
Phi Distribution for Run 69513
69513
Entries 526
Mean -0.02518
RMS 1.805
0.09
0.08
0.07
0.06
0.05
0.04
0.03
0.02
0.01
0
-3
-2
-1
0
1
2
3

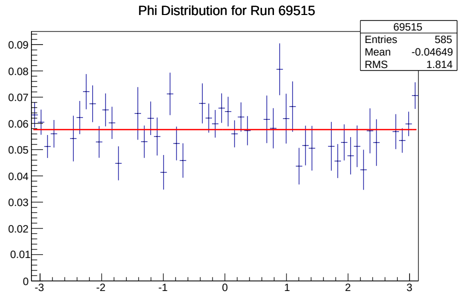
Phi Distribution for Run 69515
69515
Entries 585
Mean -0.04649
RMS 1.814
0.09
0.08
0.07
0.06
0.05
0.04
0.03
0.02
0.01
0
-3
-2
-1
0
1
2
3

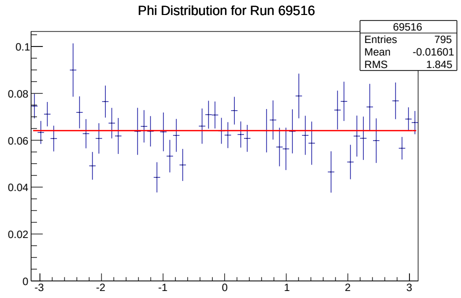
Phi Distribution for Run 69516
69516
Entries 795
Mean -0.01601
RMS 1.845
0.1
0.08
0.06
0.04
0.02
0
-3
-2
-1
0
1
2
3

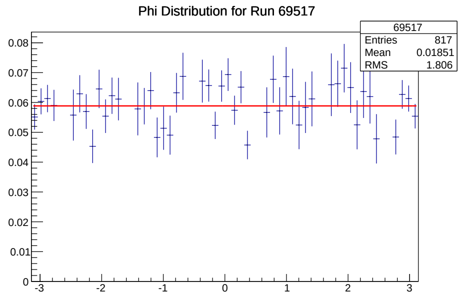
Phi Distribution for Run 69517
69517
Entries 817
Mean 0.01851
RMS 1.806
0.08
0.07
0.06
0.05
0.04
0.03
0.02
0.01
0
-3
-2
-1
0
1
2
3

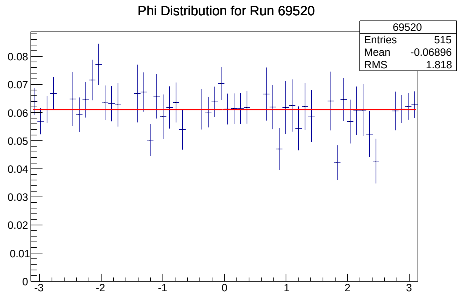
Phi Distribution for Run 69520
69520
Entries 515
Mean -0.06896
RMS 1.818
0.08
0.07
0.06
0.05
0.04
0.03
0.02
0.01
0
-3
-2
-1
0
1
2
3

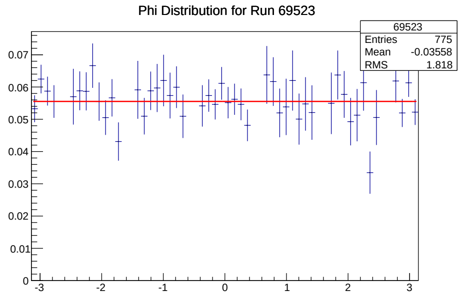
Phi Distribution for Run 69523
69523
Entries 775
Mean -0.03558
RMS 1.818
0.07
0.06
0.05
0.04
0.03
0.02
0.01
0
-3
-2
-1
0
1
2
3

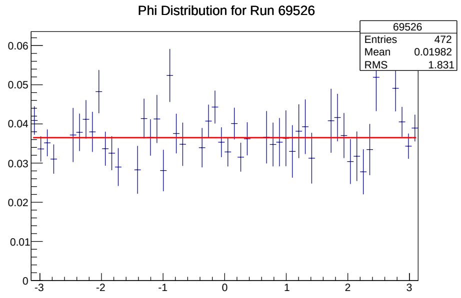
Phi Distribution for Run 69526
69526
Entries 472
Mean 0.01982
RMS 1.831
0.06
0.05
0.04
0.03
0.02
0.01
0
-3
-2
-1
0
1
2
3

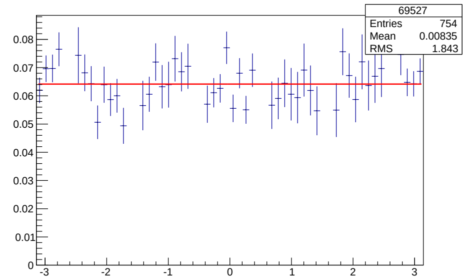
Phi Distribution for Run 69527

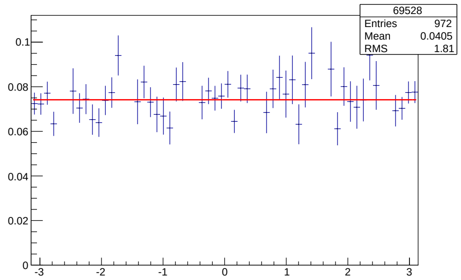
Phi Distribution for Run 69528

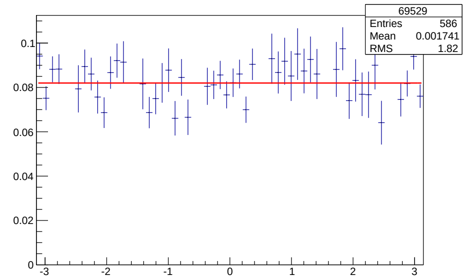
Phi Distribution for Run 69529

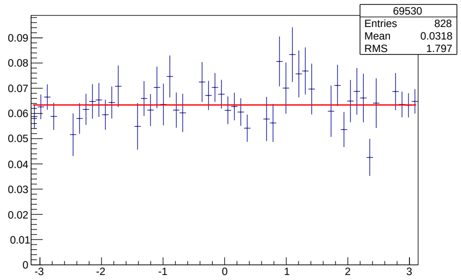
Phi Distribution for Run 69530

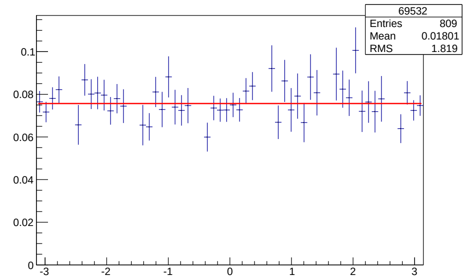
Phi Distribution for Run 69532

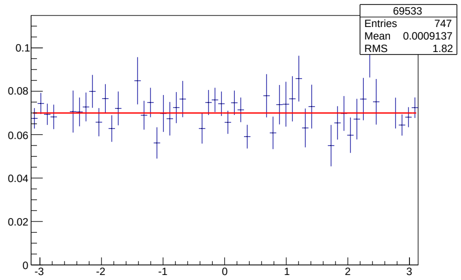
Phi Distribution for Run 69533

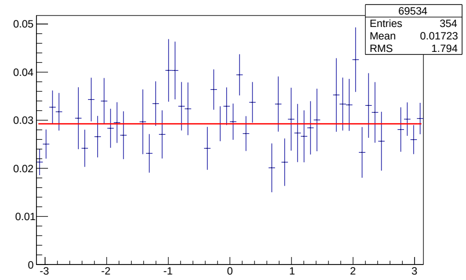
Phi Distribution for Run 69534

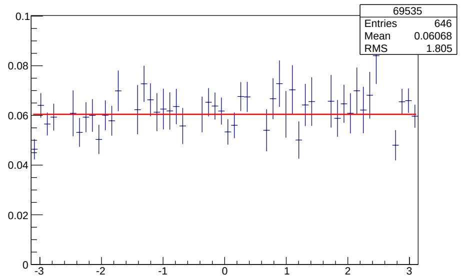
Phi Distribution for Run 69535

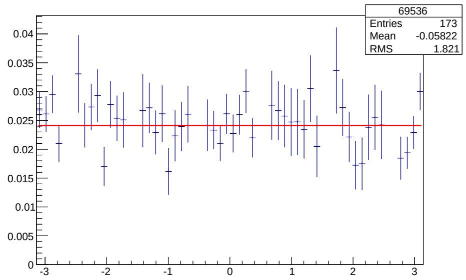
Phi Distribution for Run 69536

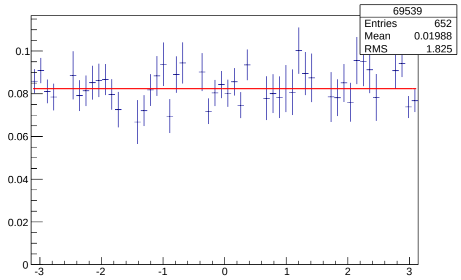
Phi Distribution for Run 69539

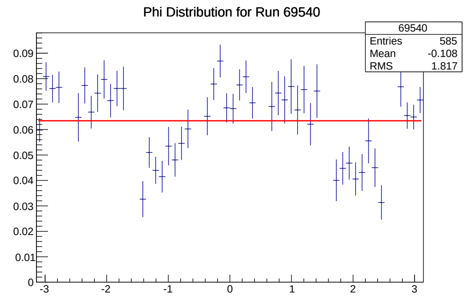
Phi Distribution for Run 69540

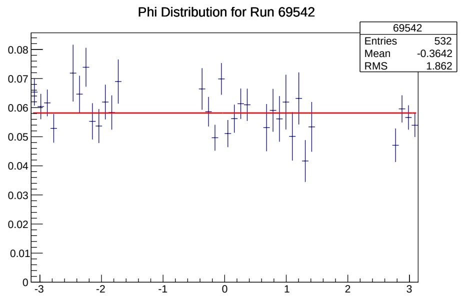
Phi Distribution for Run 69542

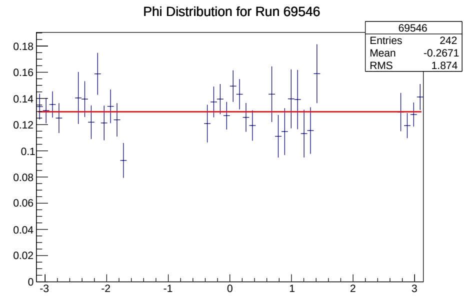
Phi Distribution for Run 69546

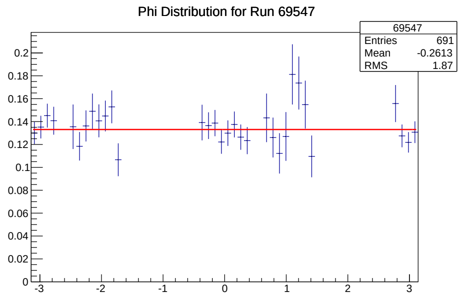
Phi Distribution for Run 69547

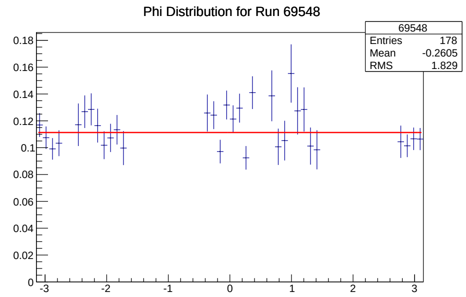
Phi Distribution for Run 69548

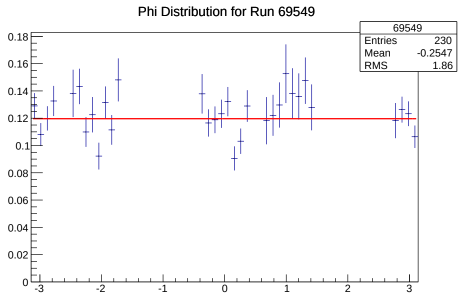
Phi Distribution for Run 69549

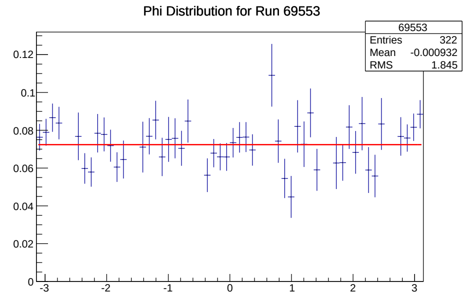
Phi Distribution for Run 69553

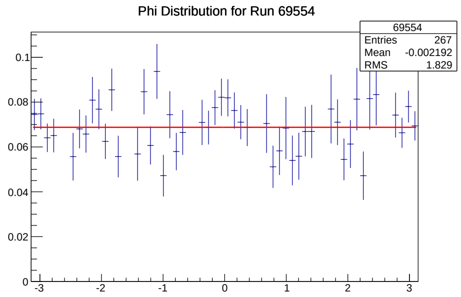
Phi Distribution for Run 69554

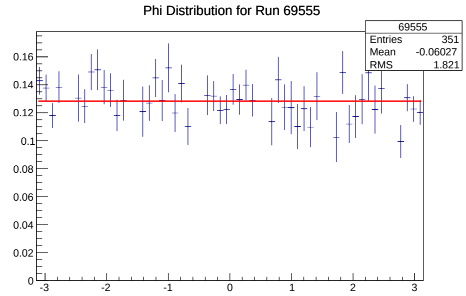
Phi Distribution for Run 69555

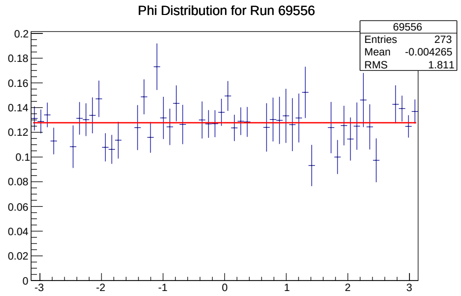
Phi Distribution for Run 69556

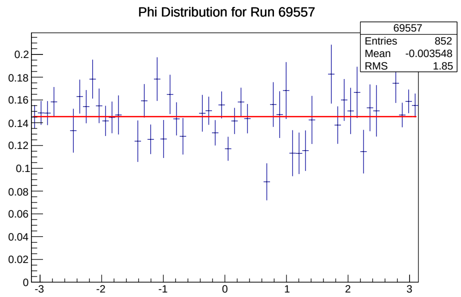

Phi Distribution for Run 69557

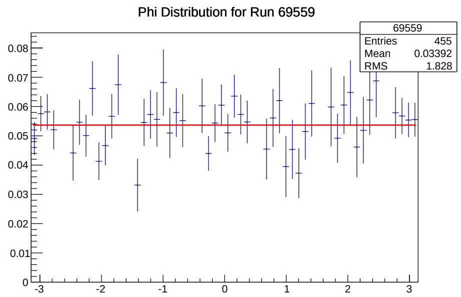

Phi Distribution for Run 69559

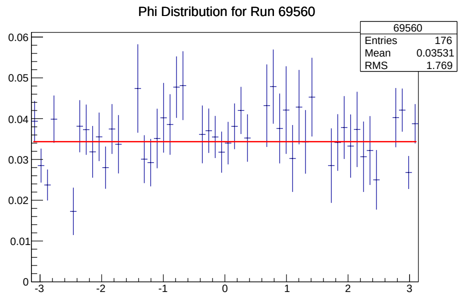

Phi Distribution for Run 69560

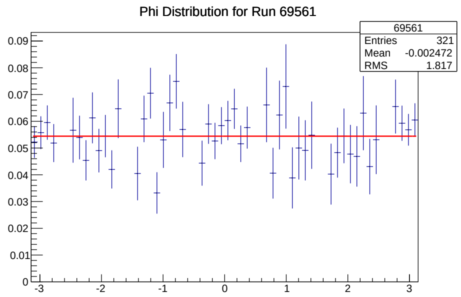

Phi Distribution for Run 69561

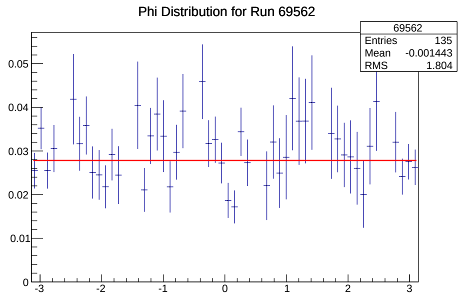

Phi Distribution for Run 69562

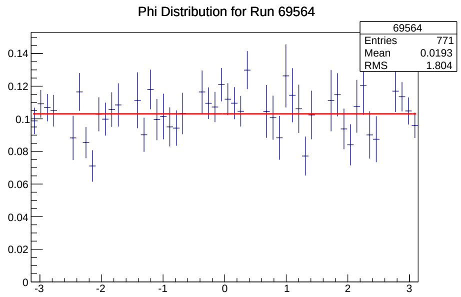

Phi Distribution for Run 69564

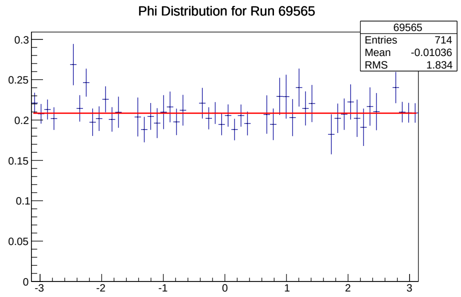

Phi Distribution for Run 69565

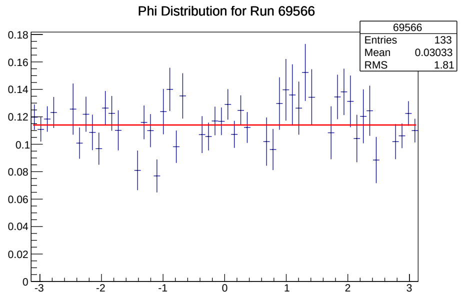

Phi Distribution for Run 69566

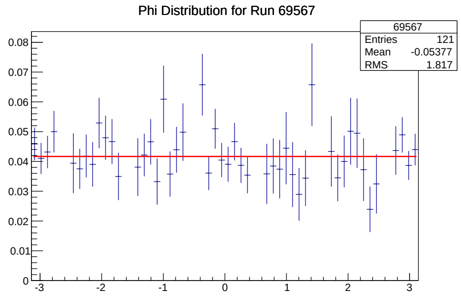

Phi Distribution for Run 69567

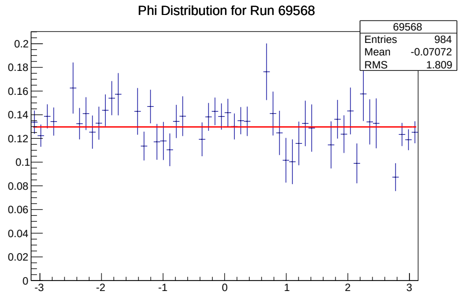

Phi Distribution for Run 69568

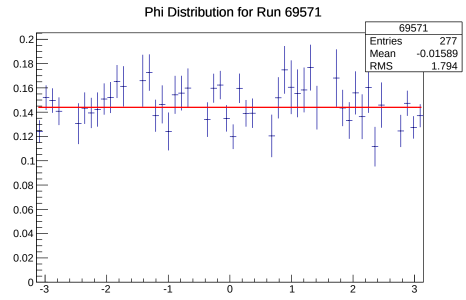
Phi Distribution for Run 69571

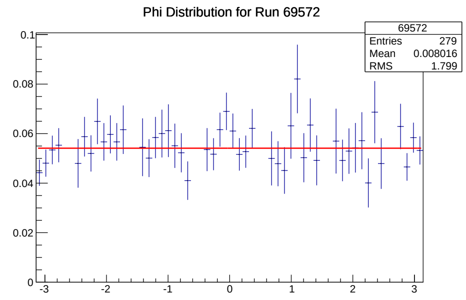
Phi Distribution for Run 69572

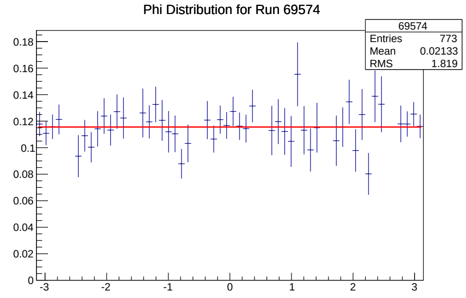
Phi Distribution for Run 69574

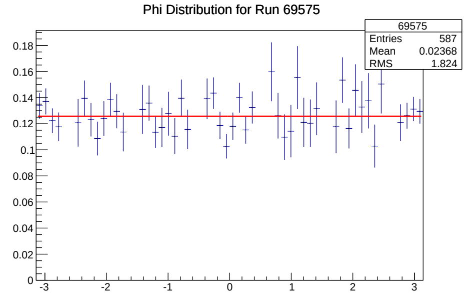
Phi Distribution for Run 69575

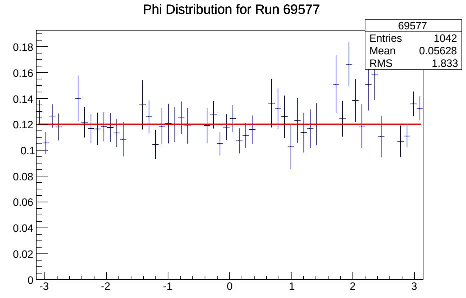
Phi Distribution for Run 69577

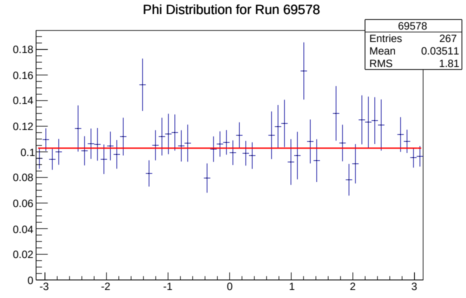
Phi Distribution for Run 69578

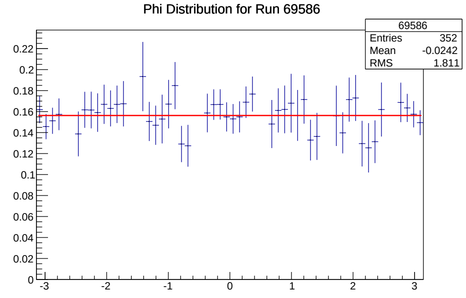
Phi Distribution for Run 69586

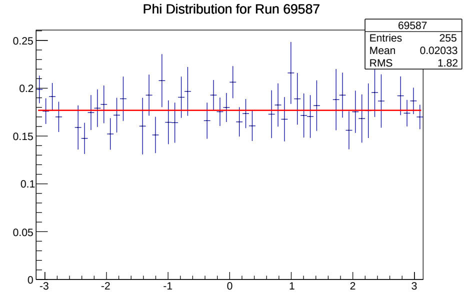
Phi Distribution for Run 69587

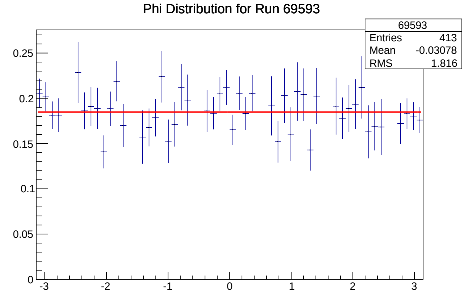
Phi Distribution for Run 69593

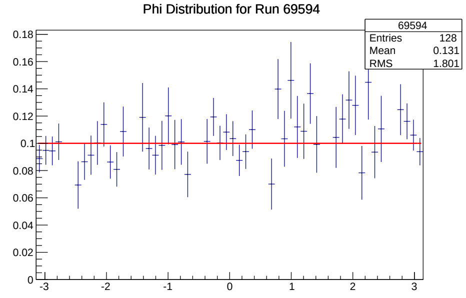
Phi Distribution for Run 69594

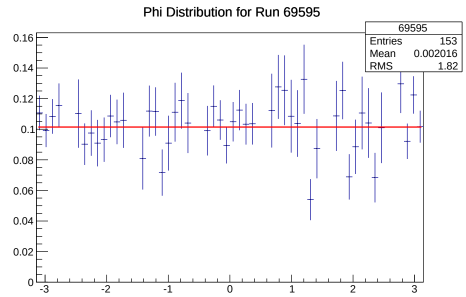
Phi Distribution for Run 69595

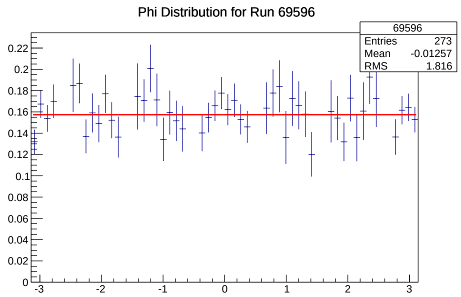
Phi Distribution for Run 69596

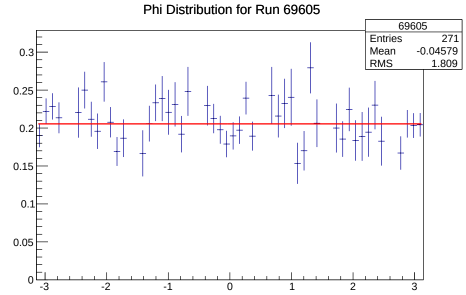
Phi Distribution for Run 69605

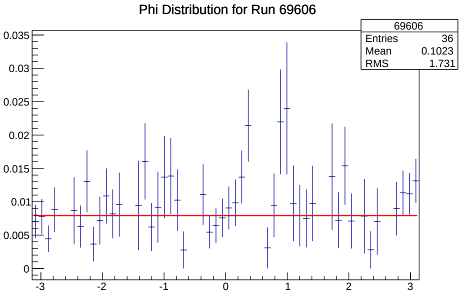
Phi Distribution for Run 69606

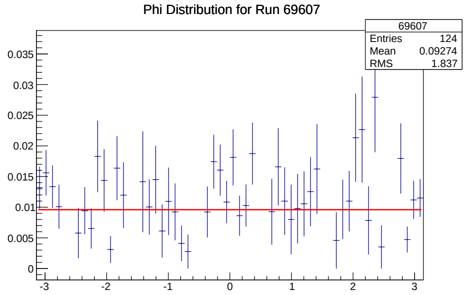
Phi Distribution for Run 69607

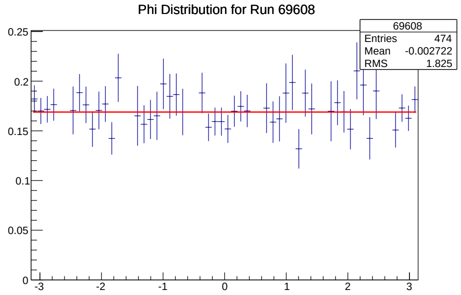
Phi Distribution for Run 69608

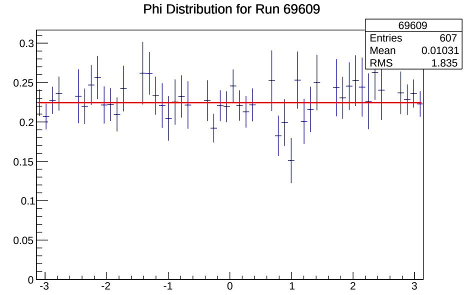
Phi Distribution for Run 69609

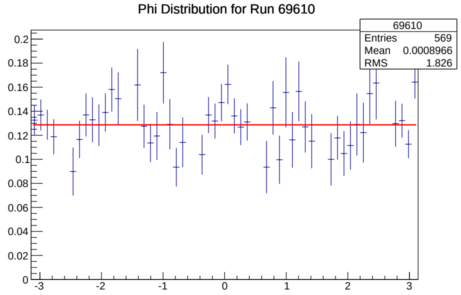
Phi Distribution for Run 69610

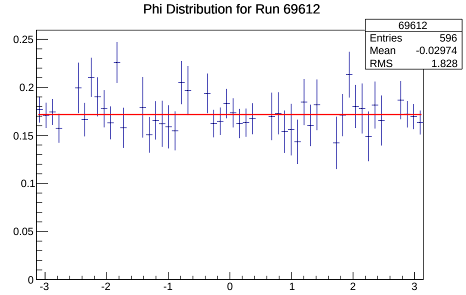
Phi Distribution for Run 69612

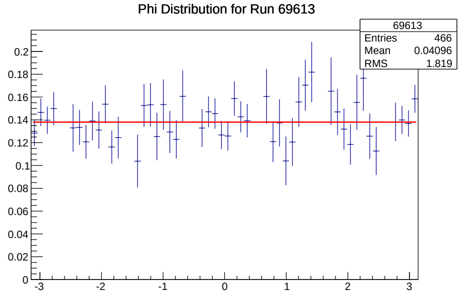
Phi Distribution for Run 69613

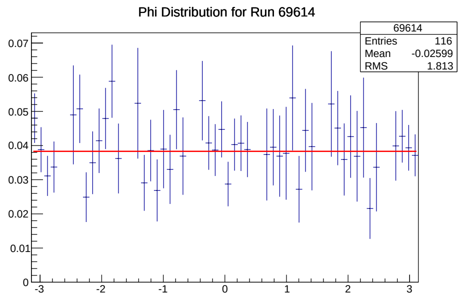
Phi Distribution for Run 69614
69614
Entries 116
Mean -0.02599
RMS 1.813
0.07
0.06
0.05
0.04
0.03
0.02
0.01
0
-3
-2
-1
0
1
2
3

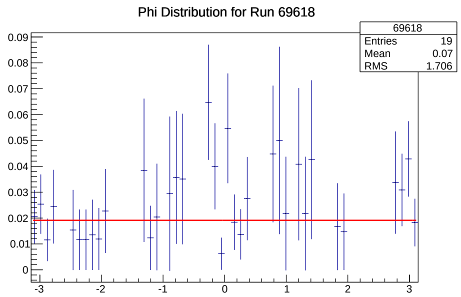
Phi Distribution for Run 69618
69618
Entries 19
Mean 0.07
RMS 1.706
0.09
0.08
0.07
0.06
0.05
0.04
0.03
0.02
0.01
0
-3
-2
-1
0
1
2
3

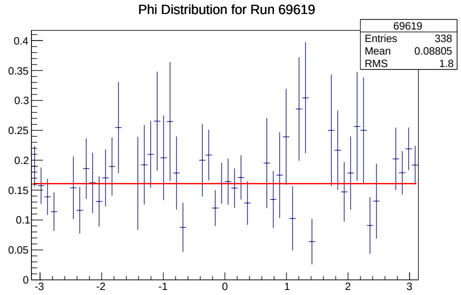
Phi Distribution for Run 69619
69619
Entries 338
Mean 0.08805
RMS 1.8
0.4
0.35
0.3
0.25
0.2
0.15
0.1
0.05
0
-3
-2
-1
0
1
2
3

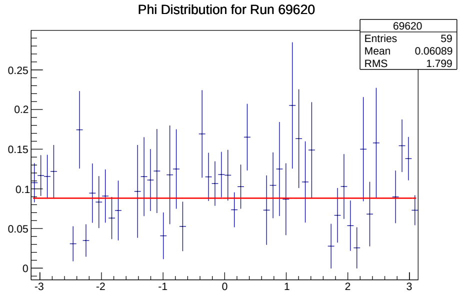
Phi Distribution for Run 69620
69620
Entries 59
Mean 0.06089
RMS 1.799
0.25
0.2
0.15
0.1
0.05
0
-3
-2
-1
0
1
2
3

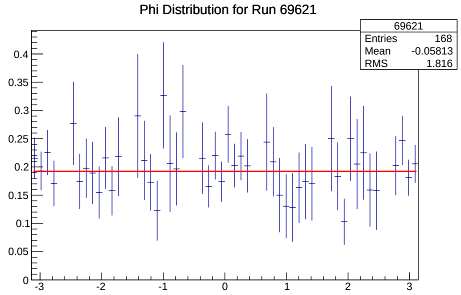
Phi Distribution for Run 69621
69621
Entries 168
Mean -0.05813
RMS 1.816
0.4
0.35
0.3
0.25
0.2
0.15
0.1
0.05
0
-3
-2
-1
0
1
2
3

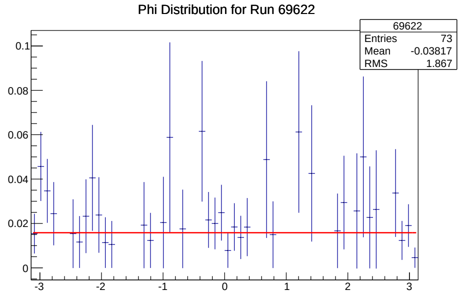
Phi Distribution for Run 69622
69622
Entries 73
Mean -0.03817
RMS 1.867
0.1
0.08
0.06
0.04
0.02
0
-3
-2
-1
0
1
2
3

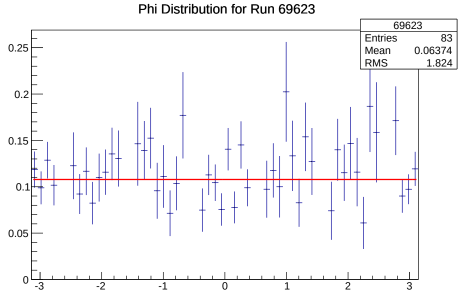
Phi Distribution for Run 69623
69623
Entries 83
Mean 0.06374
RMS 1.824
0.25
0.2
0.15
0.1
0.05
0
-3
-2
-1
0
1
2
3

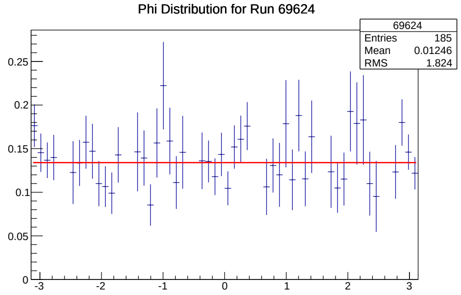
Phi Distribution for Run 69624
69624
Entries 185
Mean 0.01246
RMS 1.824
0.25
0.2
0.15
0.1
0.05
0
-3
-2
-1
0
1
2
3

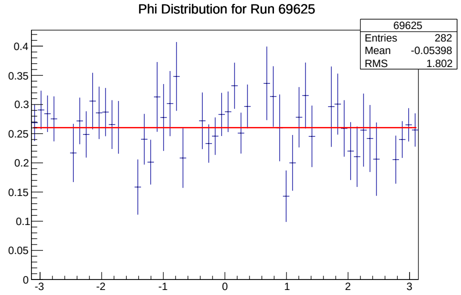
Phi Distribution for Run 69625
69625
Entries 282
Mean -0.05398
RMS 1.802
0.4
0.35
0.3
0.25
0.2
0.15
0.1
0.05
0
-3
-2
-1
0
1
2
3

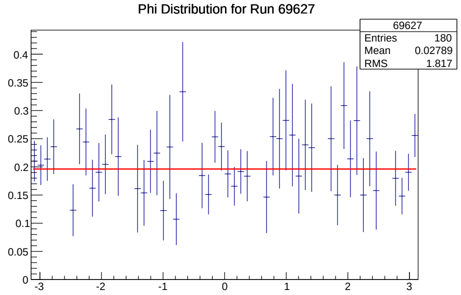
Phi Distribution for Run 69627
69627
Entries 180
Mean 0.02789
RMS 1.817
0.4
0.35
0.3
0.25
0.2
0.15
0.1
0.05
0
-3
-2
-1
0
1
2
3

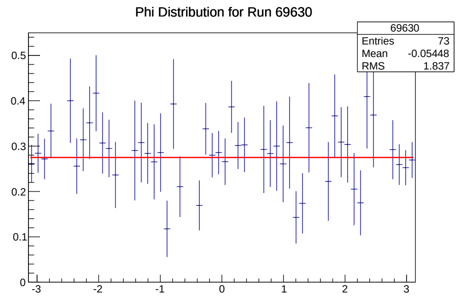

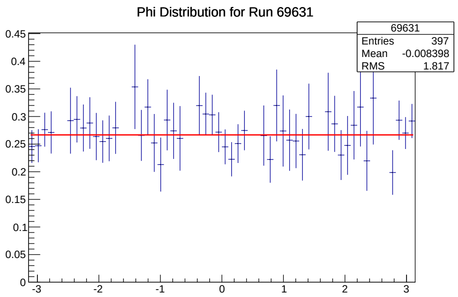

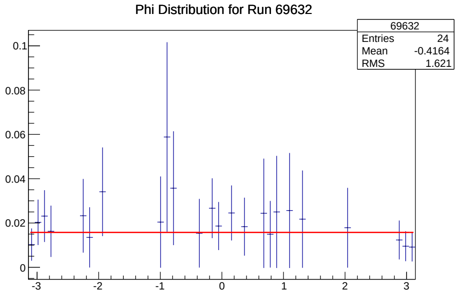

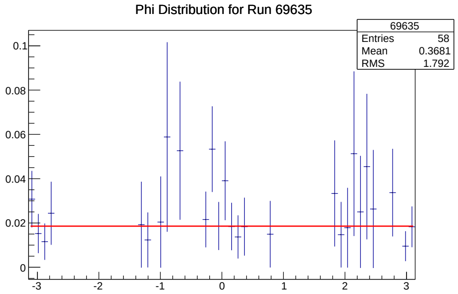

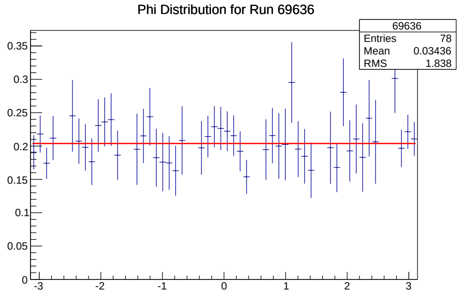

References

[1] D. Ho et al. Beam-Target Helicity Asymmetry for $\vec{\gamma}\vec{n} \to \pi^- p$ in the N* Resonance Region. *Phys. Rev. Lett.*, 118:242002, 2017.

[2] N. Suzuki et al. Disentangling the Dynamical Origin of P_{11} Nucleon Resonances. *Phys. Rev. Lett.*, 104:042302, 2010.

[3] A. M. Sandorfi et al. Determining pseudoscalar meson photoproduction amplitudes from complete experiments. *J. of Phys. G*, 38:053001, 2011.

[4] B. A. Mecking et al. The CEBAF Large Acceptance Spectrometer (CLAS). *Nucl. Instrum. Meth. A*, 503:513, 2003.

[5] C. D. Bass et al. A Portable Cryostat for the Cold Transfer of Polarized Solid HD Targets: HD-Ice-I. *Nucl. Instrum. Meth. A*, 737:107, 2014.

[6] M. M. Lowry et al. A Cryostat to Hold Frozen-Spin Polarized HD Targets in CLAS: HDice-II. *Nucl. Instrum. Meth. A*, 815:31, 2016.

[7] X. Wei et al. Boosting Deuteron Polarization in HD Targets: Experience of moving spins between H and D with RF methods during the E06-101 experiment at Jefferson Lab. *PoS*, PSTP2013:016, 2014.

[8] Ho D. Peng P., Kageya T. et al. E asymmetry for $\vec{\gamma}\vec{n} \to \pi^- p$ from g14 (hdice) data. *CLAS analysis note 104*, 2016, 2016.

[9] E. Pasyuk. Energy-loss corrections for charged particles in clas. *CLAS Note*, 2007-016, 2007.

[10] K. Livingston. Polarization from coherent bremsstrahlung enhancement. *CLAS analysis note 20*, 2011, 2011.

[11] F. A. Natter et al. Monte carlo simulation and analytical calculation of coherent bremsstrahlung and its polarisation. *Nucl. Instrum. Meth. B*, 211(4):465–486, 2003.

[12] F. Rambo et al. Coherent π^0 photoproduction from ^{4}He. *Nuclear Physics A*, 660(1):69–83, 1999.

[13] B. Ritchie and M. Dugger. Consistency corrections to the linear photon polarization for g8b data. *CLAS analysis note 02*, 2012.

[14] D. Sokhan. *Beam Asymmetry Measurement from Pion Photoproduction on the Neutron*. PhD thesis, Edinburgh U., 2009.

[15] W. J. Briscoe, A. Schmidt, I. Strakovsky, R. L. Workman, and A. Švarc. Extended SAID partial-wave analysis of pion photoproduction. *in progress*, 2023.

[16] V. L. Kashevarov, M. Ostrick, and L. Tiator. Regge phenomenology in π^0 and η photoproduction. *Phys. Rev. C*, 96(3):035207, 2017.

[17] T. Seifen et al. Polarization observables in double neutral pion photoproduction. ..., (7), 2022.

[18] F. V. Adamian, P. I. Galumian, V. O. Grabsky, G. G. Akopian, V. K. Oktanian, G. V. Karapetian, V. V. Karapetian, and G. A. Vartapetian. Single π^- Meson Photoproduction on Neutrons by Linearly Polarized Photons in the Third and Fourth Resonance Region. *J. Phys. G*, 15:1797–1803, 1989.

[19] J. Alspector et al. Pi+- and pi0 production by polarized photons in the resonance region. *Phys. Rev. Lett.*, 28:1403–1406, 1972.